

**TECHNISCHE  
UNIVERSITÄT  
DRESDEN**

---

---

# Biochemical functionalization of silicon dioxide surfaces for sensing applications

Dissertation  
zur Erlangung des wissenschaftlichen Grades  
Doktoringenieurin

vorgelegt von

Lotta Römhildt  
geboren am 13.03.1984 in Hannover

Institut für Werkstoffwissenschaft  
Lehrstuhl Materialwissenschaft und Nanotechnik  
Fakultät Maschinenwesen  
Technische Universität Dresden  
2014

Eingereicht am 14.02.2014

1. Gutachter: Prof. Dr. Gianaurelio Cuniberti (TU Dresden)
2. Gutachter: Prof. Dr. Sven Ingebrandt (FH Kaiserslautern)

Verteidigt am 12.05.2014





## Abstract

The aim of this work was to functionalize silicon dioxide surfaces with biochemical molecules in such a way that biorecognition of target molecules in solution will be possible. By introducing a tool set of different molecules and characterization methods, a more universal approach towards various biosensor setups is presented.

This includes on the one hand preparation of the biosensor surfaces to allow further molecule attachment via their reactive functional groups. Secondly, the selection of chemical molecules providing suitable counterparts for abundant functional groups of potential receptors is discussed. Two detection schemes are introduced – based on an antibody to detect the antibiotic amoxicillin and aptamers to detect thrombin.

The antibody was implemented in an inverse competition assay to probe such small target molecules. Antibiotic residues are often present in wastewater. Aptamers, so-called artificial antibodies, were selected as they provide many advantages over antibodies. As a model system, two different thrombin binding aptamers were chosen which allowed to perform sandwich assays as well. The protein thrombin plays an important role in the blood coagulation cascade. To probe the individual modification steps, different techniques for analysis were applied. Surface micropatterning was introduced to improve recognition of modified areas and fluorescence-to-background ratios resulting in a thrombin detection limit down to 20 pM. One important goal was the integration in ion-sensitive field-effect transistor devices. Aptamers are small in size which might enable a higher sensitivity of these devices compared to the use of antibodies because of the Debye layer thickness.

As a final step, first measurements towards silicon nanowire based field-effect transistor biosensors were carried out on devices with bottom-up and top-down fabricated nanowires using both proposed receptor-analyte combinations. The potential of these devices as portable sensors for real-time and label-free biosensing is demonstrated.

## Kurzreferat

Ziel dieser Arbeit war es Siliziumdioxidoberflächen so mit biochemischen Molekülen zu funktionalisieren, dass die biologisch spezifische Erkennung von Zielmolekülen in Lösung möglich wird. Hier wird eine Auswahl an geeigneten Molekülen und Charakterisierungsmethoden für einen vielseitigen Ansatz gezeigt, der auf verschiedene Biosensorsysteme anwendbar ist.

Das beinhaltet zum Einen die Präparation der Biosensoroberflächen, so dass die Moleküle über reaktive funktionelle Gruppen angebunden werden können. Als zweites ist die Auswahl der chemischen Moleküle wichtig, da diese die passenden Gegenstücke zu potentiellen funktionellen Gruppen der Rezeptoren darstellen. Zwei verschiedene Detektionsvarianten werden eingeführt – Antikörper gegen das Antibiotikum Amoxicillin und Aptamere gegen Thrombin.

Der Antikörper wurde in einen inversen Wettbewerbsassay integriert um einen solch kleinen Analyten detektieren zu können. Rückstände von Antibiotika sind häufig in Abwässern zu finden. Aptamere, sogenannte künstliche Antikörper, weisen gegenüber Antikörpern viele Vorteile auf. Als ein Modellsystem wurden zwei unterschiedliche Thrombin bindende Aptamere verwendet, was auch die Durchführung von Sandwich Assays ermöglichte. Das Protein Thrombin spielt eine wichtige Rolle bei der Blutgerinnung. Um die einzelnen Modifikationsschritte zu untersuchen, wurden verschiedene Charakterisierungsmethoden angewendet. Die Mikrostrukturierung der Funktionalisierung erleichterte die Erkennung der modifizierten Flächen und verbesserte das Fluoreszenz-zu-Hintergrund Verhältnis. Das führte zu einer Detektionsgrenze von 20 pM für Thrombin. Ein wichtiges Ziel dieser Arbeit war die Integration der Funktionalisierung in einen Ionen-sensitiven Feldeffekttransistor. Die kleinen Aptamere könnten dabei aufgrund der geringen Debye-Schichtdicke bei diesen Sensoren eine höhere Sensitivität als mit Antikörpern ermöglichen.

Zuletzt wurden erste Messungen hin zu Silizium Nanodraht basierten Feldeffekttransistor Biosensoren mit beiden untersuchten Rezeptor-Analyt-Kombinationen durchgeführt. Sowohl die Chips mit bottom-up als auch mit top-down gewachsenen Nanodrähten zeigen dabei ihr Potential als handliche Sensoren zur markerfreien Detektion in Echtzeit.







# Contents

<b>Introduction</b>	<b>1</b>
State of the art . . . . .	1
Scope of the thesis . . . . .	2
<b>1. Fundamentals</b>	<b>5</b>
1.1. Introduction to Biosensors . . . . .	5
1.2. Biorecognition . . . . .	7
1.2.1. Biorecognition principles . . . . .	7
1.2.2. Receptors . . . . .	8
1.3. Surface Functionalization . . . . .	14
1.3.1. Noncovalent methods . . . . .	15
1.3.2. Covalent methods . . . . .	18
1.4. Silicon Nanowire Based Field-Effect Transistor Devices . . . . .	21
1.4.1. From FETs to ion-sensitive devices . . . . .	21
1.4.2. Fabrication methods . . . . .	25
1.4.3. Influences of organic solvents and buffer solutions . . . . .	29
1.5. Conclusion . . . . .	31
<b>2. Materials and Methods</b>	<b>33</b>
2.1. Surface modification techniques . . . . .	33
2.1.1. Surfaces . . . . .	33
2.1.2. Chemical surface functionalization . . . . .	35
2.1.3. Patterning . . . . .	38
2.2. Selected target molecules . . . . .	40
2.2.1. Protein thrombin . . . . .	40
2.2.2. Antibiotic amoxicillin . . . . .	41
2.3. List of all materials . . . . .	42
2.4. Characterization techniques for biochemical functionalization . . . . .	44
2.4.1. Atomic force microscopy . . . . .	44
2.4.2. Static contact angle . . . . .	44
2.4.3. Ellipsometry . . . . .	45
2.4.4. Zeta potential . . . . .	46
2.4.5. Fluorescence microscopy . . . . .	46

---

2.5. Characterization techniques for receptor-analyte interactions . . . . .	47
2.5.1. Electromobility shift assay with native polyacrylamide gel . . . . .	47
2.5.2. Quartz-crystal microbalance with dissipation monitoring . . . . .	48
<b>3. Receptor-target combinations</b>	<b>51</b>
3.1. Aptamer based sensing . . . . .	51
3.1.1. Aptamer design . . . . .	51
3.1.2. Sandwich assay for optical detection . . . . .	52
3.1.3. Aptamer attachment strategy . . . . .	52
3.2. Antibody based sensing . . . . .	54
3.2.1. Inverse competition assay . . . . .	54
3.2.2. Attachment strategy . . . . .	55
<b>4. Biochemical Functionalization and Biosensing</b>	<b>57</b>
4.1. Thrombin detection . . . . .	57
4.1.1. Biochemical modifications . . . . .	57
4.1.2. Receptor-analyte interaction . . . . .	68
4.2. Amoxicillin detection . . . . .	74
4.2.1. Biochemical functionalization . . . . .	74
4.2.2. Receptor-analyte interaction . . . . .	75
4.3. Nanowires as tools . . . . .	76
4.3.1. Zeta potential . . . . .	76
4.3.2. Nanowires with lipid bilayer shells . . . . .	78
<b>5. Towards SiNW FET Biosensing</b>	<b>87</b>
5.1. Thrombin detection . . . . .	87
5.1.1. Bottom-up SiNW FET setup . . . . .	87
5.1.2. Device characterization . . . . .	88
5.1.3. Biosensing . . . . .	93
5.2. Amoxicillin detection . . . . .	98
5.2.1. Top-down SiNW FET setup . . . . .	98
5.2.2. Device characterization . . . . .	98
5.2.3. Biosensing . . . . .	99
<b>Summary and Outlook</b>	<b>103</b>
<b>Bibliography</b>	<b>122</b>
<b>Appendix</b>	<b>123</b>
A. Protocols . . . . .	123
A.1. Functionalization . . . . .	123

---

A.2.	Buffers . . . . .	125
A.3.	PDMS . . . . .	126
A.4.	Steps of the sandwich assay . . . . .	126
A.5.	Gelelectrophoresis . . . . .	127
A.6.	Lipids . . . . .	127
B.	Additional results . . . . .	128
B.1.	FET sensing . . . . .	128
<b>List of publications</b>		<b>131</b>



# Introduction

## State of the art

The development of novel biosensor techniques has been one of the strategic directions driving nanoresearch in the past years. The needs of increasingly ageing societies lead to a growing demand for technological assistance in healthcare. The goal here is to reduce the costs and expenditure of time of trained professionals to handle the number of elderly people and assure proper and individual treatment. Due to the high mobility of people worldwide and the fear of epidemic spreading of diseases like virus or bacteria infections, the interest for fast routine tests at low costs and high sensitivity is equally high. Moreover, early recognition and assistance in correct medication are important application fields of novel smart sensors. Mainly health monitoring and disease treatment [1–4] but also environmental applications like testing water pollution by toxics or drug accumulation [5, 6] have been investigated extensively. Current technologies for bacteria or virus detection are sensitive but often the size of the testing equipment, the required trained lab professionals and in some cases the duration of the analysis do not fulfill the aforementioned needs for low cost, portable and fast biosensors.

This is where the emerging field of nano-bio-technology comes into play. Nanomaterials possess special physical properties due to their confinement down to the nanometer range in at least one dimension. The combination of nanomaterials and biological processes like self-assembly or recognition opens up a wide field of novel technological applications, especially for biosensing. Nanomaterials enable the miniaturization of devices and a high sensitivity at the same time due to the increased surface-to-volume ratio. Here, the integration of a silicon nanowire to build a field-effect transistor is used for sensor devices with signal amplification at low power consumption. The latter is advantageous for portable or implantable devices. Silicon nanowires can also be combined with existing silicon wafer processing technology for chip fabrication which will reduce the costs of the disposable chip. Additionally, the integration of bottom-up processes at the nanoscale might further decrease costs as less complex lithography steps are sufficient. Close to the surface, charged molecules lead to a significant impact on the electronic material properties as the whole bulk is affected. Device technology can further amplify this event for readable signals.

The work for this thesis was carried with the aim to make use of a Schottky barrier based silicon nanowire field-effect transistor (SB SiNW FET) as a biosensor by implementing bottom-up synthesized SiNWs. SiNW based FET sensing has been described firstly by Lieber *et al.* in 2001 [7] and to date they demonstrated sensing of DNA and PNA hybridization [8], viruses down to a single virus detection events [9], using antibodies as receptors, multiplexed sensing [10] and cell potentials by kinked NWs [11]. Other groups developed NW arrays in top-down fabrication to measure biorecognition events

like protein detection using antibodies [4, 12] or hybridization [13].

In order to use these devices as biosensors the biological part is equally important. Biological molecules for detection are highly specific for certain target molecules and define the specificity of the whole biosensor. The selection of these so-called receptor molecules for affinity sensing is carried out according to the aimed application (*e.g.* virus sensing or DNA hybridization). These receptors have to be localized closely to or at the sensor surface for signal transduction by the transducer to a final optical or electrical readout signal. The stability of this molecule on the sensor surface is thus the main issue. Common receptors in the past have been antibodies which exhibit a high specificity [4, 9, 12, 14, 15].

A relatively new class of receptor elements are aptamers [16]. Aptamers are short oligonucleotides (single-stranded DNA). These so-called *artificial antibodies* are identified and synthesized in the laboratory. DNA is a robust material which might improve sensor stability. The easy synthesis of these aptamers and possible attachment of functional groups is significantly reducing the costs compared to antibodies and allows for oriented immobilization on the sensor. Aptamers are also not limited to a certain group of targets, but can be identified against a wide range of targets from short organic molecules like TNT or Daunorubicin [17, 18] to proteins for diverse disease treatment [19]. A special feature of FETs is that these devices, run in ionic solutions, are only sensitive within a short distance from the surface, the Debye layer. With respect to FET biosensing, the smaller size of aptamers compared to antibodies fulfills the need for small receptors to assure a high sensitivity. Despite these advantages, only little work has been published implementing aptamers in SiNW sensors [20, 21]. For this thesis, the focus was on the development of 'aptasensors' [22] – *i.e.* aptamer based biosensors – to fill this gap.

For all the different applications, interface engineering and biochemical functionalization of the transducer surface are crucial for affinity biosensor development to assure an excellent sensor performance. Requirements are a stable receptor attachment under varying conditions while preserving the functionality of receptors at the same time. Additionally, binding strategies will enhance the receptor orientation towards the target in solution whereas blocking protocols try to avoid unspecific attachment to reduce background signals.

The main focus here is on the biochemical functionalization of silicon dioxide surfaces and the evaluation of receptor-analyte interactions with the immobilized receptors using optical, gravimetric and finally electrical sensing methods for the goal of a SiNW based FET.

## Scope of the thesis

This work is facing boundaries between the biological sensing element and the identification of novel receptors on one side (Ph.D. thesis in preparation by C. Pahlke) and the sensor chip development implementing bottom-up grown silicon nanowires for the use in ionic solutions as biosensors on the other side (Ph.D. theses in preparation by S. Pregl and F. Zörgiebel). The goal is to link these components together for the purpose of biosensing. This requires research at the edge of materials

science, biochemistry, biotechnology, physics and electrical engineering.

Common receptors like DNA or antibodies display a small number of different groups which are suitable for further attachment at their surface or can be attributed with them. Typical functional groups of biomolecules are primary amines, carboxylic acids, thiols or aldehydes. Thus, attachment strategies usually involve the reaction with one of these groups for covalent attachment. Finding different chemical surface functionalization routes for each of these functional groups allows for a set of building blocks that can be adapted to each new target in terms of length and chemical group. This strategy is thus versatile for new biosensor developments. However, each receptor might behave differently upon reaction with surface-bound linkers. After evaluating and characterizing the surface chemistry and the receptor attachment, the functionality of the receptor is probed by specific interaction with the target molecule.

These receptor-analyte interactions are the next step in sensor development for reliable performances. The surface design includes both, receptor immobilization and overall transducer surface treatment. Receptor densities, analyte concentration limits as well as blocking strategies can be investigated. Finally, all steps and the protocols on planar surfaces will be transferred to the curved surface of nanowires and integrated into the chip fabrication route. Here, degradation of layers and materials due to attachment protocols are taken into account which leads to changes in the previously developed modification. Application of all functional steps in the biosensor itself is therefore a critical step.

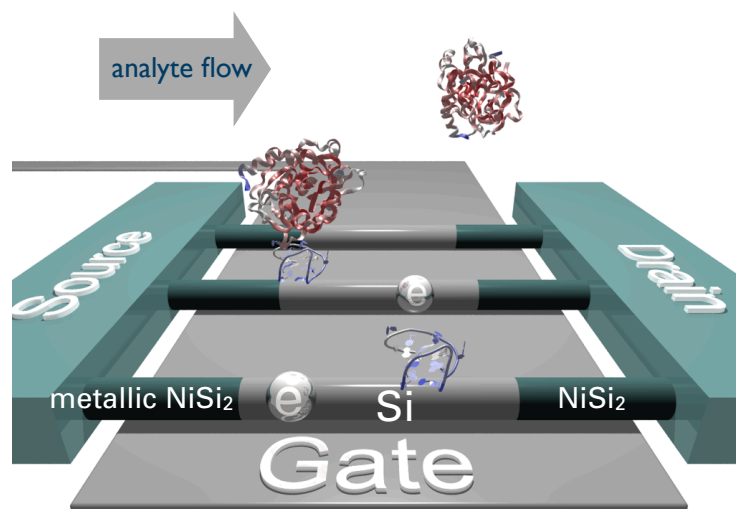


**Figure 0.1.:** Schematic drawing of Schottky barrier based silicon nanowire FET with attached thrombin-binding aptamers by D. Nozaki. Thrombin in solution is flushed over the device and attaches to the functionalized surface.

As a model system, the detection of the protein thrombin was selected. Thrombin was the first target molecule for which the identification of an RNA aptamer was published [16]. The interaction of slightly later discovered DNA aptamer with thrombin is relatively strong with dissociation constants in the nanomolar range (1.6-200 nM) [23–25] and the structure formation of the aptamer rather stable which makes it an ideal model for aptasensor development for the goal of application in the SiNW

FET sensor as schematically drawn in Figure 0.1. Attachment was carried out on planar (wafers and glass slides) and curved (SiNWs) substrates for reference studies, all with terminal silicon dioxide. This work shows why silanes are especially suited for attachment to oxidized silicon or glass and how they are brought onto the surface. The introduction of surface patterns helped to characterize the modification individual steps.

The fundamentals **chapter 1** first introduces the general concept and terminology of a biosensor and gives a small introduction to current technologies. A sensor comprises of an inorganic transducer, a biological receptor for the aimed application which is attached via biochemical strategies. A separate section is dedicated to each of these sensor building blocks. According to the findings in previously published research, the strategies for surface functionalization to attach amino-terminated receptors were chosen and are described, see **chapter 2**. The targets which will be used within this theses – thrombin and amoxicillin – are then presented. This is followed by a list of the used materials and an overview of the fabrication and characterization techniques mainly carried out. **Chapter 3** explains and discusses the strategies to detect thrombin via aptamers in a sandwich assay on patterned surfaces and amoxicillin in an antibody-based inverse competition assay. The results of the biochemical functionalization are the focus of the **chapter 4** confirming the specificity and success of the individual steps. Moreover, this chapter is dedicated to the interactions between receptors and analytes in solution as well as after immobilization on the solid support. Thrombin biosensing is confirmed optically. The antibody based sensing of amoxicillin is then presented. The third section makes an excursion to wrap silicon nanowires which are dispersed in solution in a lipid bilayer shell to create one-dimensional bilayers. Implementation of the aptamers and subsequent thrombin detection using the bottom-up FET sensor with Schottky barriers is presented and the findings are discussed in the final **chapter 5**. The second application (amoxicillin) is investigated on top-down fabricated nanowire FET. The last part summarizes the thesis work and analyzes future perspectives.



# 1. Fundamentals

The development of biosensors combines different fields of research. This chapter is thus divided into four parts presenting these fields. The first section generally introduces the conceptual setup of a biosensor. Various receptor molecules defining the application of the inorganic sensor are available. The section on receptors introduces aptamers and antibodies as they were investigated and implemented in the sensor. These receptors are specific for a single target molecule. The conjugation of biochemical molecules via different routes is discussed in the next section on surface functionalization routes. Then, the electrochemical transducer, a silicon nanowire based field-effect transistor (SiNW FET) is introduced for the use as a biosensor. Finally the chapter is summarized with respect to the applied techniques.

## 1.1. Introduction to Biosensors

Biosensors are analytical instruments which use biological recognition of an analyte and convert this event into an electrical signal with a physicochemical device [26]. A biosensor aims at detecting the presence of an analyte like antigens or single-stranded DNA (ssDNA), see Figure 1.1 on the left side. It is composed of two components. The biological part – the receptor – is responsible for the specificity of the sensor towards the analyte, see Figure 1.1. Most common receptors are enzymes, antibodies or nucleic acids. The receptors are localized at the transducer surface. A transducer is a technical device that is able to detect the local physicochemical changes via optical, mechanical or electrochemical properties upon analyte binding. The biosensor is connected to a signal processing unit which converts these changes into an optical signal like a colour change or an electrical signal like an intensity value, mass change or conductance change that is readable for the user. Depending on the physicochemical type of recognition or reaction, the sensors are classified, *e.g.* as affinity (biorecognition), enzyme-mediated or chemical sensors etc. [27]. To gain more information and overview over the broad field of biosensing, the different biosensor types and applications, the reader is referred to the following book [27] and review articles [22, 28–34].

The most common biosensor application already commercialized is the glucose sensor for diabetes treatment with approximately 85 % of the entire market [35]. Glucose sensors are mostly based on the detection of oxygen that results from an enzyme-initiated process. Miniaturization and simple handling allow for self-monitoring by patients and individual medication which is also desirable for many other biosensors. Other applications for sensing of *e.g.* virus or bacteria related diseases, cancer biomarker detection, DNA sequencing or NBC weapons are still under broad investigation to go from research to commercialization and from laboratory equipment to portable devices. Some of the current

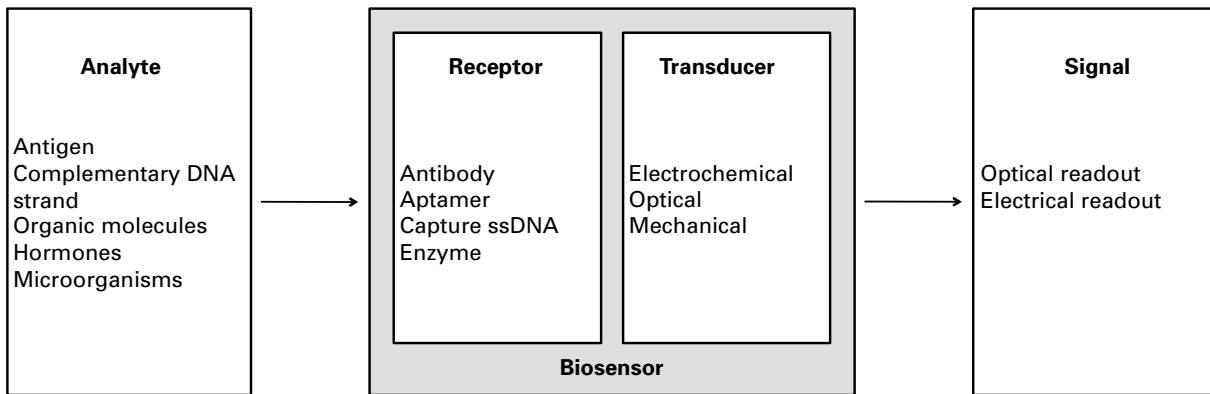


**Figure 1.1.:** Schematic drawing of the setup of a biosensor.

technologies like PCR (polymerase chain reaction), cell culture, cytometry, immunoassays or mass spectrometry are highly specific and established. However, the main disadvantages are sensitivity, the instrument sizes, speed of detection of roughly around 24 h due to complicated sample treatment and reaction time or the need for trained professionals [28, 36]. Thus, the development of real-time, label-free, portable, low-cost, flexible and reliable sensors with lab on a chip systems are the main goals. Further requirements to evaluate novel biosensors are their sensitivity to detect low levels of the analyte, selectivity to avoid false positive signals and a fast response time that allows for rapid diagnosis. In terms of fabrication, the integration into existing technologies and production, the versatility of application and the possibility to produce at low costs are crucial. Reversibility of the biosensor would allow for repeated measurements to improve comparability [36].

The integration of nanomaterials into transducer concepts is one of the possibilities to meet certain of the abovesly listed requirements especially in terms of miniaturization and sensitivity due to their high surface-to-volume ratio and the confinement within the nanometer scale in at least one dimension which leads to changes in the physical properties. Especially silicon nanowire based field-effect transistors (SiNW FETs) fulfill many of these requirements. The use of nanomaterials and the possible integration into Si wafer processing technology enables miniturization of devices at low costs. The immediate current jump upon physicochemical changes without need for analyte labeling meets further requirements (real-time, label-free). Sensitivities down to fM-aM values of analyte concentration in liquids prove the high sensitivity (see references in Table 1.1). Table 1.1 shows different applications as examples for the device versatility.

SiNW FET devices have been investigated for biosensing purposes since 2001, proposed by Lieber group [7] ( see the Introduction ). Since then, number of publications has exploded. An overview table summarizing a selection of published systems and applications can be found in Table 1.1, inspired by Curreli *et al.* [37] and Lehoucq [36] and further extended. The emphasis here is on the attachment strategies for different antibodies and ssDNA acting as receptors.

**Table 1.1.:** Attachment strategies on SiNW FETs. Gas phase (g) or liquid phase (l) attachment of the first step is indicated. The abbreviations for materials can be found in Table 2.2. Additionally the following abbreviations are: GA (glutaraldehyde), TD (top-down) and BU (bottom-up). The table is adapted from Curreli and Lehoucq [36, 37]. The emphasis here is on the attachment strategies for the receptor.

Functionalization strategy	Receptor & functional group	Analyte	Sensor type	Sensitivity	Source
APTES	biotin	streptavidin, anti-biotin	BU p-Si	10 pM	Cui [7]
aldehyde silane	anti-hemagglutinin	influenza A, anti-adenovirus group III	BU p-Si	single virus	Patolsky [9]
t-boc protected amine	anti-IgG antibody	IgG antibody	TD n-Si, p-Si	100 fM	Stern [14]
APTES, GA	mouse IgG antibody	anti-mouse IgG antibody	TD n-Si	n.a.	Hsiao [15]
APTES, GA	antibody	AFP (alpha fetoprotein)	TD n-Si	10 pg/ml	Rim [4]
Trimethyloxy-silane aldehyde	NH <sub>2</sub> -PNA	complementary DNA strand, hepatitis C	TD n-Si	10 fM	Gao [38]
APTES	COOH-DNA	complementary DNA strand, H1N1/N5N1	TD n-Si, p-Si	1 fM	Gao [39]
APTES, GA	NH <sub>2</sub> -DNA	complementary DNA strand, gene sensing	TD n-Si	100 fM	Zhang [40]
APDES (l), SA, EDC/NHS	NH <sub>2</sub> -aptamer (DNA)	Thrombin	BU p-Si	330 pM	Kim [20]
APDES (l), SA, EDC/NHS	NH <sub>2</sub> -aptamer RNA	VEGF	BU n-Si, p-Si	1.04 nM (n-Si), 104 pM (p-Si)	Lee [21]

## 1.2. Biorecognition

### 1.2.1. Biorecognition principles

Target molecule and receptor are interacting partners in a biorecognition process. Receptors are molecules responsible for specific identification of target molecules. The molecular recognition of an analyte due to the interaction of a specific receptor has many facets in nature ranging from chemical over photoactive or electronic to magnetic receptors. In biosensorics mostly biochemical receptors are used for technological purposes. Examples for biorecognition are enzymes and their reactions, microorganisms, antibody-antigen interactions and artificial key-and-lock principles, dyes, lectines, receptors for hormones and many more [41].

The process of biorecognition is a noncovalent form of interaction between two different molecules.

The binding develops an equilibrium of association and disassociation of the two partners. Despite of its noncovalent nature the interaction can be relatively strong as it is the case for biotin-streptavidin interaction with a dissociation constant  $K_d$  of approximately  $10^{-14}$  M [42]. The driving force is a key-and-lock principle based on hydrogen bonds, salt bridges, hydrophobic interactions, van der Waals forces, electrostatic interactions and structural fitting [27]. Antibodies are natural receptors in the immune system to prevent or heal from diseases. For technological purposes also artificial receptors can be designed and applied, like aptamers. This work gives an example for the use of antibodies, but the main focus is on the application of aptamers in biosensing which will be discussed more in detail in the following, see section 1.2.2.

### 1.2.2. Receptors

#### Antibodies

Antibodies are biological molecules which bind to defined target sites with high specificity. In Figure 1.2 the different roles of antibodies in the human body are visualized. The scheme gives an insight into the many possible applications for biosensing. They are built from two heavy and two light chains (Y-shape, see center of Figure 1.2). The Fc end consists of two heavy chains and its sequence and structure is fixed within a class of antibodies, *e.g.* the group of Immunoglobulin G (IgG). Ideally, this part is used for attachment to surfaces. The Fab end contains twice the variable region that specifically recognizes the target molecule. Thus, each antibody can theoretically bind two molecules. The Fab ends are able to adapt to new pathogens and thus support the immune system to recover. Antibodies can be produced nowadays from animals like mice or rabbits in laboratory conditions and further integrated into biosensors. Two groups of antibodies can be distinguished. The term 'polyclonal antibodies' defines a pool of different antibodies enriched in animals that are all specific for the same analyte but different epitopes. An epitope is a distinct part of the target molecule. 'Monoclonal antibodies' are produced *in vivo* as well as *in vitro*, are all identical and only specific for one epitope [43].

Antibodies possess high specificities against their targets and deliver reliable results. However, main disadvantages of antibodies are their sensitivity to changes in the environmental conditions, like temperature or pH. Modifications like dye labeling might affect their tertiary folding structure and thus antibodies can lose their affinity. Labeling is also technologically challenging. As animals are required for production of antibodies the costs are relatively high and ethical questions have to be considered. Immobilization can affect the folding as well [45]. As most antibodies possess different possible attachment sites like amino groups, oriented attachment is a challenge. Oriented attachment can be achieved *e.g.* with physisorption of Protein A that binds to the Fc end of many antibodies [46], see also section 1.3.1. This is a universal route for many antibodies and orients the antibody in the desired direction with the recognition sites towards the analyte in solution. When longterm stability comes into play which is a requirement for biosensor products, antibodies are presumably not the ideal choice as they lose their activity when not stored in liquid or at low temperatures. The

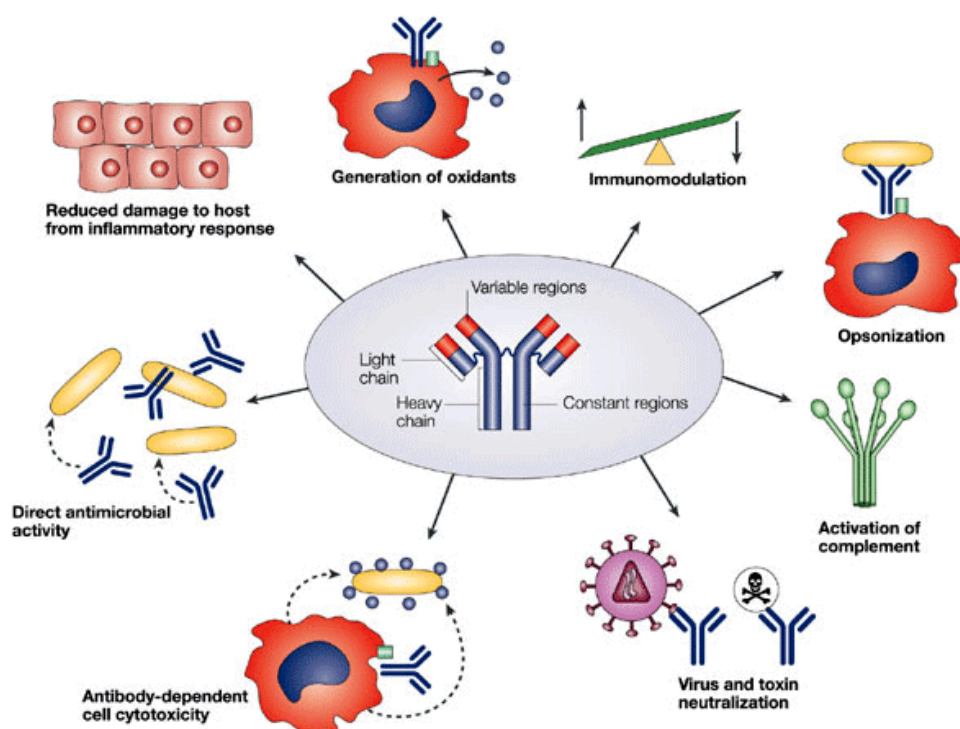


**Figure 1.2.:** Different biological effects of antibodies are summarized in this overview from neutralizing viruses and toxins to regulation of the cell cytotoxicity. In the center, the basic setup of an antibody is displayed. The heavy chain end, labeled as constant region, is called Fc end. The variable region exists twice and is composed of heavy and light chain (Fab end) [44].

application of antibodies is also limited to certain analytes. Very small organic molecules or large cells cannot be detected [22]. Since the use of SiNW based FETs, mostly DNA hybridization and antibody based sensing was published. By introducing concepts for packaging and lab-on-a-chip technologies for immobilization directly before sensing, the use of antibodies will be more applicable.

Secondary antibodies are a group of antibodies able to detect the Fc end of a class of antibodies, *e.g.* IgG. These secondary antibodies can be used for labeling successful recognition events. Usually, they are attributed with a label leading to a colour signal (enzyme mediated colour in enzyme-linked immunoassays (ELISA) [47], fluorescent dye) or conjugated to nanoparticles (mostly gold NPs) for investigation with SEM [4].

## Aptamers

**DNA aptamers** Aptamers have firstly been described in 1990 as a new class of receptor molecules [16]. These artificial ligands consist of short oligonucleotide strands (RNA or DNA) with a length of usually 15 up to 100 bases. The sequence of the bases leads to a characteristic structure formation - like quadruplex for guanine-rich aptamers, hairpins or helical segments [48]. The structures are stabilized via hydrogen bonds, electrostatic and van der Waals interactions between the nucleotides and towards the target. The aptamers are thus able to specifically recognize a certain target molecule

at a typical binding site due to threedimensional interaction. The presence of certain ions like  $\text{Na}^+$  or  $\text{Mg}^{2+}$  is believed to influence and stabilize the structure [47, 49]. According to Ellington, DNA aptamers are more stable than RNA aptamers [16].

Receptor development, *i.e.* the identification of new aptamers is carried out in a so-called SELEX process. The *in vitro* selection method SELEX (Systematic Evolution of Ligands by Exponential Enrichment) is a process of several rounds to separate good target binders from unspecific sequences out of a ssDNA library. In Figure 1.3 a typical SELEX round is schematically drawn. Each oligonucleotide in this pool has the same length consisting of a randomized sequence in between fixed sequences on both ends. They are used *e.g.* for attaching the DNA during SELEX on solid supports. The four different bases G, T, A and C (guanine, thymine, adenine and cytosine) result in libraries of typically  $10^{13}$ - $10^{18}$  different combinations [22]. The selected library is incubated with the immobilized target in a first step, unbound DNA is washed away. By changing the solution, bound molecules are eluted, followed by an enrichment step and are again incubated with the target. By repeating several rounds it is possible to identify unique sequences for detection. For each target, the SELEX has to be adapted individually. Some aptamers show a better performance when used with their fixed sequences in biosensors as the situation is closer to the conditions during SELEX. Since the first SELEX, several variations have been developed. In order to identify aptamers for small target molecules which cannot be immobilized on the plate, Stoltenburg *et al.* published a process called Capture-SELEX to attach the potential aptamer strand onto magnetic beads via hybridization with a short complementary strand [50]. In case a very strong affinity occurs between the target and the aptamer, dehybridization takes place and the aptamer gets released from the magnetic bead. By this, only excellent binders, *i.e.* aptamers, are selected. Dissociation constants between proteins and aptamers are in the nano- to picomolar range whereas with small molecules like dyes the constants are typically in the micromolar range [51].

To overcome the disadvantages of antibodies – mainly costs, restricted variety of targets and stability without losing specificity – the development of aptamers plays a key role. Aptamers can be selected for a huge variety of targets ranging from ions [53], small chemical molecules like TNT [17] or daunorubicin [18] and proteins like thrombin [23] to cells [54]. Aptamer development is also possible against toxins which cannot be realized with antibodies as they do not elicit an immune response [19].

DNA is also much more stable under varying conditions such as changes in pH, temperature or in non-physiological conditions. DNA strands can be easily synthesized *in vitro* at high purification standards without the need for animals and thus show little batch-to-batch variations. Modifications with functional groups for attachment or fluorescent dyes are standard methods and may be introduced without a loss in affinity to the target [22, 30]. The 3' and 5' ends can both be used for functionalization with reactive groups such as amino, thiol or biotin for receptor attachment and fluorophores for optical recognition. Modification of 5' is easier and thus cheaper whereas the 3' end is targeted more easily by nucleases. Thus it is of advantage to link the aptamer via the 3' end. Adding sequences that do not participate in the recognition, so-called spacers which mostly consist of nucleotides or carbon chains  $((\text{CH}_2)_n)$ , and optimizing their length helps to attach functional groups or fluorophores and thus

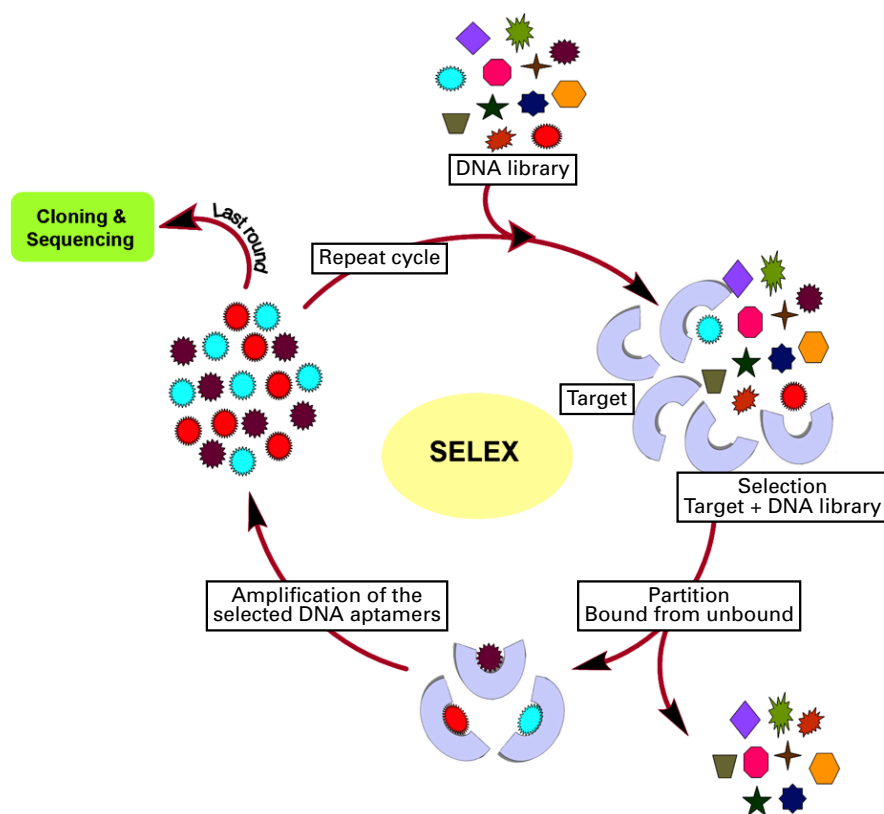


**Figure 1.3.:** Schematic drawing of traditional SELEX procedure, taken from [52] and modified.

improves the sensor performance as it separates the binding or functionality from the actual folding region [55, 56]. Because of its robust nature, regeneration of an aptamer based sensor after detection is possible by incubating the sensor surface with appropriate solvents like 1-2 M NaCl or by heating until the aptamer folding is destroyed and subsequent cooling [57, 58].

By only using one single functional endgroup, the aptamer can be oriented in a favourable way. DNA can be provided with terminal primary amines in the synthesis process. This is rather specific as they do not display other primary amines in their 4-bases structure as proteins or peptides consisting of amino acids do [59]. All aptamers can attach the same way and not randomly which should enhance the sensor performance. Also drying periods do not destroy the DNA immediately, it is widely known how stable DNA is. The threedimensional structure formation of aptamers can be denatured with elevated temperature treatment or by the use of regeneration solutions and regenerated which is a key advantage for the application in reusable biosensors and different assay designs. DNA in general is negatively charged in a wider pH range due to the low iso-electric point (pI). Thus, suppression of unspecific adsorption is facilitated compared to proteins by using repulsion due to electrostatic interactions [59].

A key advantage with respect to application in field-effect transistors (FET) is the small size of an aptamer [60]. Figure 1.14 illustrates the dimensions of an antibody and an aptamer layer in comparison to the sensitive Debye layer. Outside of this layer, no sensing is possible with FETs run in liquids (more details see section 1.4.3). With a size of only 1-2 nm, it will be possible to run the aptasensor in ionic concentrations in between 1 to 10 mM to support biological structure formation and interactions while improving the sensor performance, whereas antibodies require much lower concentrations to remain with the sensitive layer.

The disadvantage of aptamers is that the sequences first have to be identified in this rather long and complicated process with multiple steps that need to be optimized individually (SELEX for aptamers, Phage display biopanning for peptides). Comparing selected sequences out of different SELEX procedures helps to identify *e.g.* plastic binders which lead to wrong positive results. The attack of nucleases which destroy the DNA lead to concerns about the stability of the aptamers. Therefore spiegelmers have been developed which are not degraded by nucleases [61]. As each aptamer is only composed of four bases the aptamer diversity might be limited in terms of their very similar and low pI and hydrophilicity which makes it difficult to identify aptamers for negatively charged or hydrophobic targets [30].

As introduced earlier, aptamers exhibit different structures due to their sequences like quadruplex for G-rich oligonucleotides. The sketch in Figure 1.4 shows how the G-rich parts interact with each other due to hydrogen bonds and build a relatively stable three-dimensional molecule in the case of thrombin binding aptamer with 15 bases [62]. It forms a quadruplex structure with two G quartets, arranged in three lateral loops. The application of thrombin sensing will be discussed more in detail in section 3.1. Other aptamers show loops or hairpins due to partial dimerization which requires a thermal pretreatment for proper folding. The weaker the structure, the more important this temperature treatment is. To assure a high yield, DNA strands are typically heated up to 90°C in a short time (minutes) and then cooled down slowly to room temperature where the structure is maintained [17].

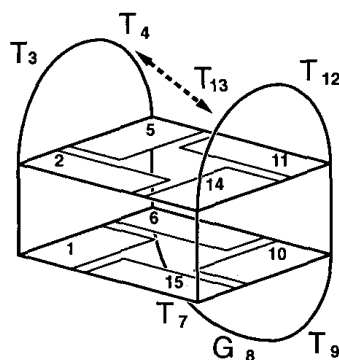


**Figure 1.4.:** Schematic drawing of the thrombin binding aptamer quadruplex formation shows the position of Gs (1, 2, 5, 6, 10, 11, 14 and 15) forming two stacked quartets and the lateral loops with mainly T involved [62].

Since reported, aptamers have gained increasing interest in the development of biosensors (impedance spectroscopy [63, 64], SPR [58], QCM [65], FET [20]). The interaction of the protein thrombin with



several DNA and RNA aptamers has been investigated, see also [23, 25, 47, 57, 66]. In addition, the aptamers for the growth factors PDGF and VEGF were dominating the published literature [21, 67–70] and are part of most overview articles [19, 29, 71, 72]. Other examples are the following aptamers and the used biosensors: detection of IgG with electrochemical impedance spectroscopy (EIS) [73] or daunorubicin detection using fluorescent dye- and enzyme-linked aptamer assays (FLAA and ELAA) after identification in ELISA [18]. To date, only little research on SiNW (or semiconductor) based aptasensors has been published. There is however an increasing interest for application in silicon nanowire based sensing due to their advantages for FET based sensors. Because of their smaller size compared to antibodies, biorecognition can take place much closer to the sensor surface within the Debye screening length at relatively high ion concentrations which is favourable for structure formation of receptor and target molecules, see Figure 1.14. Elnathan *et al.* used only antibody fragments to measure closer to the transducer [12]. The same effect can be obtained by using aptamers. Control experiments with DNA could also be carried out easily by reference measurement of control DNA instead of the aptamer or by competing hybridization with target recognition. In addition, as previously stated, their stability might lead to a better integration in chips for biosensing.

**Peptide aptamers** So far, the term 'aptamer' was reserved for DNA based receptors. Artificially synthesized peptide strands can also be called 'aptamers'. Their identification procedure, namely biopanning, is based on a library of phages that display peptides. This phage display biopanning is a similar process to SELEX, but for the development of peptide based aptamers [74].

Peptides consist of aminoacids. Phages are used as carriers of the randomized peptide sequence. Phages are viruses that infect bacteria and use them as a host to grow. The group of M13 phages *e.g.* are filamentous with  $\mu\text{m}$  lengths and a diameter of 6.5 nm [75]. They consist of different coat proteins (major and minor coat proteins) and both can be used to display additional randomized peptide sequences. The length of these additional proteins is constant for one library and thus predetermines the aptamer length. Phage libraries typically offer  $10^9$ - $10^{11}$  different aminoacid combinations [76]. All biopanning steps as well as the library have to be chosen individually. The cycle of binding, washing, elution and amplification (similar to SELEX) has to be designed and adapted to the target depending on *e.g.* its size or outer charge. After several rounds (mostly within the range of 2 to 6 rounds), the DNA of the obtained phages is analyzed in the region responsible for the aminoacid sequence of the selected protein sequence. Thus, *in vitro* synthesis of peptide oligomers with additional functionalities similar to DNA aptamers is possible, although still more expensive.

Advantages compared to DNA aptamers are the higher stability in terms of attack by nucleases and the possibility of direct integration of phages in biosensors [77] as they can be amplified easily with the help of bacteria growth which is a cheap and fast method. So far, numerous peptide aptamers have been identified, *e.g.* aptamers for the inhibition of hepatitis B virus capsid formation [78], cell cycle analysis or bacteria detection [74, 79] have been published.

Within this chair, peptide aptamers against norovirus are under development (Ph.D. thesis in preparation: C. Pahlke). Norovirus causes severe gastroenteritis especially in hospitals and on cruise

ships, locations where the virus can spread easily. The disease is rapidly transmitted via airborne infection and a lack of strict hygiene measures. Disease spreading could be avoided if virus recognition happens as quickly as possible. Therefore, a fast and label-free screening method for direct biosensing as it could be offered via FET sensing is a desirable goal for health care applications.

### 1.3. Surface Functionalization

The aim of surface modification or functionalization for applications in biosensing is to localize receptors in proximity to the transducer surface in order to achieve high sensitivity. The success of the functionalization strategy is essential for the sensor performance. Main goal is to reliably attach the receptors to achieve a sensor with a stable capture layer while preserving the function of receptors towards the target. An immobilized receptor molecule is here affected by the ability to build its structure because of steric hindrance at high receptor densities and the binding mechanism. Receptor orientation towards the analyte solution ensures the accessibility for the target molecule. The overall biochemical surface treatment hinders unspecific adsorption which reduces the background noise.

Receptors can be attached to surfaces using a variety of mechanisms. Commonly, receptors are not directly bound to the inorganic transducer surface but via linker molecules. Reasons for this are that the functional groups for potential attachment are often not yet chemically compatible with the present surface end groups. In addition, the sensor performance usually improves at a certain distance from the surface [80]: close to the surface, binding and surface terminal groups may disturb the receptor folding. Long linker molecules are possible for techniques like surface plasmon resonance or quartz-crystal microbalance but not applicable for FETs due to the Debye layer thickness (see section 1.4.3). Issues like the undesired unspecific adsorption can also be addressed by designing a functionalization strategy. Unspecific adsorption leads to an increased background signal. To summarize, a molecular layer on the sensor surface with the required functional groups and properties may provide the conditions that allow for attachment of an active ligand. By this, biorecognition can take place at the surface. The choice of this layer or linker molecule depends on both, the sensor surface and the available functional groups of the receptor. This heterobifunctionality can be achieved in one or several steps. The general aim is to create a two-dimensional functionalization layer.

Consequently, the key requirement of a linker (system) is to bring the biomolecule onto the inorganic surface. Biological receptor molecules mostly offer terminal groups like primary amines, thiols, carboxy or aldehyde groups or can be designed *in vitro* with these additional functionalities. Most common surfaces in biosensing applications are noble metals, semiconductors or oxides. Among the possible mechanisms to attach any molecular layer or chemical linkers to the substrate is physisorption. Physisorption summarizes interactions based on relatively weak mechanisms due to van der Waals forces, electrostatic or the much stronger hydrophobic interactions [81]. These processes are however reversible. Stronger binding occurs when linkers are chemisorbed, non-oriented or via oriented covalent binding. Another option is to make use of the high affinity of streptavidin and biotin for surface functionalization. Receptors like DNA, peptides or molecules like lipids are commercially available

with attached biotin. Additional ways where receptors are incorporated in polymer matrices is not part of this thesis. This section discusses the strategies and challenges of surface functionalization with the main focus on concepts suitable for SiNW FET sensing.

The length of the linker between surface and receptor can be varied. Short linkers may be required when the biorecognition, *i.e.* a biochemical process, needs to be converted into an electrical signal in close proximity to the surface due to the distance dependent sensitivity of environmental changes. Close to the surface however the receptor is increasingly influenced which might lead to a change in the structure formation. Longer linkers also have the tendency to form better ordered monolayers. As stated in 1.4, the ionic concentration of the used buffer determines the Debye screening length in the experimental setup. A biorecognition event is only recognized within this distance. Thus, low salt concentrations are required to increase the sensitivity of the sensing system using SiNW FETs. So a tradeoff depending on the system under investigation is required to decide for the linker length. Handling with ionic concentrations at the lower limit can thus increase the sensitive layer thickness and maintain appropriate buffer conditions for biorecognition at the same time. In addition to the length, the receptor density plays a role. Low densities reduce sensor performances due to the low probability of a detection event. High densities on the contrary might come along with steric hindrance so that the receptors' tertiary structure might be altered. The accessibility of the target molecule can also be influenced in case they are big in size compared to the individual receptor.

For this work, functionalization strategies were investigated in parallel to the development of a silicon nanowire based FET sensor for the use as a biosensor. Silicon nanowire or wafer surfaces are oxidized in ambient conditions. This results in a native oxide shell ( $\text{SiO}_2$ ) of approximately 2 nm (see results in section 4.1.1). Introducing a thermal treatment homogenizes the oxide layer. This possibly increases the reproducibility. The oxide can only be removed by etching in strong acids and silicon oxidizes again after minutes. Thus, two options are available in the case of silicon - silicon dioxide and hydrogen terminated Si (Si-H) after etching. Before designing a functionalization scheme, it is important to decide for the type of surface and surface treatment. The decision here is discussed more in detail in section 2.1.1.

### 1.3.1. Noncovalent methods

#### Self-assembled adsorption layers

Molecules used for functionalization of surfaces can arrange themselves in a parallel and regular way. In dependency of time, solvent, temperature or light the molecules attach to the sensor surface and its chains align in parallel. The driving force during attachment (*e.g.* via physisorption like lipid bilayers or covalent bonding, see section 1.3.2) is to minimize energy at the interface. The resulting self-assembled layers are characterized by their typical thickness of one monolayer (**Self-Assembled Monolayers**).

Lipid bilayers are self-assembled functionalization layers. Lipids are the building blocks of cell membranes. In aqueous solutions they arrange in bilayers due to the structure of the individual lipid

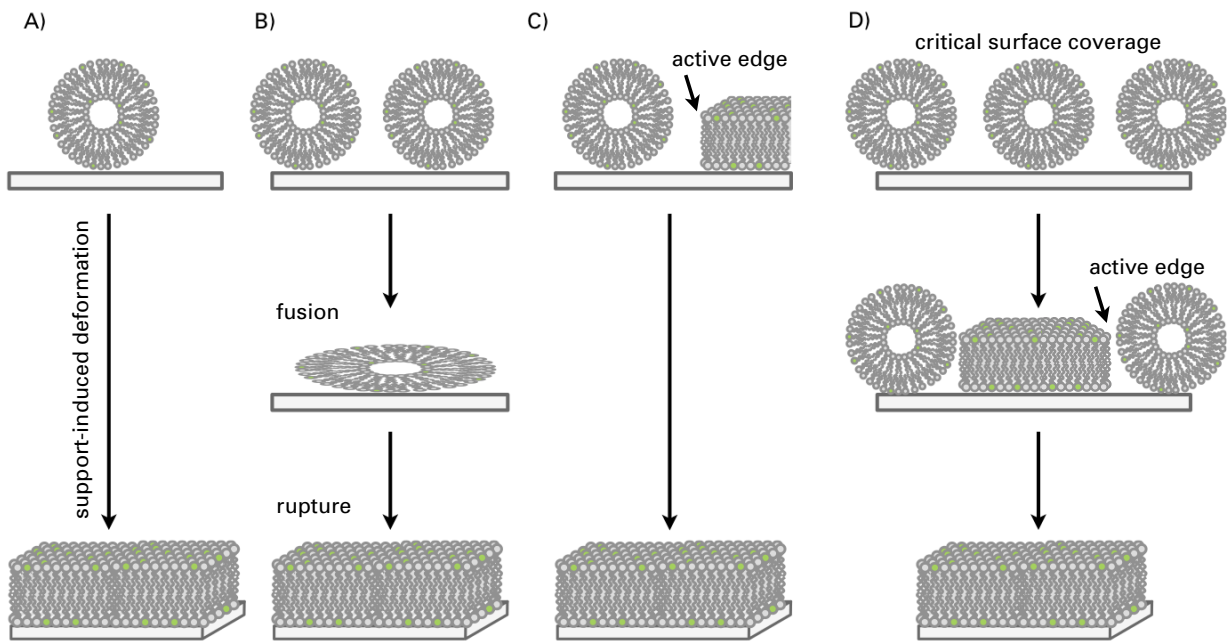


**Figure 1.5.:** Different mechanisms of vesicle rupture (own sketch after Richter *et al.* [82]) . A) Adsorption of an isolated vesicle and spontaneous rupture due to support-induced deformation (support = solid substrate). B) Adsorption of neighbouring vesicles. They fuse together and rupture. C) An active edge of a bilayer patch induces vesicle rupture. D) At a critical vesicle coverage first vesicles rupture. The active edge of the bilayer initiates further bilayer formation.

molecule with a hydrophilic head and hydrophobic tail (circles and curved lines in Figure 1.5) with the heads towards the solution and the tail facing each other. Lipid vesicles are also confined by bilayer shells. These small compartments are used for cell transportation processes and act as nucleation centres for crystallization. Bilayers have been widely used for biotechnology to mimic membranes and in biosensing applications as functional layers [83]. Unilamellar vesicles (ULVs) with a single bilayer shell form bilayers on solid supports via vesicle fusion technique. After adsorption onto substrates, ULVs fuse together and rupture according to various mechanisms suggested by Richter *et al.* [82] to build supported lipid bilayers (SLBs), see Figure 1.5A)-D). The formed supported lipid bilayer patches (bilayer islands) expose active edges leading to further enlargement of the patches until full substrate coverage in the ideal case. These molecules do not attach covalently to surfaces and possess a high recovery capacity due to the mobility of the lipid molecules (fluid-like behaviour). Functional lipid molecules with *e.g.* attached biotin or fluorophores and membrane pores can easily be integrated during the fabrication process for sensing purposes [83, 84]. The bilayers are advantageous in terms of biocompatibility and blocking as they shield *e.g.* the nanowire from unspecific adsorption [59]. Lipid bilayers have been used so far for detection of ions as certain ions cause the intergrated pores to open. This local change in environment on the nanowire surface leads to high signal change in the measured conductance [83].

As stated in my paper from 2013 [84], lipid bilayers as biological materials have already been used to functionalize surfaces for biosensing, *e.g.* in quartz-crystal microbalance measurements [85], on

metal oxide semiconductor FETs [86] or SiNW based FETs [83]. With the incorporation of membrane proteins that form pores with regard to chemical changes in the surrounding media, biological processes like enzymatic reactions can be monitored [83]. Lipid bilayer coating of nanowires could also be important to provide biocompatible surfaces when electrical characteristics of single cells are measured using kinked nanowires [11, 87, 88]. Bilayers have potential to mimic cell membranes in the study of transportation mechanisms through membrane channels or drug influences on the membrane stability [89]. Furthermore, lipids can enhance the biocompatibility of small particles for medical purposes such as drug delivery [90–92]. The degree of membrane curvature plays an important role for membrane proteins in cells. Curvature changes might influence certain intracellular processes governed by the transport properties of the membrane [93]. Therefore, the coating of curved small objects such as carbon nanotubes (CNTs) [94] or nanowires [95] is also of fundamental interest [96]. Bringing together biological molecules with inorganic nanosized materials offers enhanced functionalities of existing nanoscale devices. Studies on the bilayer formation around the nanowire in solution are discussed in section 4.3.2.

### Other adsorption layers

Protein adsorption is another way to provide functionality for biosensing. As most biomolecules possess surface charges proteins adsorb because of electrostatic interactions. Hydrophobic interactions also play an important role. This procedure can act as a first modification step for further attachment. Streptavidin physisorption was used for the attachment of biotinylated anti-thrombin aptamers to chips for surface plasmon resonance [58] as well as to glass slides for microarrays [97]. Streptavidin offers four binding sites for biotin. The interaction of biotin and streptavidin is also one of the strongest noncovalent interactions [42, 98] assuring stable immobilization. The protein is relatively big (4 subunits of 15,000 Da result in 60,000 Da), covers the sensor surface and improves the signal-to-noise ratio due to less unspecific adsorption (blocking effect). Streptavidin provides a biological soft surface for further attachment of biomolecules which enhances the performance in contrast to the rigid inorganic transducer surface. Thus, streptavidin coating is suited for techniques like surface plasmon resonance (SPR), quartz-crystal microbalance (QCM) or microarrays, where the distance to the transducer does not play a key role as it does for FETs.

Implementation of antibodies as recognition elements is possible via their Fc end which is not involved in the antigen recognition (detailed explanation of the antibody structure see section 1.2.2). It attaches to physisorbed protein A, G or L layers. As this route is specific for the Fc end, it is a strategy to fulfill the requirement of oriented immobilization as the variable Fab ends responsible for recognition stick out into the solution and are accessible for the target molecules [46]. As these are biological molecules with batch-to-batch variations, the binding yield can vary which might make results less reproducible compared to covalent bonding. The total layer thickness is problematic for FET sensors due to the increased distance of the biorecognition event from the surface [12].

### 1.3.2. Covalent methods

#### Self-assembled monolayers

Covalently attached self-assembled monolayers (SAM) are rather homogeneous with a constant thickness. The principal structure of these molecules is composed of the following parts: a head group for anchoring like thiols for SAM formation on gold (see Figure 1.6). This functional anchor group is attached to a chain of identical elements, often alkyl groups. The length of this alkyl chain  $(\text{CH}_2)_n$  influences the parallel arrangement with other molecules. Short molecules lead to more defects in the layer. Elongation of the alkyl chain results in higher stability of the SAM which is favourable in terms of blocking, competes however with the sensitivity in FETs, see section 1.4. With respect to those sensors, the disadvantages of short linkers have to be overcome by additional blocking steps. The third part of the molecules for SAMs are the terminal groups sticking out of the layer which provide functional groups for attachment of ligands.

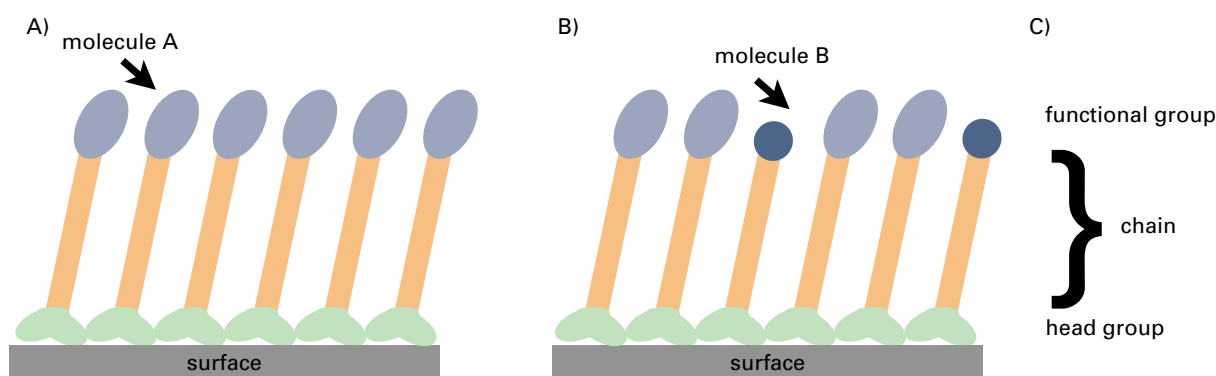


**Figure 1.6.:** Schematic drawing of a typical SAM with headgroup for anchoring to the surface, a molecular chain for parallel arrangement and the terminal group for crosslinker or receptor attachment. A) SAM with one molecule type. B) Mixed monolayer. C) Description of the molecule parts.

The process for SAM formation goes basically through two phases – molecules rapidly cover the surface area resulting in a layer thickness of 80-90 % of the final thickness. The final arrangement however takes place over several hours [99]. Depending on the strength of the binding to the surface, the SAM can also be regarded as a fluid with continuous molecule arrangement as wider distances at low coverage are competing with the energy of holes in the layer, see physisorbed lipid bilayers in previous paragraph 1.3.1. Mixed monolayers with two different molecules can be optimized toward an ideal receptor density by varying the ratios [100]. This strategy still assures that the whole surface can be functionalized and thus blocked against unspecific adsorption. Requirements are that the two types of molecules in these mixed layers do not form islands or networks but are distributed homogeneously. The number of functional endgroups for further attachment also influences the receptor density. Here, a tradeoff between steric hindrance and sensitivity is the main goal for optimal sensor signals.

Functionalization strategies based on covalent bonding between the surface and the molecule anchor

groups offer stable attachment of molecular layers. Covalently linked SAMs are thus the ideal choice for reliable biosensing.

### Organosilanes

Organosilanes are organic molecules for the covalent functionalization of SiO<sub>2</sub>, *i.e.* oxidized Si substrates like wafers or glass substrates. The central Si atom offers four binding sites. The principal structure is summarized in the formula X<sub>3</sub>Si(CH<sub>2</sub>)<sub>n</sub>R. X represents a hydroxyl or hydrolysable group consisting in most applications of alkoxy groups (methanol or ethanol) for attachment to the inorganic surface. The central Si atom and R are linked by a short carbon chain (CH<sub>2</sub>)<sub>n</sub> and R is the terminal functional group for direct receptor or crosslinker attachment. Typical terminal groups for further crosslinker or receptor binding are aldehyde, primary amine, mercapto or epoxy groups (see section 1.2 on receptors). This is crucial to link the inorganic surface together with specific biomolecules in order to create biosensor surfaces able to transduce biorecognition to a readable sensor signal.

In the presence of water, the alkoxy splits from the silane and forms an alcohol, see Figure 1.7A). This process is called hydrolysis and can happen either in solution or due to the presence of surface water directly at the surface. It leads to reactive OH groups attached to the central Si atom (silanols). Attachment protocols using the liquid phase include a time prior to sample incubation for this hydrolysis procedure. The silanols can interact with surfaces equally exposing OH groups via hydrogen bonding [101]. Water is released when the molecules bind covalently to the surface in a condensation process forming stable siloxane bonds (Si-O-Si), see step 2) in Figure 1.7A). The unbound side group silanols can further crosslink by thermal curing [59]. OH groups can easily be created on silicon dioxide surfaces by cleaning in piranha solution, with an oxygen/air plasma treatment [102] or other solutions like NaOH as investigated by Janissen *et al.* [103]. Thus, organosilanes are well suited to covalently link to these OH-terminated surfaces. In theory, the resulting monolayers are well ordered as illustrated in Figure 1.7A) after full attachment. In reality, effects like polymerization in solution (polycondensates), physisorption due to *e.g.* electrostatic interactions and molecular inversion which reduces the number of desired functional groups occur, see Figure 1.7B) [102].

Table 1.2 summarizes the typical functional groups that are possible with organosilanes for attachment of amino groups of receptors. Aldehyde and primary amines form a covalent bond called imide bond which is labile and needs to be stabilized by reduction with sodium borohydrate to form secondary amines. Isothiocyanate terminal groups form stable thiourea bonds but the silane is very toxic, delicate to handle and for biosensing strategies not so common. Epoxy terminated silanes and especially aminosilanes are widely used. Epoxy groups form aminoalcohols with primary amines at pH values higher than physiological pH. Aminosilanes require use of a crosslinker to create carboxy groups that lead to a stable amide bond formation.

### Functionalization principles

For organosilanes, adsorption in the liquid phase (*i.e.* diluted silane) or from the gas phase at elevated temperature or pressure (*i.e.* pure silane) are the two main methods for covalent attachment of

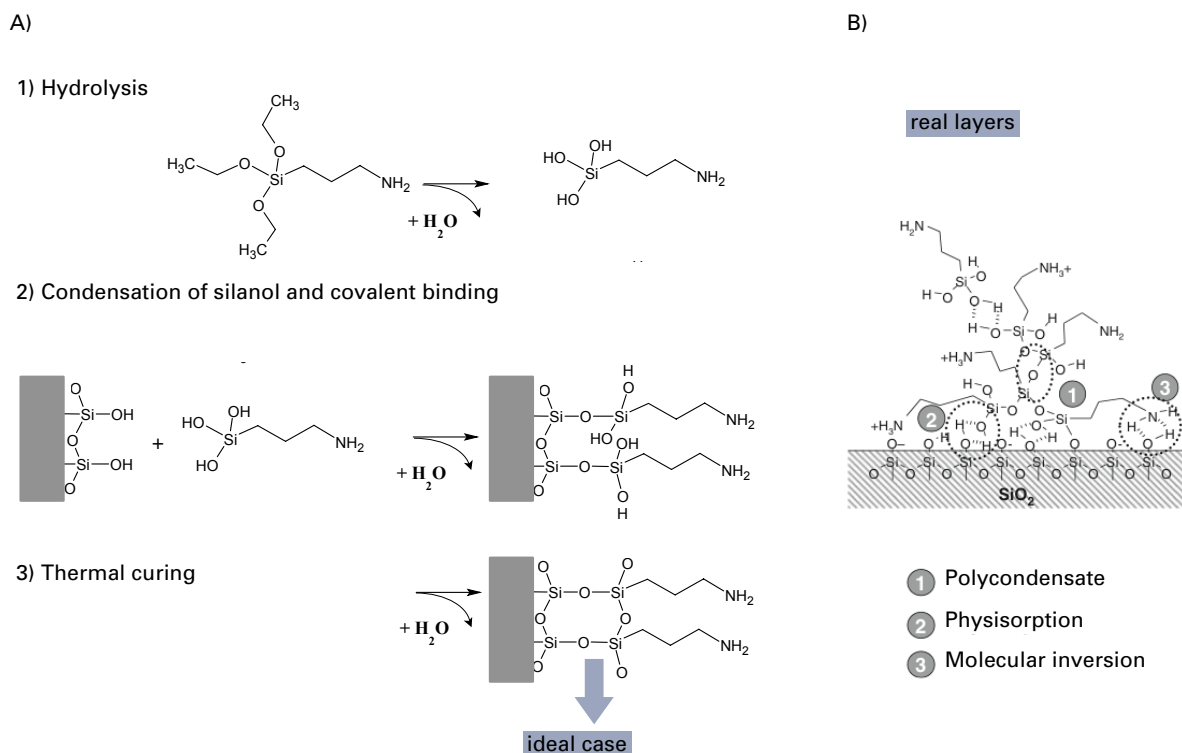


**Figure 1.7.:** A) Chemical reaction for covalent silane binding to hydroxylated silicon oxide surface is a three-step procedure. B) In reality, silanes form irregular layers due to electrostatic interaction, polymerization in solution and molecular inversion, from [102].

**Table 1.2.:** Typical coupling routes after silane attachment to silicon oxide surfaces for crosslinking with amino-receptors.

Terminal silane group	Bond formation with primary amine NH <sub>2</sub>	Reaction	Silane name
NH <sub>2</sub>	imide	via crosslinker glutaraldehyde	APTES, APTMS etc.
NH <sub>2</sub>	amide	via crosslinkers succinic anhydride, EDC and NHS	APTES, APTMS etc.
epoxy	aminoalcohol	direct	GOPEs, GOPMS
aldehyde	imide	direct	11-(Triethoxysilyl) undecanal

organosilanes to silicon oxide surfaces. The choice depends on the specific silane and the requirements of the sample. In liquid phase methods, the presence of three silanols on one molecule leads to polymerization of the molecules in solution under certain circumstances (Figure 1.7B). As the aim is to achieve rather homogeneous layers of approximately monolayer thickness, molecular stacking due to this polymerization is undesired. This can be avoided by using fresh solutions, inert gas atmosphere and control of the involved deionized water and the deposition procedure. Organosilanes



tend to degrade with time in the presence of water in the atmosphere and are handled with care. The advantage of these free silanol side groups is that they possibly crosslink in a postbaking step after surface attachment and stabilize the layer (Figure 1.7A). Gas phase attachment is thus beneficial although molecular stacking on the surface can still be present. These procedures consist of less experimental steps which reduces the risk of damaging or contaminating samples. Another approach is the use of silanes with only one chemically reactive X group whereas the other two ones are replaced by *e.g.* non-reactive methyl groups. This is thought to reduce polymerization and molecular stacking. It also reduces the boiling point which makes experimental procedures for gas phase routes easier. However, crosslinking to stabilize the layers is not occurring which might result in less stable layers. X can also be replaced by halogens. Chloro- or fluorosilanes are highly reactive and play an important role for the creation of hydrophobic surfaces on glass or wafers. They are however not used for the biosensing purposes in this work.

### Crosslinkers

Crosslinkers are a class of molecules capable to link two functional groups together, *e.g.* surface groups and receptors or different molecules in solution. Thus, they are attributed with two functional end groups. They either provide two identical chemical groups or two different ones – called homo- and heterobifunctional crosslinkers [59]. The latter are more specific as homobifunctional crosslinkers cause undesired side effects like crosslinking of surface groups or receptors among each other which actually inhibits the aimed further functionalization, as it can be the case for glutaraldehyde. A prominent example for heterobifunctional crosslinkers is succinic anhydride. This ring structure opens upon attachment to primary amines in aqueous solution and creates carboxy groups. The reaction mechanism and attachment are described more in details in section 2.1.2. In addition, crosslinkers are classified according to their role in the chemical process. Molecules that only form reactive intermediate products but are not part of the later binding are called zero-length crosslinkers [98]. An example is the combination of a carbodiimide (EDC) and N-hydroxysuccinimid (NHS) to activate carboxy groups [104], see Table 2.2 and section 2.1.2.

## 1.4. Silicon Nanowire Based Field-Effect Transistor Devices

### 1.4.1. From FETs to ion-sensitive devices

#### MOSFETs

A field effect transistor is a semiconductor based device used for switching or signal amplification in electrical circuits. FETs consume low power [105]. Widely used transistors are the so-called MOSFETs (metal oxide semiconductor field-effect transistor). Here, two highly doped domains (*e.g.* n-type) are separated by a p-type domain with p-n junctions at the interface, see setup in Figure 1.8A). The n-domains are connected to the source (S) and drain (D) contacts. A metal gate is placed on top of the area between S and D, separated by a thin insulating oxide layer. The conductance is controlled

by an external field, for instance the gate field. By applying a positive gate voltage at the metal gate, electrons are attracted at the semiconductor–oxide interface. Once the threshold voltage is reached, an inversion layer builds a conducting channel between the n-type regions connected to S and D, see Figure 1.8B). The size of this channel depends on both, the external gate field and the selection of the materials. Applying an additional SD bias voltage  $V_{sd}$  enhances the charge carrier movement through the channel and narrows the channel at one end. Thus conductance of the charge carriers is altered (Figure 1.8C). In this case (positive  $V_{sd}$ ), electrons will be attracted by the drain. Common elements for doping of silicon are boron (p-type) or arsenic (n-type).

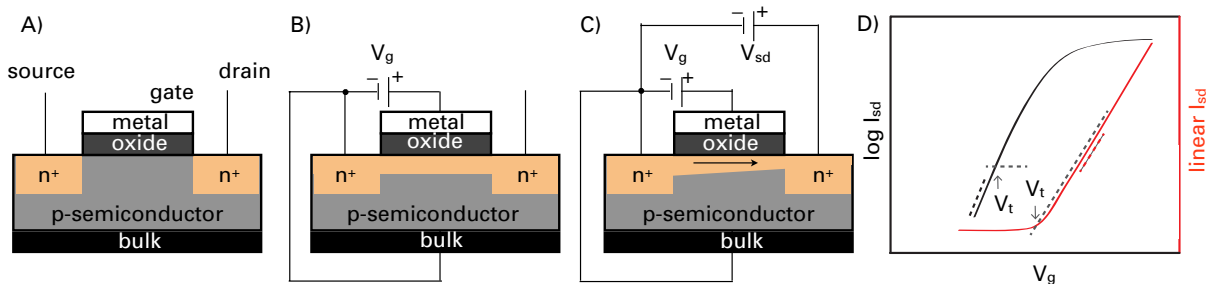


**Figure 1.8.:** Schematic drawing of the principle of a MOSFET, drawing after Tarasov [105]. A) Basic setup of a MOSFET at  $V_g$  and  $V_{sd} = 0$ . B) Applying a positive gate voltage, electrons go from bulk to the semiconductor–oxide interface. Formation of a conducting layer. C) The conduction channel is controlled by an applied positive  $V_{sd}$ . Electrons move to the drain. D) Transfer characteristics  $I_{sd}$  as a function of the applied gate voltage in semi-log (left y-axis) and linear (right y-axis) scale. For both configurations, the threshold voltage is defined. It is found either where the curve is steepest (logarithmic  $I_{sd}$ ) or at the intersections of the prolongation of the linear part with the curve (linear scale).

## ISFETs

Ion-sensitive FETs (ISFETs) are similar to the common MOSFET. Bergveld *et al.* discovered that MOSFETs in direct contact with a liquid solution are sensitive towards protons and thus suitable as pH sensors [106]. For this however, the metal gate is replaced by the electrolyte solution which contains a reference electrode – a so-called liquid gate which can control the current between S and D [105]. For sensing, it is indispensable to include a reference electrode to measure against a stable potential. The conductance in ISFETs depends on the charge situation at the oxide–electrolyte interface. ISFETs are sensitive towards charged molecules in general. Depending on the isoelectric point (pI) of the surface and the pH of the electrolyte, the charging of the terminal surface groups behaves like a local gate. Therefore, it is possible to detect variations in the pH of the solution, *i.e.* taking or giving away protons at the functional interface is sensed [105].

For the transfer characteristics of the devices, the source drain current ( $I_{sd}$ ) is measured as a function of the applied gate voltage  $V_g$  (Figure 1.8D). In semi-logarithmic scale, the steepest slope of the curve is defined as subthreshold swing with the threshold voltage  $V_t$  at which the current is switched on due to the formation of an inversion layer at the interface. At this point the FET switching can happen

at maximum speed. By analyzing this slope which is constant over several orders of magnitude [105], curve shifts at a fixed current due to attached charged molecules can be determined ( $\Delta V_t$ ).

Because of the possible (de)protonation of the surface oxide, pH measurements are usually applied to probe the device performances for potential application in biosensing. By changing the proton concentration (pH change), the surface potential is directly affected and influences the threshold voltage. This is visible as a shift of the I-V curve to lower or higher voltage values (Figure 1.9A). The sensitivity of ISFETs is determined by the maximum possible shift because of a pH change and defined by the Nernst limit at 300 K ( $k$  = Boltzmann constant,  $T$  = absolute temperature,  $e$  = elementary charge):

$$\ln(10) \frac{kT}{e} = 59.5 \frac{mV}{pH} . \quad (1.1)$$

FETs with silicon dioxide surfaces achieve a maximum sensitivity of appr. 45 mV/pH at  $pH > 5$  [107]. The example in Figure 1.9B) exhibits a sensitivity of 35 mV/pH [4].

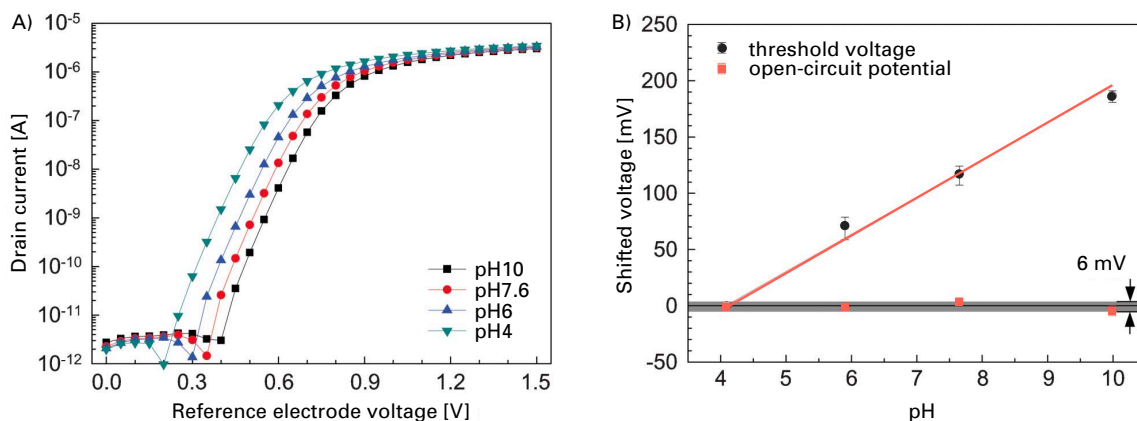


**Figure 1.9.:** pH measurements with a top-down fabricated SiNW FET using different pH solutions [4]. pH sensitivity here is 35 mV/pH. a) Transfer curves and their shifts in x-direction. b) Shifted voltage due to pH steps.

As most biomolecules display charges at their outer surface (depending on the pH of the solution), ISFETs are equally sensitive to biomolecules such as proteins or DNA. Thus, the curve shifts parallel to the x-axis in case the charge situation changes are analyzed the same way as for pH measurements. The direction always depends on the charge sign.

Few publications are available on planar FETs (two-dimensional transistors) as they lack low detection limits. Bavli *et al.* showed a planar resistor (molecularly controlled semiconductor resistor MOCSEER), run in liquid environment, for the detection of different analytes on a lipid bilayer functionalized surface with a detection limit also in the  $\mu\text{g}/\text{ml}$  range [86]. Hammock *et al.* introduced a planar organic FET for thrombin sensing using an aptamer. The signal was enhanced by adsorption of randomly distributed gold nanoparticles. They achieved a detection limit of 100 pM.

## SiNW FETs

SiNW based FETs for biosensing belong to the group of ion-sensitive FETs (ISFET) operated in liquid conditions. Nanomaterials were implemented as they are suitable for detection of biochemical recognition due to their excellent sensitivity at the (sub-)nano scale. Nanowires offer high surface-to-volume ratios for good sensitivity and small cross-sectional conduction pathways [108]. Therefore, they can overcome the detection limits of planar ISFETs. Backgated nanowire based FETs have a transconductance of 4-10 times higher than planar standard ISFETs of same sizes due to their high surface-to-volume ratio and the efficient penetration of the gate field [109]. For biosensing applications as ISFETs, the liquid also acts as a gate electrode and variations in the surface potential are converted to a conductance change in the channel. Different from planar ISFETs, the NWs themselves are conduction channels which are fully affected by surface potential. Biological recognition events alter the surface potential of the nanomaterials even at low analyte concentrations. Charged biomolecules can locally act as liquid gate leading to resistivity changes. The resistivity is very sensitive towards the biorecognition event. Due to signal amplification by the FET the signal can be detected by significant jumps in the voltage at a fixed source drain current. Commonly, single-crystalline nanowires are with p- or n-type doping to create charge carriers that are attracted or repelled by the attaching charged biomolecule.

The proposed sensor is not using doped NWs as mostly employed [7, 110] but tuning of the Schottky barrier width and height due to local changes of the charge environment caused by charged biomolecules represents the sensing mechanism [108, 111, 112]. The undoped single-crystalline Si nanowire is free of impurities which is believed to increase the performance compared to doped SiNWs. Schottky barriers are formed by interdiffusion of nickel from the nickel contacts into the nanowire at elevated temperatures. Ni and Si form an alloy with almost similar crystal lattice parameters as Si has. The interface between NiSi<sub>2</sub> and Si is sharp and regarded as a true Schottky barrier [113] avoiding contact resistances in contrast to other devices as presented by Shin *et al.* [114]. The pristine Si channel is centered between the two metallic NiSi<sub>2</sub> leads. The Si channel length depends on the applied annealing time which allows for Ni diffusion and alloy formation. By changes in the gate voltage the barrier width is altered. The existence of a Schottky barrier using the here presented technique is proven in the publication of Martin *et al.* by applying scanning gate microscopy [115]. Modelling of the Schottky barrier in 1D shows the improvements compared to 2D (planar) Schottky barrier devices. The confinement due to the nanometer diameter leads to a shortage of the Schottky barrier width and lowers the Schottky barrier which facilitates tunneling and enhances the current densities [108, 112]. In ambient atmosphere, SiNWs are oxidized and thus coated by a native oxide shell which is amorphous. Typical nanoscale ISFET devices with oxide shell show a sensitivity in the range from 20 mV/pH (pH near 2) to more than 45 mV/pH (pH > 5) [107], a so-called sub-Nernstian behaviour. The pH sensitivity can be increased by deposition of thin Al<sub>2</sub>O<sub>3</sub> layers [107]. To summarize, biorecognition events at the NW surface of these Schottky barrier powered FETs act as an applied gate voltage and are expected to alter the barrier width and height [108] which leads to a measurable signal.

### 1.4.2. Fabrication methods

In principal, there are two main methods to fabricate single-crystalline SiNWs. Both methods are shortly described in the following paragraphs. For this thesis mainly bottom-up grown NWs using CVD furnaces (chemical vapour deposition) were integrated into device structures. In cooperation with the BioFET group at POSTECH, also devices with top-down NW arrays based on lithographic fabrication were studied [4, 116]. Furthermore, nanocrystalline nanowires consisting of other materials like copper or noble metals can be produced out of salt solutions with dielectrophoresis which is investigated at our chair [117–119]. Using bottom-up technologies for the NW fabrication allows for cheaper production of the nanometer features. Further processing steps in the micrometer range were carried out by standard lithography techniques.

#### Device with bottom-up grown silicon nanowires

**Bottom-up nanowire growth** Single-crystalline Si nanowires are grown with vapour-liquid-solid growth method (VLS) which was first described by Wagner and Ellis [120]. Growth is carried out in a CVD furnace (CVD – chemical vapour deposition). Thin gold films (*e.g.* 0.3 nm [111]) are sputtered onto Si wafers and heated to 450°C until coalescence results in nanoparticle (NP) formation. Argon plasma improves significantly the homogeneity of the Au cluster size [111]. Another method is to use presynthesized gold colloids (AuNPs) which are dispersed on a wafer substrate [9, 112]. In both cases the AuNPs act as catalyst particles for the nanowire growth. Gold forms a liquid alloy with Si from the gas phase which comes from a monosilane flow ( $\text{SiH}_4$ ) at 450°C and defined pressure. Once the droplet is supersaturated, Si starts to precipitate at the droplet-substrate interface. Single-crystalline nanowires grow in tip growth mode in the vertical direction. Varying pressure and temperature influences the diameter and the growth morphology – straight, kinked or spaghetti-like [109]. The NW diameters correlate with the NP diameter but are slightly bigger [112, 121]. The resulting NW forest on the growth substrate, see Figure 1.10A), is then further processed for device integration by removing the NWs from the substrate.

Different generations of devices were fabricated by S. Pregl (in preparation: Ph.D. thesis on FET optimization). Undoped SiNWs were grown in the previously described bottom-up method VLS in a CVD furnace using gold nanoparticles with a diameter of 19 nm  $\pm$  0.5 nm (from BBI). Monosilane gas  $\text{SiH}_4$  was used a precursor and  $\text{H}_2$  as the carrier gas (450°C, 65 mbar). This resulted in NWs with a mean diameter of 22 nm  $\pm$  0.5 nm for our sensor and a ratio of 114% for  $\frac{d_{NW}}{d_{AuNP}}$  [112]. Lengths of 10  $\mu\text{m}$  up to 40  $\mu\text{m}$  are typical [122]. They were transferred to thermally oxidized Si wafers (100 nm oxide) using contact printing (CP) for large-scale parallel alignment, see Figure 1.10B). Before further processing, the AuNPs were etched off to avoid gold contaminations and the oxide shell was removed by etching in buffered HF to assure direct contact of the nickel material with bare silicon. A SiNW with thermally grown oxide of 5 nm is presented in Figure 1.11. The nanowire with an original diameter of roughly 22 nm grows in radial direction by further thermal oxidation from 2 nm to around 5 nm oxide thickness.

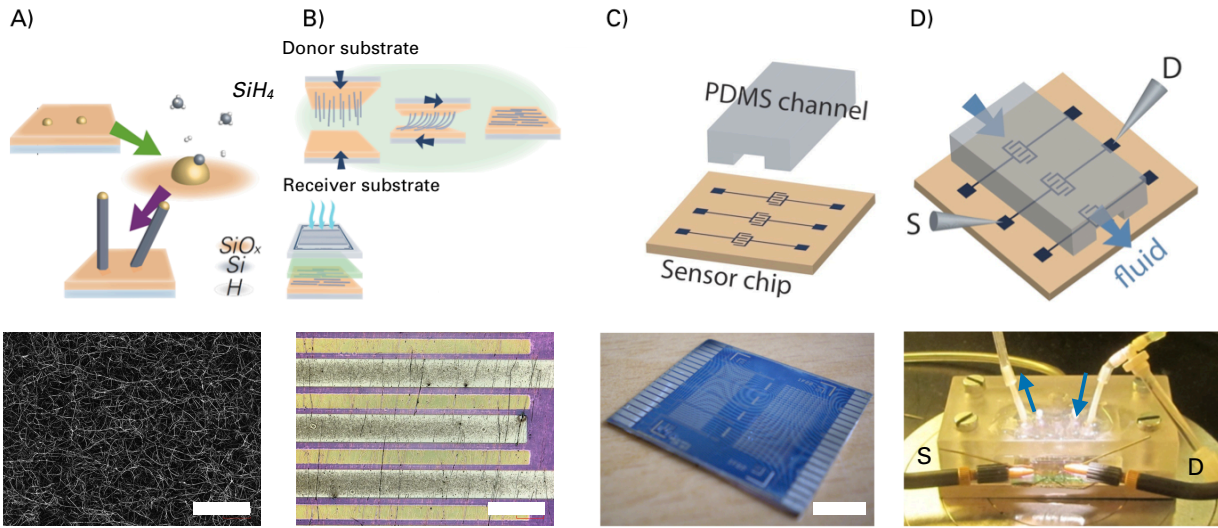


**Figure 1.10.:** Fabrication procedure of SiNW FETs with bottom-up grown nanowires. A) Scheme of NW growth from gold catalyst particles in silane flow in tip-growth method and optical image of the growth substrate. Scale bar is  $20\ \mu\text{m}$ . B) Scheme of contact printing procedure for transfer from donor to receiver substrates results in parallelly aligned nanowires. Postdefinition of contact structures using UV lithography. Optical image of the interdigitated finger structure after this process. Scale bar is  $20\ \mu\text{m}$ . C) After processing, the sensor chip is ready for integration in the experimental setup, *e.g.* by putting a PDMS channel on top of the chip. Scale bar is  $5\ \text{mm}$ . Picture of the chip: courtesy of F. Zörgiebel. D) Chip with PDMS channel and the tips of a probe station to contact source and drain. This simple setup has one in- and one outlet. Sketches in upper row from S. Pregl.

**Nanowire integration into devices** SiNW FET devices with a single NW can be achieved by sonicating the grown NWs in organic solvent and spraying on a chip wafer [111, 123]. By chance a NW is connecting two preprocessed contacts or post defining of contacts using e-beam lithography enables the fabrication of electrically connected SiNWs. Parallel arrays of SiNWs are created by contact printing (transfer printing) from the growth substrate, *i.e.* donor substrate, to a virgin wafer, *i.e.* receiver substrate [122, 124–126], as illustrated in Figure 1.10B). Alignment techniques such as Langmuir-Blodgett were also applied to NW solutions in organic solvent [127, 128] or by directed spray flow [123]. By using parallel arrays, the bottom up grown NWs can be easily integrated into the production route of the Si based chip in a routine step allowing for series production [112, 126]. In parallel arrays, single defect wires do not influence the overall performance due to averaging. These arrays result in high currents with on/off current ratios of up to  $10^6$ . In addition, higher currents facilitate the integration in commercially available and cheap devices due to easier packaging of integrated circuits [112].

The device structure was created using photolithography on the parallel NW substrates [112], see Figure 1.10B). Via evaporation, nickel contacts were deposited onto the chip. Interdigitated finger structures were patterned onto the chip as it is presented in Figure 1.10B), C). Each chip was thus composed of 21 structures. Before initiating the silicidation process, the photoresist was removed. Heating the contacted NWs up to  $500^\circ\text{C}$  leads to Ni diffusion into the NW bulk. Different NiSi phase

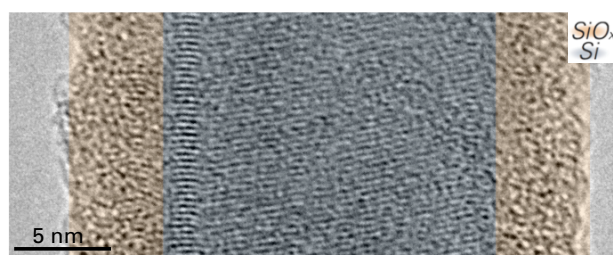


**Figure 1.11.:** TEM image of SiNW with thermal oxide, annealed at 875°C for 4 min. Courtesy of E. Baek.

may form, but the interface between NiSi and pristine Si was found to compose of NiSi<sub>2</sub> [113]. Due to variations in nanowire diameters and their crystal orientations, the silicidation length is different for each nanowire. Thus, the electrode spacing also needs to be sufficiently large to create a high yield of silicidized NWs without completely metallizing. Fully metallized nanowires however can be burnt via Joule heating when applying a source drain voltage at zero gate voltage [112]. To give an example, for an interelectrode spacing of 2.5  $\mu\text{m}$  the developed procedure leads to pristine channel length of 0.41  $\mu\text{m} \pm 0.2 \mu\text{m}$ .

The nanowires were oxidized at 875°C resulting in a homogeneous dense oxide layer and a reproducible oxide thickness of around 5 nm (see Figure 1.11) for an annealing time of 4 min. Further processing is required for operation in liquids to prevent any material from degradation and assure sample delivery via fluidic channels as exemplarily demonstrated in Figure 1.10 (details see next paragraph and in section 5.1).

**Fluidic setup** Aiming for health diagnostics and portable devices, housing concepts and microfluidics are crucial. Microfluidics also reduce the required amount of analyzing substance and its evaporation is avoided which would lead to signal modification by changing the concentration with time. During surface functionalization, channels could be helpful to specifically functionalize only the exposed chip regions of interest for higher sensitivity [129]. Parallel channels allow for multiplexed detection of different analytes and on-chip control measurements. Commonly, PDMS molds are mechanically pressed onto the chip and microfluidic tubes are connected to this. Small channel structures are created lithographically using chemically stable photoresists like SU-8 as channel material. Fraunhofer Society presented a platform including analyte and buffer compartments for mixing and multiparameter analysis as well as integrated pumps [130]. This credit card sized housing can include various types of sensors (electrical, optical) allowing for portability and versatility in application. The FET sensor development also includes housing and packaging development as ongoing research (in cooperation with IAVT, TU Dresden). As a first setup, a single channel in PDMS mold was fabricated and integrated in the chip measurement setup, see Figure 1.10D) and chapter 5.1.1. These devices were used for aptamer based sensing in this work.

**Passivation strategies** For these biosensing applications, passivation steps are necessary and were developed by S. Pregl and F. Zörgiebel and will be presented more in detail in their Ph.D. theses. The goal of chip passivation is to protect any material from degradation due to the used liquids during the functionalization and detection procedure. Degradation especially of metallic materials would cause leakage. Different methods such as a polymer layer which leaves the sensitive region free or oxide layers were investigated for the purpose of biosensing. Deposition of a thin  $\text{Al}_2\text{O}_3$  layer of 15 nm using atomic layer deposition (ALD) shows the best results. Here, the sensitive device region is fully covered with this thin layer. By this, any liquid can intrude between the chip and the passivation layer. This layer does not decrease the performance of the device, which was tested in dry and liquid conditions. On the contrary,  $\text{Al}_2\text{O}_3$  offers more OH groups after hydroxylation than  $\text{SiO}_2$ . This results in a higher sensitivity for pH sensing and approaches the Nernst limit [105, 107]. As the performance as an ISFET is not reduced and  $\text{Al}_2\text{O}_3$  can be functionalized with organosilanes as it is the case for  $\text{SiO}_2$  [107], the introduction of the layer was the method of choice to assure biosensing without the risk of degradation.

#### Device with top-down fabricated silicon nanowires

In 2004, a method to fabricate SiNWs with a combination of lithography techniques defining nanowires from thin single crystalline Si layers was presented [131]. In order to produce top-down Si NWs, these layers on wafers are selectively etched after electron beam (e-beam) lithography (Figure 1.12, steps 1 and 2). E-beam lithography is required to achieve diameters below 100 nm. Here, the fabrication of Rim *et al.* is presented more in detail as these n-type FET sensors fabricated in POSTECH were used, too [4, 116].

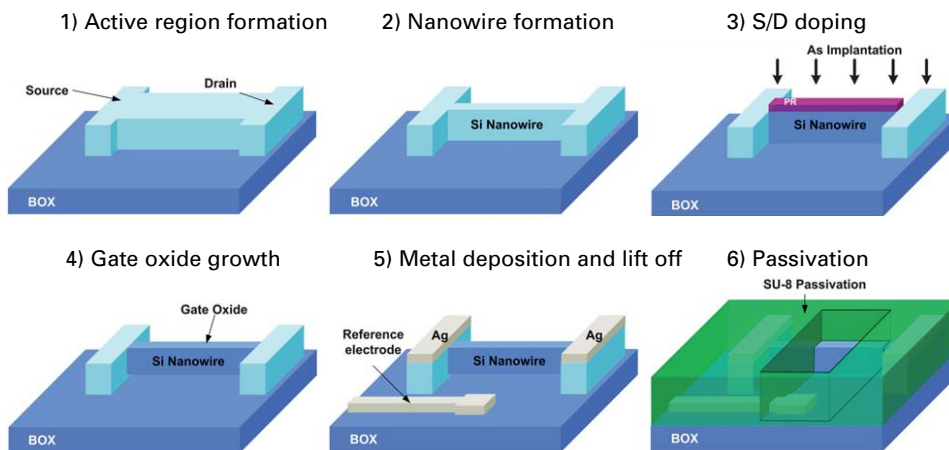


**Figure 1.12.:** Device fabrication process for top-down fabricated SiNW FET from POSTECH, image taken from [116] and modified.



After nanowire array fabrication, source and drain are doped by ion implantation to form ohmic contacts (step 3). Gate oxide is grown to create the gate dielectric (step 4). Metal contacts are defined (step 5) and finally everything except the wire regions is passivated for sensor use in liquids, *e.g.* with photoresists like SU-8 (step 6). The advantages of top-down devices compared to those implementing bottom-up grown NWs are the precise definition of NW arrays on certain areas and the predetermined number of NWs on one device which increases the reproducibility. Moreover, it is possible to create different structures than just straight NWs like honeycomb patterns which were proposed to show higher reliability and sensitivity [132]. However, the processing (e-beam lithography) and other steps are more expensive and complicated than the combined VLS and CP procedures which reduces time and the use of costly equipment. The NWs are also not as symmetrical in crosssection due to their trapezoidal shape and show rather thick oxide shells at least 5 nm with varying thickness [4]. These devices were used for antibody based sensing in this work.

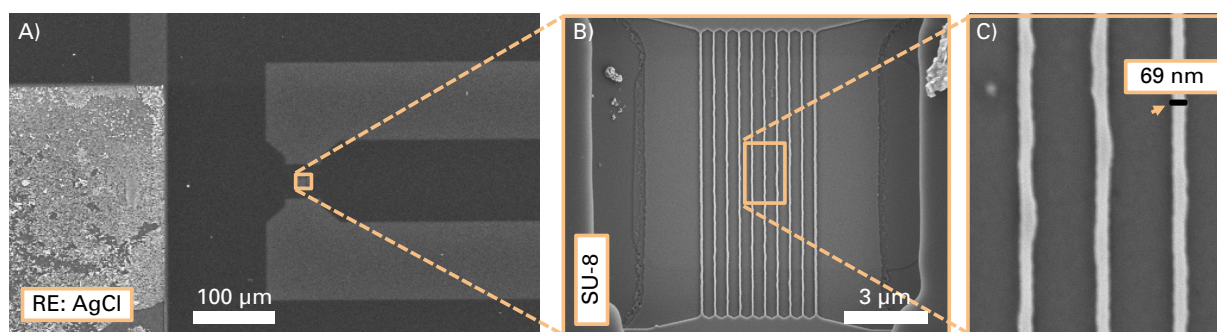


**Figure 1.13.:** SEM image of a top-down fabricated NW chip. a) On-chip reference electrode close to nanowire array. b) Open NW array with 10 parallel wires surrounded by polymer layer cover (SU-8). c) The wires have a mean diameter of 50 nm with a 10 nm oxide shell. This results in an average diameter of 70 nm.

### 1.4.3. Influences of organic solvents and buffer solutions

A crucial parameter for biosensing with an FET is the ionic strength of the measurement solution. It defines the Debye screening length at the sensor surface (here: the NW), meaning that only charges within this distance are screened and alter the device characteristics. Thus, the molarity of the used buffer solution needs to be kept at a low level as this results in a higher Debye screening length  $\lambda_D$ . This length can be calculated using the formula:

$$\lambda_D = \sqrt{\frac{\epsilon_0 \epsilon_r k T}{2 N_A e^2 I}} \quad (1.2)$$

For different buffer strengths of the widely used PBS buffer with physiological pH, the Debye length is exemplarily shown in Figure 1.14. With the standard 1x concentration of PBS (10 mM), the maximally sensed recognition event could be at a distance of approximately 1.5-3 nm [12, 14, 133]. For typical sample solutions like blood, serum or urine, the Debye layer is only 0.7-2.2 nm thick [12].

Due to this, many experiments are run in low ionic strength solutions of 1 mM or less. Very low concentrations could be problematic for biosensing. Certain ionic concentrations are required for the proper three-dimensional structure formation of biological molecules (see 1.2) and the biorecognition itself.

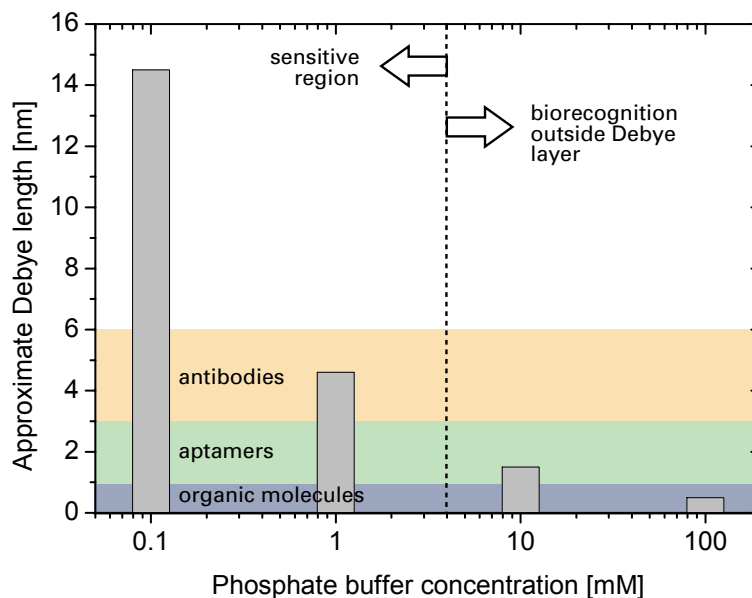


**Figure 1.14.:** Illustration of the Debye length for different phosphate buffer concentrations ( $x$  M) and  $2x$  M NaCl. The values are extracted from Park *et al.* [133]. The blue stripe indicates the thickness of a layer of organic molecules (example of organosilane layer), the green stripe represents the extents of an additional aptamer layer, the green and orange stripes together illustrate the thickness of an additional antibody layer on top of the organic molecules. The upper limit of the sensitive region for aptamers as recognition elements can be found in between 1 and 10 mM, as indicated by the vertical dashed line. For antibodies (orange), concentrations of less than 1 mM would be required because of their size [133].

Buffers and reagents used during biochemical functionalization and when the device is run in liquid media usually cause the metallic materials like source and drain contacts to degrade or react with ions which leads to a baseline drift and performance reduction. Thus, reliable passivation and housing are key steps for stable biosensor measurements. The measurements presented in this work were carried out using passivation of the device (see section 1.4.2). Chemical functionalization is also affected by aqueous liquids which may lead to detaching of organic surface layers see section 1.3. Thus it is desirable to achieve homogeneous (mono)layers and covalent bonding which is stable in the applied liquid solutions.

To summarize, Lieber *et al.* firstly published NW based FETs for biosensors [7, 121] and are to date still using bottom-up grown nanowires [126]. Several groups have started biosensor research using NWs since then, but the majority researches on top-down devices since published [131] (see overview in Table 1.1, partially adapted from Curreli *et al.* and Lahouq and extended [36, 37]). The achieved sensitivities are comparable for both techniques. This work mainly focuses on bottom-up chips, as we are interested to replace as many steps as possible by bottom-up procedures and self-assembly, but it also shows the application of highly-developed top-down chips in cooperation with POSTECH [4].

## 1.5. Conclusion

In this chapter, the different building blocks for biosensing with a focus on aptamer based sensing using nanowire ISFETs were presented. To conclude, the promising properties of aptamers especially with respect to the specific requirements in ISFET based biosensing lead to a further interest to implement these aptamers in our Schottky barrier powered SiNW FET. Several applications and receptor-analyte systems were summarized in this chapter. The main focus in this work is on the detection of the protein thrombin as a model system for aptamer based sensor development using DNA aptamers. The thrombin binding aptamer 1 (TBA1) is very stable. In addition, a second aptamer is available which helps to characterize the samples in sandwich assays. The interest in thrombin detection and the aptamer design are explained in section 3.1.

In addition, small molecule detection will be shown exemplarily using antibodies against an antibiotic, namely amoxicillin (AMX), which belongs to the group of penicillins. This aims at detection of AMX residues in water samples, see section 3.2.



## 2. Materials and Methods

This chapter presents the used materials for providing functionalized surfaces with reactive terminal groups for further attachment. This is followed by presentation and discussion of the relevance of two different applications, *i.e.* the target molecules which will be detected. At the end of the first part, a list of all materials can be found. The second part deals with the details of characterization techniques for biochemical functionalization and receptor-analyte interactions.

### 2.1. Surface modification techniques

#### 2.1.1. Surfaces

With the goal to functionalize silicon nanowires integrated in field-effect-transistors (FET) on silicon wafer chips, the possible surfaces are presented. Silicon nanowires are curved objects with different planes exposed. In order to investigate the functionalization steps and test different strategies, the use of planar substrates facilitates characterization. Firstly, Si wafers as substrates can be used and are especially suited for techniques like ellipsometry or atomic force microscopy (AFM) due to the flat surface. In order to detect fluorescence, glass slides are the substrates of choice. Si nanowires and wafers are oxidized in ambient conditions with a thin oxide shell of around 2 nm. Thus, Si and O are present at the surface and the structure is amorph which is comparable to glass. Etching the oxide however cleaves the oxide and leads to hydrogen-terminated Si which is well suited for SAM formation. Both surface possibilities are discussed in the following.

#### Hydrogen-terminated silicon surface

After removing the oxide in strong acid (HF or  $\text{NH}_4\text{F}$ ), the resulting hydrogen-terminated Si is able to react with  $\omega$ -alkenes. Their C=C double bond at one chain end is catalyzed upon irradiation with UV light or at elevated temperatures and covalently attaches to Si-H forming stable Si-C bonds. The long alkyl chains tend to form well-ordered self-assembled monolayers (SAM) see section 1.3.2. By using carboxy terminated molecules, receptors with functional primary amines can be immobilized on the modified nanowire surface. In order to evaluate this way of surface treatment, its sensitivity was compared to the sensitivity of SiNW FETs with oxide shell. Bunimovich *et al.* demonstrated that DNA probes which were surface bound via electrostatic interaction to an amino terminated oxide-free Si nanowire show a higher sensitivity for hybridization with the complementary strand than on an equally amino functionalized oxidized nanowire [134]. This advantage of the hydrogen terminated surface has to be counterbalanced with the etching step which is aggressive towards metallic materials

on the chips. This is particularly critical for our Schottky barrier FET devices. The sensitive region is located at the interface so the metallic part cannot be covered during etching and might be etched away too quickly as NWs are very thin. It is however an interesting option for doped NWs to achieve high performances. Physical properties of SiNWs can be controllably altered by defining their surface bonds due to chemical functionalization of oxide-free NWs [135]. In addition, it would require to open windows after passivation to be able to access bare wires.

### Silicon dioxide surface

Silicon is naturally oxidized in ambient atmosphere. The native shell is usually around 2 nm thick (measured with transmission electron microscopy) and can be grown thermally to thicker layers (thermal oxide). The structure of silicon dioxide however is amorphous so the crystal plane of the nanowire does not play a role for functionalization layers. As the surface groups are Si-O, different attachment strategies are possible. The bare oxide surface is not very reactive. Thus, non-covalent attachment routes are one option, see 1.3.1. For covalent ways, an activation of the hydroxy groups is necessary. This is achieved via plasma treatment using oxygen plasma or solvent-based methods like the use of NaOH as presented by Janissen *et al.* [103]. The created hydroxy groups (Si-OH) are reactive for attachment with several molecules as described in paragraph 1.3.2. Silane molecules that bind to SiO<sub>2</sub> also attach to other oxides like ZnO or Al<sub>2</sub>O<sub>3</sub> [105, 136]. Thus, a later passivation of the nanowire FET with such an oxide layer does necessarily require fundamental changes in the functionalization strategy. The density of silanol groups on a fully hydroxylated surface is 5.0 groups/nm<sup>2</sup>. The estimated amine density with APTES is then around 2-4 molecules/nm<sup>2</sup> [137, 138]. For investigations with transmission optical microscopy, the functionalization of glass slides instead of opaque wafers significantly simplifies characterization of the modification strategies.

To conclude, silicon dioxide was chosen for further functionalization purposes after careful consideration of the different characteristics. Although on hydrogen terminated Si more uniform layers (*i.e.* SAMs) can form which enhances reproducibility and stability, the easier handling of naturally oxidized samples, comparison with glass slides, the more universal approach in terms of passivation with other oxides for sensor applications in liquids and the short linker length of many silanes led to this choice. In addition, etching of metallic NiSi<sub>2</sub> would be hard to control which is critical with respect to the most sensitive region of the FET, the Schottky barrier. The protocols are then transferred from planar substrates to the silicon nanowires on the chip.

### Cleaning

The cleaning procedures of wafer pieces and glass slides are described in detail in the appendix A.1. Wafers were ordered from clean room facilities and exhibit a very flat surface. They are cleaned using organic solvents and temperature treatment or ultrasound to create bubbles at the surface that carry away dirt particles and contaminants. This is finally followed by plasma cleaning for removal of organic contaminants and hydroxyl group activation. Cleaning of wafers was always carried out directly before further modification. Purchased glass slides exhibit more contaminants on their surfaces. The same

treatment as for wafers results in blurry backgrounds as it was observed for fluorescence tests to confirm DNA attachment. Thus, these substrates require a cleaning procedure involving organic solvents as well as immersion in acids and bases for proper cleaning (see appendix A.1). The glass slides were used within two weeks after cleaning.

## 2.1.2. Chemical surface functionalization

### Carboxy-terminated surface

The amino terminated silane 3-aminopropyltriethoxysilane (APTES) is the most popular silane in research. Mostly, liquid phase attachment in ethanol at a concentration of 1-2 % silane is used with incubation times around 0.5-1 h and a postbake at 110-120°C for 10-20 min [15, 138–140]. These protocols result in amino surfaces with monolayer thicknesses although the real silane layer probably shows a parallel occurrence of chemi- and physisorption, molecular stacking and polymerization, see Figure 1.7 [102]. Detailed protocols for all steps can be found in the appendix A.1. Silanization with aminosilanes was also carried out via the gas phase in a Schlenk tube setup as presented in section 2.1.2.

To link the amino-receptors to this surface, intermediate steps of crosslinking and activation are necessary. Carboxy groups are created by adding a solution of the molecule succinic anhydride as a heterobifunctional crosslinker (see Figure 2.1). The anhydride is very reactive towards nucleophiles like amines. During the reaction with the surface-amine, one carbonyl group of the two gets attacked and the anhydride ring structure opens up. This carbonyl binds covalently to the amine. The other one is free to create a terminal carboxylic acid [98].

Carboxy groups only link to the amino-terminated receptor after activation with so-called zero-length crosslinkers. They form an intermediate reactive product but are not included in the later binding itself. The method of choice here is to use carbodiimide EDC (1-ethyl-3-(3-dimethylamino-propyl)carbodiimide) and the ester NHS (N-hydroxysuccinimide). At first, EDC activates the carboxy groups by binding to them (Figure 2.2). Therefore, EDC should be added initially in the experimental procedure. To be more precise, EDC hydrochloride powder is dissolved in water at a high concentration and then added to the reaction solution at the final concentration. This is followed by adding NHS for attachment. NHS replaces EDC and creates a reactive ester. This ester splits upon primary amine binding when the amino-terminated receptor (amino-receptor) is added. Hermanson also recommends the use of sulfo-NHS as it is better soluble in water than NHS [98]. Presolving NHS in water as a stock solution, assure dissolving by intense vortexing and adding the concentrated solution to the reaction worked here, too. The reaction is influenced by the pH and is faster at lower pH values [98]. The additional substances also bare the risk of contamination of the surface due to byproducts. The advantage of this method is that the specificity of the receptor attachment and the success can be evaluated by leaving out the activation step. In this work, also another variation of the silane was studied which possesses three methoxy instead of ethoxy groups (APTMS).

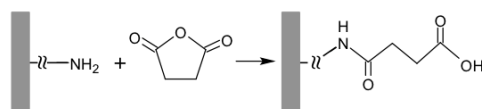


**Figure 2.1.:** Schematic drawing of reaction scheme of ring opening reaction of heterobifunctional crosslinker succinic anhydride upon attachment to an amino-terminated  $\text{SiO}_2$  surface (grey bar).

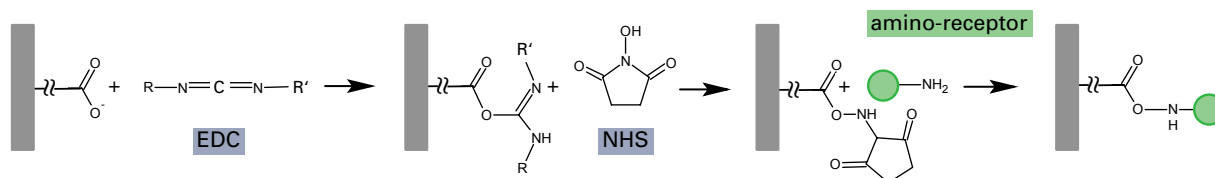


**Figure 2.2.:** Schematic drawing of reaction scheme using zero-length crosslinkers EDC and NHS for carboxy group activation to form amide bonds with primary amines of receptors to a carboxy-terminated  $\text{SiO}_2$  surface (grey bar).

### Epoxy-terminated surface

The epoxy silane glycidoxypropyltrimethoxysilane (GOPMS) is the second option for surface functionalization with silanes. Its advantages compared to APTES are that it allows a one-step attachment of the amino-receptor, as epoxy and primary amines couple directly and form stable aminoalcohols (see section 1.2). Additionally, Taylor *et al.* showed that GOPMS surfaces result in low background signals for unspecific DNA adsorption. Similar to the ethoxy groups, the methoxy groups hydrolyze and the resulting silanols attach to the activated surface. The terminal epoxy group forms a covalent bond directly with the receptor amine at slightly elevated pH values of at least 8.5-9.0 [98, 110] (taking physiological pH 7.4 as a standard reference for the biosensing experiments). The ring opens and the terminal C atom covalently binds to N to form a stable aminoalcohol, see Figure 2.3. The epoxy silane is more sensitive to atmosphere (hydrolysis [101]) and longer incubation times are required than for APTES. Firstly, adsorption from the liquid phase with protocols adapted from Hermanson and Gopinath *et al.* was tested [98, 141]. Solution based protocols also include solvents like toluene instead of ethanol which makes the procedure more complicated especially with respect to chips and the aim to reduce possible harming of the devices during surface modification. So the focus was here more on gas phase attachment. As equipment like a solid glove box and more complicated setups as presented by the group of Ingebrandt [142] were not available or possible to realize, other protocols were investigated. The gas phase attachment in an oven over night after Tarasov [105] leads to reproducible results and was thus the method of choice. The protocol can be found in the appendix A.1. Ek *et al.* also found out that gas phase attachment results in layers with higher density than solution based methods [137].

### Setup for gas phase silanization in Schlenk tube

Silanes as chemical functionalization layer were described in section 1.3. Silane layers are created either by diluting the silane in a solvent and subsequent sample immersion or via evaporation at low



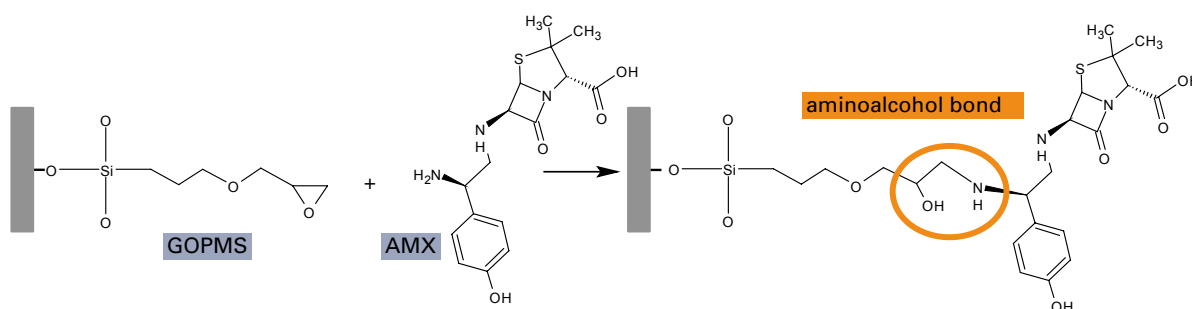


**Figure 2.3.:** Schematic drawing of reaction scheme of terminal epoxy groups on SiO<sub>2</sub> surface with amino-terminated molecule (here amoxicillin). Together, they form an aminoalcohol bond which is stable.

pressure and/or higher temperature. The latter requires a chamber setup. A simple way is to place the sample in the vicinity of a droplet of the silane, altogether in a chamber (*i.e.* oven, desiccator) and heat or apply a vacuum. This lowers the vapour pressure of the liquid and it evaporates, also onto the sample. A more elegant way is to use sealed chambers or tube systems that allow to remove air and water from the reaction or control their influence as the silanes are degrading in the presence of water. This can be done by vacuum pumping and inert gas purging. Reducing the chamber size decreases the required amount of liquid and the system is more controllable. Such a goal was achieved by setting up a common Schlenk tube system with a valve either allowing N<sub>2</sub> flow or pumping, see Figure 2.4. The valve allows continuous pumping and purging for immediate switching. It is connected to the reaction glass tube via a polymer tube. Before functionalization, the system is pumped and flushed three times to remove water. The sample and silane are installed in the glass tube (see inset in Figure 2.4) while purging with N<sub>2</sub> to assure little water content. The droplet is firstly deposited onto the flask bottom using a pipette. Then the sample is placed onto the holder with the active side facing up. The holder which is attached to the lid is then carefully placed within the tube. The samples are thus approximately 2 cm above the droplet. By turning the valve from inert gas flow to pumping, the lid is tightly sealed. As the volume of the tube is small (around 100 ml) the vacuum which is controlled by a pressure meter is quickly created. For APTES attachment, the protocol from Choi *et al.* was adapted and downsized [143]. For the flask volume, 50  $\mu$ l of pure silane are pumped for 1-2 min and then left without pumping for 0.5-1 min. After purging, the sample is ready for postbaking with the same parameters as for liquid phase attachment (see appendix A.1) and without further rinsing steps. This setup was only used for wafer pieces as the opening radius is too small for conventional glass slides of around 2 cm side length.

This technique did not work for epoxy silane attachment, as the applied pressure was not enough to evaporate the epoxy silane (GOPMS) to such an extent that GOPMS layers were formed on the samples. Further heating would have been necessary. Thus, a different protocol was used for GOPMS using overnight heating in an oven adapted from Tarasov [105].

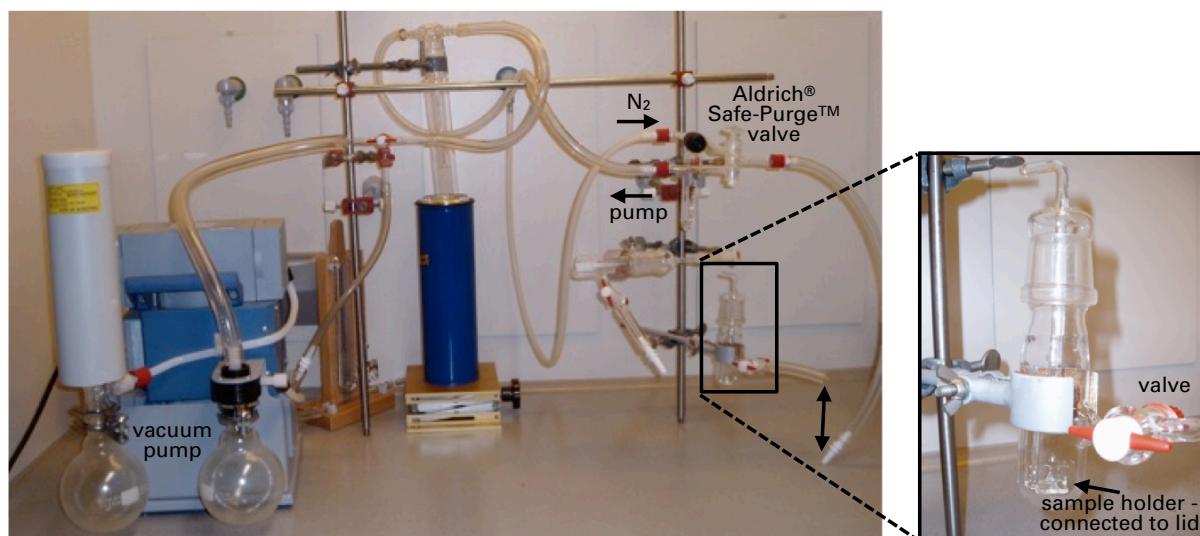


**Figure 2.4.:** Schlenk tube setup for APTES functionalization via the gas phase.  $N_2$  is purged to vent the functionalization chamber and assure inert gas flow during sample and silane placement (inset on the right). By turning the Safe-Purge valve, vacuum is pumped.

### 2.1.3. Patterning

In the following, techniques to apply chemical or biological surface patterns onto planar surface are described. Patterns offer several advantages – the presence of functionalized and reference surfaces for on-chip modification control, the easy recognition of functionalized areas by microscopy techniques and the control of blocking strategies for an improved signal-to-noise ratio.

#### Soft lithography

In the 1990s, soft lithography was invented mainly by Whitesides and co-workers [144, 145]. This is an approach to pattern surfaces on the micrometer scale with the help of a soft elastomer stamp made of PDMS. Since then, organic molecules, molecules for monolayer formation, proteins, cells, micro- and nanoparticles and many more have been transferred from solution to a substrate [146]. The basic principle is illustrated in Figure 2.5. After fabrication of the PDMS mold from a master (usually a structured Si wafer showing all kinds of structures like stripes, circles etc.), the ink containing the molecule or particle covers the whole stamp and is left for incubation. The liquid is then blown off completely in  $N_2$  flow so that only a thin film remains. Now the stamp is pressed onto the receiver substrate, leaving time for the molecules to arrange and attach. After removal, the new surface exhibits a regular pattern. This technique has been applied to pattern silicon dioxide surface with organic molecules in the past by several groups [147–149]. Silanes were of special interest for this work. The motivation to introduce patterning at the first step of functionalization bears one main advantage: each functionalization step can be monitored and analyzed for its specificity towards the modified surface in comparison to the control surface. Having both areas on one sample allows for direct comparison and possible mistakes during the experiment can be ruled out. Moreover, these

structures help to identify modified areas more easily when investigated with the microscope (like fluorescence or AFM) and increase the signal compared to the background by direct and on-chip comparison, see chapter 4.

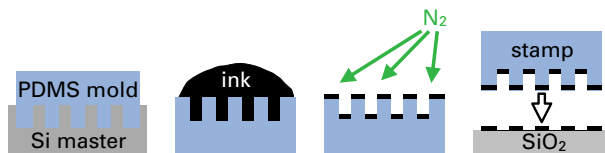


**Figure 2.5.:** Schematic drawing of preparation of a PDMS mold on a Si wafer master structure. Release of the PDMS stamp and application of an ink is followed by ink removal using nitrogen. The stamp can be used for molecule printing onto substrates like glass slides or wafers, as a thin molecular film remains on the stamp.

PDMS stamps are prepared according to standard protocols at a polymer ratio of 10:1 and molded with a Si wafer master structure. The master is created using laser lithography and wet etching. After mixing the two components, the mixture is degassed to avoid any bubble, poured over the master and heated up on a hot plate ( $110^\circ$ ) for 5 minutes. Alternatively, heating in an oven (same temperature) for 2 h also results in solidified elastomer stamps. After release from the master, the stamp is glued onto a small holder which can be used for manual printing. Including rinsing steps, the stamp can be used for the same chemical several times, however it should not be too old in general. The exact protocol can be found in the appendix A.3.

As a first test, the success of the printing can be tested easily. Silanes are usually less hydrophilic than the rather freshly plasma cleaned  $\text{SiO}_2$  surface which is very hydrophilic. By cooling down the sample using a flat peltier element, water from the atmosphere condensates in between the printed substrates. To investigate the patterns more in detail, AFM studies, labeling with gold nanoparticles and fluorescence tests were carried out.

## Nanoplotting

A nanoplotter can be used to create microarrays by spotting nano- to picoliter amounts of the solution onto a surface in regular arrays. Here the nanoplotter device from GeSiM mbH was used in combination with the picoliter pipette creating droplets of  $60\text{--}70\ \mu\text{l}$ . The array parameters (size, distances) were selected depending on the contact angle of the droplet on the chosen surface (glass slides, chips etc.). It is also possible to plot different solutions on one sample. The droplets dry fast due to their small size. Spotting of aptamers is not a problem as drying does not destroy their function. By immersion in buffers the activity is regained. Heating additionally improves the structure formation (see chapter 1). Eisen and Brown summarize different problems that might occur in nanoplotting (see Figure 2.6), their possible reasons and measures to avoid them [150], like a locally high background (A) or comet-tails (B).

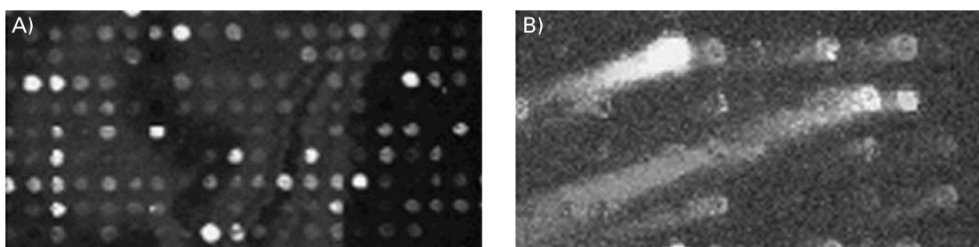


**Figure 2.6.:** Example microarray pictures with frequent errors from Eisen and Brown [150]. A) Locally high background. B) Comet-tails.

## 2.2. Selected target molecules

### 2.2.1. Protein thrombin

Thrombin is a protein which exhibits enzyme- and hormone-like properties. The molecule plays an important role in the blood coagulation cascade where it converts fibrinogen into fibrin for clotting, and it stimulates the process of platelet aggregation [151]. A role in cardiovascular diseases [152], inflammation reactions and tissue recovery make it an interesting candidate for a medical related biosensing applications. The concentration of thrombin varies a lot depending on the ongoing processes. Concentrations in the upper picomolar range indicate thrombin-related diseases with coagulation irregularities whereas normal levels can be found at  $\mu\text{M}$  down to nM range [153]. Thrombin is continuously present in the blood plasma as the precursor prothrombin which is activated when needed *e.g.* to seal wounds. Thus, label-free and real-time sensors able to measure from nanomolar down to the picomolar range are important to recognize and distinguish healthy from disease thrombin levels with a fast response time and little sample treatment.

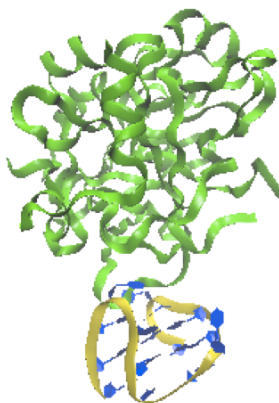


**Figure 2.7.:** Thrombin molecule representation and interaction with thrombin binding aptamer (15mer) attaching to the fibrinogen binding site (structure 1HAO in RCSB protein data bank from Padmanabhan *et al.* [154], visualized in VMD 1.9.1.

For experiments, the heterodimer human  $\alpha$ -thrombin is used. It is produced by proteolytic activation of prothrombin with the help of an enzyme called prothrombinase. This enzyme catalyzes the

proteolysis of two peptide bonds which results in the heterodimer. The heterodimer is composed of a lighter A chain and a heavier B chain (6,000 and 31,000 Da). They are linked via a disulfide bond. The size of thrombin is thus 37,000 Da. The isoelectric point is around pH 7-7.6 [155]. For detection of charged thrombin a biorecognition buffer below or above physiological pH is required. Thrombin will be positively charged at lower pH values.

Thrombin displays two electropositive binding sites [156]. The first aptamer which was developed against thrombin [23] detects the fibrinogen binding site. The interaction of both molecules is presented in Figure 2.7. Since 1997, a second aptamer that binds to a different binding site (*i.e.* heparin) is available, too [25]. By binding to these thrombin sites, both aptamers can also act as artificial inhibitors of thrombin-induced processes initiated at these exosites. This is also useful for sandwich assays where the analyte is sandwiched in between two receptors. Thus, no protein labeling is required. It is much easier to implement labeled DNA, *i.e.* labeled aptamers, into the assay. Due to the stable quadruplex conformation of the thrombin binding aptamers [25], thrombin detection is also an excellent model system used to develop aptasensors on different sensor platforms [20, 57, 157, 158]. The aptamer based sensing concept for thrombin is presented more in detail in section 3.1.2.

### 2.2.2. Antibiotic amoxicillin

Many bacteria infections can be cured using antibiotics like penicillin. Bacteria can however adapt to this medication and become resistant. Due to the massive worldwide use of antibiotics for treatment of diseases of humans but also of animals in food industry many superresistances have already been developed. The continuous use of antibiotics leads to contamination of water which affects plants, animals and especially humans. Even low amounts may cause severe effects due to chronic doses. Therefore, the destruction of antibiotics is a goal of current research [5, 6, 159, 160] and also in the Ph.D. thesis of S. Teixeira.

To determine the contamination levels in water samples is one goal. This is already possible with different techniques [6] but FET again offers a method of realtime and low-cost biosensing. Another application for antibiotic detection comes along with the destruction of the drug molecules using catalytic nanoparticles like TiO<sub>2</sub> or ZnO and the irradiation with ultra-violet light. Even though this technique can largely destroy the molecule, see UVvis curves with time-dependent decay in Figure 2.8 for amoxicillin (courtesy of S. Teixeira, 2013) for three different nanoparticles and 20 mg/L AMX in water, it is not known whether a small amount of molecules is still present or if the residues are still harmful. Thus detecting the antibiotics after nanoparticle-UVvis treatment would allow for this.

Amoxicillin belongs to the group of penicillins for antibiotic treatment and is taken as an example for this class of drug molecules. They are all relatively small molecule (see Figure 2.9) and thus not easy to be detected by FET after functionalization with an antibody in the classical setup with immobilized antibodies. Thus a competition assay for small molecule detection was adapted from Scott *et al.* for FET sensing [161]. The setup is presented more in detail in section 3.2 on attachment strategies for antibody based sensing.

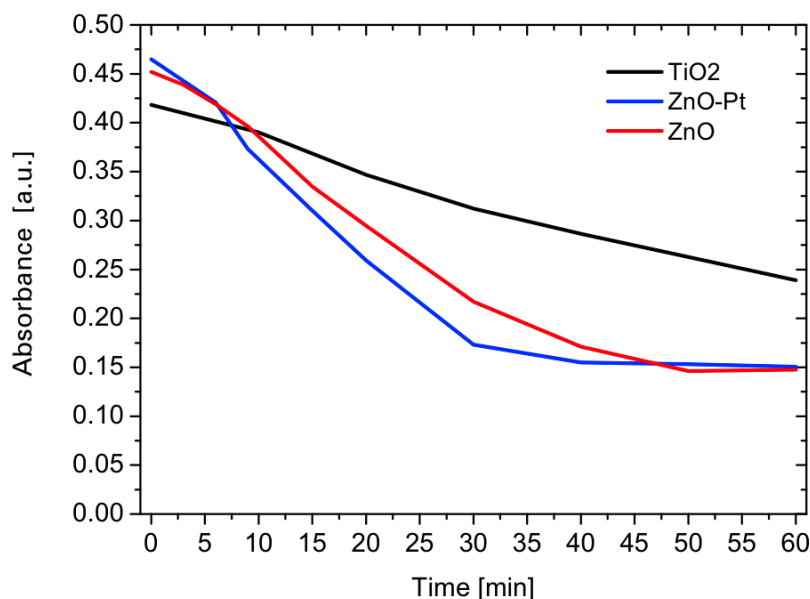


**Figure 2.8.:** Degradation of 20 mg/L AMX by 1g/L catalyst nanoparticle (TiO<sub>2</sub>, ZnO-Pt and Zn-O) under irradiation with ultra-violet light is proven by a reduction of the absorbance with increasing time of irradiation, measured with a UVvis spectrometer (courtesy of S. Teixeira).

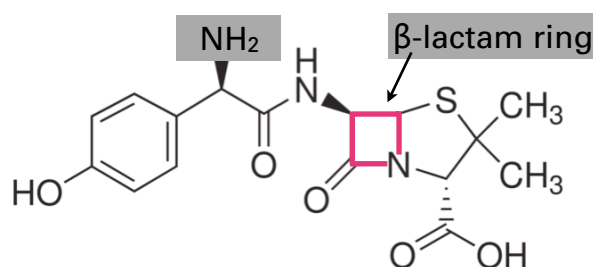


**Figure 2.9.:** Structure of molecule amoxicillin, taken from Sigma Aldrich website. The  $\beta$ -lactam ring is highlighted. The primary amine close to the benzol ring will be used for surface attachment in the inverse assay.

## 2.3. List of all materials

The used aptamers, their sequences and modifications for attachment and fluorescence labeling are listed in Table 2.1. The used aptamer strands against thrombin are called thrombin binding aptamers (TBA). As two different aptamers are available (see section 3.1, they are distinguished by naming them TBA1 and TBA2. TBA1 was used for all techniques, except for FET sensing, where TBA1-5' was attached. Fluorescence microscopy requires labeled DNA, so TBA1-FAM and TBA2-red were used for this purpose. As no label was required in the case of gelelectrophoresis, unmodified TBA2 was chosen. A ssDNA with comparable length acted as a control to TBA1 in both fluorescence and

FET sensing experiments. Further chemicals and their abbreviations as well as the companies are summarized in Table 2.2.

**Table 2.1.:** List with short name of the employed aptamer strands, their sequences and modifications (Eurofinsdna).

Name	Sequence 5' → 3'	5' modification	3' modification
TBA1	GGTTGGTGTGGTTGG	/	T <sub>6</sub> C <sub>6</sub> NH <sub>2</sub>
TBA1-green	GGTTGGTGTGGTTGG	T <sub>6</sub> C <sub>6</sub> fluorescein amidite	C <sub>6</sub> NH <sub>2</sub>
TBA1 (FET)	GGTTGGTGTGGTTGG	T <sub>6</sub> C <sub>6</sub> NH <sub>2</sub>	/
TBA2	AGTCCGTGGTAGGGCAGGTTGG GGTGAC	/	/
TBA2-red	AGTCCGTGGTAGGGCAGGTTGG GGTGAC	T <sub>6</sub> C <sub>6</sub> rhodamine red	/
SCR	CACACTCTGTCAACCTAC	C <sub>6</sub> NH <sub>2</sub>	/

**Table 2.2.:** List with all used chemicals (abbreviations, full names and company).

Short name	Full name	Company
APTES	3-aminopropyltriethoxysilane	Sigma Aldrich
GOPMS	glycidoxypropyltrimethoxysilane	Sigma Aldrich
EDC (EDC HCl)	N-(3-Dimethylaminopropyl)-N'-ethylcarbodiimide hydrochloride	Sigma Aldrich
NHS	N-hydroxysuccinimide	Sigma Aldrich
SA	succinic anhydride	Merck
AMX	amoxicillin	Sigma Aldrich
anti-AMX antibody	anti-amoxicillin antibody	Abcam
AuNP-labeled secondary antibody	anti-mouse IgG (whole molecule)-gold antibody produced in goat	Sigma Aldrich
BSA	bovine serum albumin	Merck
TGF-β1	recombinant human transforming growth factor beta 1	R&D Systems
DOPC	glycophospholipid 1,2-dioleoyl-sn-glycero-3-phosphocoline	Avanti Lipids
NBD-PE	1,2-dioleoyl-sn-glycero-3-phosphoethanolamine-N-7-nitro-2-1,3-benzoxadiazol-4-yl	Avanti Lipids
coomassie loading dye	coomassie brilliant blue	MPbio
polyacrylamide	bromphenol blue	Biolab
APS	acrylamide-bis solution (40 % w/v in dI water)	Serva
TEMED	ammoniumpersulfate	MPbio
/	tetramethylethylenediamine	Sigma Aldrich
/	gel drying frame and cellulose sheets	Carl Roth

## 2.4. Characterization techniques for biochemical functionalization

### 2.4.1. Atomic force microscopy

Atomic force microscopy (AFM) is a scanning probe microscopy (SPM) technique. A small cantilever is used to scan the surface in contact, non-contact or tapping mode. The attraction forces in between the tip and the surface change depending on their distance. The atomic force microscope NanoScope IIIa MultiMode from Veeco was used to perform analyses. Measurements of the topography in dry conditions were carried out. Antimony doped Si tips (model RTESP) from Veeco and Bruker respectively were used for imaging in tapping mode with spring constant in between 20-80 N/m and resonance frequencies in between 200 and 400 kHz. The resonance frequency can be determined via *auto tune* in the software. The images were scanned with a speed of 1-2 Hz with 256 or 512 lines per image. The measured data was further processed with the analysis program Gwyddion for Windows to obtain flattened images, roughness values or height profiles. Flattening was carried out with the Gwyddion functions *level data by mean plane* to remove effects that come from tilted samples, followed by *line correction by comparing the height median* to get rid of scanning effects for a smoother image. The function *statistical values* displays roughness values of the sample.

### 2.4.2. Static contact angle

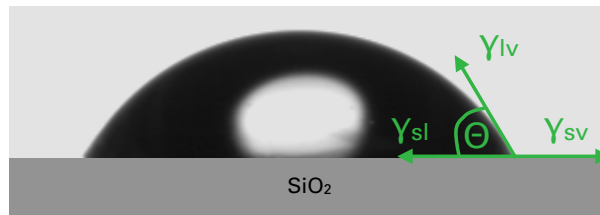


**Figure 2.10.:** A deposited water droplet on a  $\text{SiO}_2$  surface. Measuring the contact angle  $\theta$  enables the calculation of surface tensions  $\gamma$  between droplet, air and surface.

By applying various liquid droplets onto a surface, its surface properties can be characterized, see Figure 2.10. The contact angle  $\theta$  of a droplet depends on both the surface chemistry and the surface roughness. Three interfaces meet here: liquid, air and solid substrate. Between all of these three partners, a certain surface tension  $\gamma$  is characteristic, *e.g.*  $\gamma_{sl}$  for the interface between solid substrate and the droplet. Thus, the surface tensions of all components play a role. If the contact angle of a water droplet with the surface is below  $90^\circ$ , the surface is called 'hydrophilic' with a good wetting behaviour, whereas above  $90^\circ$  the 'hydrophobic' surface shows a poor wetting ability. Figure 2.10 is an example for a hydrophilic surface. Immediate spreading of the droplet is not measurable and classified as having a contact angle 'below  $10^\circ$ '. In case of full wetting behaviour, the Antonow relation applies:

$$\gamma_{sv} = \gamma_{sl} + \gamma_{lv} . \quad (2.1)$$



In case of incomplete wetting behaviour, the Young's equation can be used to calculate the surface tensions and includes the measured contact angle.

$$\gamma_{sv} = \gamma_{sl} + \gamma_{lv} \cos \Theta_l . \quad (2.2)$$

The contact angle of degassed dI water droplets on wafer or glass substrates was obtained with the sessile drop method with needle out using the Dataphysics Contact Angle Systems OCA device. For all measurements, 1.5  $\mu\text{l}$  at medium speed were deposited onto the surface and analyzed right after (approximately 2 s after deposition) as the contact angle changes with time. Each surface was measured with the maximum possible number of droplets for statistics.

### 2.4.3. Ellipsometry

Ellipsometry is an analytical method that detects changes in the polarization state of polarized light when a laser beam is reflected on an even surface. The ellipsometer SE400advanced (Sentech instruments) uses reflection on planar wafer surfaces for thickness determination of layers. The laser signal is converted to thicknesses  $d$  and/or refractive indices  $n$  based on a model which approximates the optical properties of the sample. From a given refractive index for the layers below and above the layer of interest,  $d$  and/or  $n$  can be modeled in dependency of the measured signal. A schematic layer model is presented in Figure 2.11A) with Si below and air above the oxide. In contrast to the chemical functionalization layers, the refractive index of  $\text{SiO}_2$  is known. To solve this problem, the index of  $\text{SiO}_2$  of 1.4567 can be taken as an initial value for the chemical functionalization layers and act as an approximation [162]. By subtracting the oxide from the total thickness after functionalization the molecular layer thickness can be determined, see Figure 2.11B). The angle of the laser beam is variable but was usually fixed to  $70^\circ$  for dry conditions. The evaluation of the thickness of lipid bilayers requires liquid conditions. The QG synthetic quartz glass precision cell (Hellma Analytics) for liquid measurements requires a fixed angle of  $67.85^\circ$  as a prerequisite due to the angle of the measurement cell side walls.

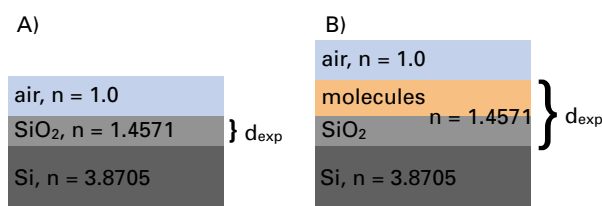


**Figure 2.11.:** Layer model to determine the thickness  $d$  of layers on Si wafers with ellipsometry. A) Fixed refractive indices for Si, air and the oxide layer allow to determine the oxide thickness. The same measurement is carried out with functionalized wafers in B). Thickness of the oxide plus the molecular layer are determined with the fixed refractive index of  $\text{SiO}_2$ . Subtraction of the value obtained in A) results in  $d$  of the molecular layer.

#### 2.4.4. Zeta potential

Zeta potential is a measure for the electrostatic interaction in between particles in a solution (colloidal solution). It is a useful parameter to evaluate the risk of agglomeration of particles which might occur due to an unfavourable ratio of repulsive and attracting forces.

Attractive forces arise due to van der Waals forces between particles. Repulsive forces originate from the electric double layer. The double layer has a typical thickness, the Debye length (see section 1.4.3), which is dependent from the ionic strength of the solvent. A double layer consists of two layers, the Stern layer close to the surface with counterions to the surface charge of the particle. It is firmly attached to the particle and moves with the particle. This layer is surrounded by the diffuse layer with ions which are less tightly bound. They stay with the bulk solution when the particle is moving. The resulting shear force in between these layers is characterized by the zeta potential. It is a measure for the surface charge and its sign. A high absolute zeta potential indicates a high number of surface charges per area. Any increase in the zeta potential will stabilize the solution as the risk for agglomeration because of attractive forces is minimized. As a threshold, zeta potentials with an absolute value of 30 mV or higher are regarded to support the formation of stable colloidal solutions according to the instrument supplier Malvern.

The aim of surface functionalization of particles is to increase the repulsive interactions by creating a higher absolute surface charge. The parameter zeta potential indicates the success of a functionalization scheme. The samples here were measured with a Zetasizer nano ZS (Malvern Instruments Ltd.) which is also capable to determine the particle size of circular particles by Dynamic Light Scattering (DLS). The device is limited to a minimum of 0.3 nm in diameter up to 10  $\mu\text{m}$ . The SiNWs with 20 nm diameter and typical lengths less than 10  $\mu\text{m}$  after sonication can be analyzed in terms of zeta potential, the size however only may indicate agglomeration with time but not the real particle size due to the high aspect ratio of nanowires.

#### 2.4.5. Fluorescence microscopy

The inverted microscope Axiovert 200 from Zeiss was mainly used with the 10x objective. Where indicated, images were taken with a different magnification. The microscope is connected to a Photometrics Cascade 512B camera, a halogen lamp for fluorescence and a shutter to control the fluorescent illumination of any sample. The available filter sets from Zeiss for detection of fluorescence are 9, 10 and 15 with the following specifications – 9: **BP** 450-490 **FT** 510 **LP** 515, 10: **BP** 450-490 **FT** 510 **LP** 515-565 and 15: **BP** 546/12 **FT** 580 **LP** 590. For the experiments presented here, corresponding dyes were chosen. 9 and 10 are very similar and well suited for green fluorescence like fluorescein dyes. Filterset 9 however emits a broader spectrum and thus set 10 with narrower window was used in those cases where red and green fluorescence had to be distinguished (see sandwich assay in section 3.1.2). To present the images here, the raw files (16-bit) were treated with the software ImageJ. Brightness and contrast adjustment as well as background subtraction were used to optimize the image, colour green was chosen for fluorescein dyes and red for rhodamine red dye in the setting "Lookup Tables".

Taylor *et al.* state that it is possible to obtain an optimized fluorescence signal for fluorescently labeled ssDNA depending on their length. For 30 bases, a concentration of 10  $\mu\text{M}$  is plotted and for 60 bases only 5  $\mu\text{M}$  are necessary. As the used aptamer is slightly shorter (around 20 bases with spacer nucleotides), a concentration above 10  $\mu\text{M}$  is probably required. This is tested in section 4.1.1.

For a comparative intensity analysis of protein detection on microarrays, the data analysis was carried out as described in the following and in Römhildt *et al.* [163] implementing the untreated raw data. The results are presented in section 4.1.2.

The microscope settings were kept constant during all measurements. For the concentration measurements the exposure time for rhodamine red-labeled aptamer was set to 1 s giving sufficient intensity for the investigated range of thrombin concentrations. The collected raw data was automatically flattened by point-wise division with a fourier transform based low-pass filter with a hard cutoff-frequency at 3 over image width that was implemented in a matlab (Mathworks, Inc.) script. The local background signal in passivated areas (background B) and the fluorescence signal in functionalized detection areas (fluorescence F) of the flattened image were then determined for each stripe or circular spot, finally resulting in a fluorescence intensity amplification ratio (F2B). It is important to note that flattened images as well as the final signal F2B are calculated as ratios of intensity data which makes data comparable among experiments with different illumination conditions due to lamp intensity fluctuations and adjustment variations. For largely unbiased analysis, threshold values between dark and bright image areas were automatically determined using the matlab script. Fluorescence and background intensities were averaged for each spot, as shown in Römhildt *et al.* [163].

For each concentration of the nanoplotted samples, 7 different areas (each with 4 spots) per concentration were analyzed row by row. Although this method includes the dark corners due to the circular signal area, their effect on the F2B value is small and thus accepted in favor of a fast analysis. The automated analysis of the stripe samples is identical although here the results do not suffer the mentioned circular image area problem as one stripe represents a rectangular area which is vertically aligned [163]. Each image delivers 14 F2B values. For each concentration, 3 images were averaged.

## 2.5. Characterization techniques for receptor-analyte interactions

In addition to the techniques introduced for surface modification to localize receptors at the surface, further techniques are available to investigate the interaction of receptors and analytes in solution (gel electrophoresis) and on transducers (quartz-crystal microbalance, FET sensor).

### 2.5.1. Electromobility shift assay with native polyacrylamide gel

Electromobility shift assays (EMSA) carried out via gelectrophoresis use the ability of charged molecules to migrate in porous gels if an external voltage is applied. The migration distance is dependent from the ratio of the molecule, the pore size and the applied voltage. Small or strongly charged molecules move fast and thus a longer distance within the same time than larger ones. Due to this, pools of dif-

ferent types of molecule (DNA strands, proteins) can be sorted. By staining the molecules, the colour indicates their position in the gel. In principal, two main different gels are used – agarose and polyacrylamide gels (PAGE). PAGEs can be subdivided into native and denaturing gels. The sensitivity at low concentrations is higher for PAGE than for agarose. After testing this, further experiments were exclusively carried out using an acrylamide gel. As PAGE aimed at investigating protein-DNA interaction, native gels that do not destroy the proteins which were used. PAGE consists of acrylamide and bisacrylamide mixed with buffer that polymerize after addition of crosslinkers. By changing the ratio of the acrylamide and the added buffer, the pore size is altered. After mixing, the gel is casted into a gel chamber from Bio-Rad Laboratories. To create the starting points, a plastic comb is added defining the number of gel pockets. After solidification, the prepared mixtures of molecules and the loading dye are inserted into the pockets. The loading dye stains the solution and supports sinking of the molecules into the pockets. An external voltage is applied to initiate migration (parameters see appendix A.5). Before imaging, the gel is immersed in DNA or protein staining solutions. Destaining to enhance the signal-to-background ratio works best when KCl is present in the buffer solution (not shown here). Images can be taken directly or with dried gels. In order to store the gels, it is possible to dry them put into a frame in between two sheets of cellulose paper. The protocol for investigating receptor-analyte interactions can be found in the appendix A.5.

The goal here was to investigate the interaction of aptamers with proteins in solution to verify that the molecules are interacting with each other. By this, problems that occur after attachment of the receptor during biorecognition experiments can be attributed to the experimental conditions themselves (*e.g.* perturbed aptamer folding).

### 2.5.2. Quartz-crystal microbalance with dissipation monitoring

Quartz-crystal microbalance (QCM) biosensing is a realtime, solution-based method which monitors the mass changes on surfaces. The quartz crystal is piezoelectric and oscillates. This oscillation is reflected in a frequency. Molecular events on the surface alter these frequency characteristics – the sensor signal. QCMs with dissipation monitoring (QCM-D) oscillate with a certain frequency when a voltage is applied. Turning of the voltage leads to a frequency decay with time. This decay is damped by any molecular event on the surface. The decay analysis allows to monitor the thickness changes and the viscoelastic properties of the thin film. With increasing film softness the damping happens faster. Not only attachment and detachment processes but also trapped water influence the sensor signal. In QCM-Ds, the frequency and the dissipation are analyzed simultaneously and mass, density and thickness changes can be determined by using different mathematical models. The frequency decreases whereas the dissipation increases for an increasing layer thickness. In the case of rigid layers, the frequency decrease is linearly proportional to the layer thickness increase (Sauerbrey relation [164]). Viscoelastic properties are usually present for the measurement in liquids with multilayers, proteins, lipids or DNA hybridization. The presence of viscous and elastic properties are taken into account in the model proposed by Voigt. All analysis was carried out using the corresponding software QTools.

The quartz crystal in one QCM chip is sandwiched in between two gold electrodes. Most commonly,

the upper gold electrode is functionalized and used for studies. By further coating it is possible to investigate functionalization and receptor-analyte interaction on other surface as well. The QCM-D device E4 from Q-Sense contains four chip stations for parallel measurement. The fluids are delivered via a peristaltic tube pump which is integrated in between the device and the waste bottle and pumps with a maximum velocity of 200  $\mu\text{l}/\text{min}$ .

Here, QCM-D sensor chips of gold with a appr. 50 nm thick silicon dioxide layers were functionalized and measured in order to compare the results to the SiNW FET biosensor.



## 3. Receptor-target combinations

After presenting and discussing the chemical surface functionalization techniques and the selected applications thrombin and amoxicillin, the attachment strategies based on these findings for two receptor types – aptamers and antibodies – are discussed in the following. The aptamers are involved in a sandwich assay whereas the antibodies are embedded in an inverse competition assay.

### 3.1. Aptamer based sensing

#### 3.1.1. Aptamer design

The DNA sequences and the chosen functional groups, see Table 2.1 at both ends result from findings in the literature. After choosing the aptamer-target combination of interest, the design of the aptamer for attachment onto the sensor surface is important. The general requirements are a strong, reliable and oriented attachment of the receptor while maintaining its function towards the target. As discussed in section 1.2.2, both ends – 3' and 5' – are suitable for attachment. Modifications at the 5' end lead to a higher production yield as it is easier in synthesis. The attachment via the 3' end however reduces the risk of an attack. In the case of the thrombin binding aptamer (15mer), Baldrich *et al.* found out that attachment to the surface via the 3' is slightly more efficient in detecting thrombin [47]. In order to separate any terminal functional group from the actual folding region, additional spacers are often introduced [47, 55, 56]. The integration of spacers is important for the success of the immobilization scheme as they reduce the influence of covalent immobilization; the aptamer structure is thus little affected. They may consist of further nucleotides – mostly polyT or polyA chains. Any possible interference with the aptamer sequences should be checked or tested. A second common way is to use carbon chains. Both ways can also be combined. When labeling of the aptamer with a fluorophore or other molecules is required, separation from the aptamer sequence is equally recommended.

The limited availability of filter sets (see section 2.4.5) determines the possible choices of fluorescent dyes. To confirm the attachment of the receptor TBA1, green fluorescence, *i.e.* a fluorescein dye called FAM (fluorescein amidite) was selected. The 5' end was fluorescently labeled to be able to link TBA 1 covalently to the surface via the 3' end, and as a spacer a combination of a carbon  $((CH_2)_n)$  and polyT chain was chosen. In order to be able to distinguish aptamers with the available filter sets, the second aptamer TBA2 was labeled with a red dye (rhodamine red).

As a control, a scrambled sequence of similar length was compared to TBA1 to show the specificity of TBA1 towards thrombin. Thrombin and the complementary strand to TBA1 compete due to a different affinity. Earlier publications used the displacement of the complementary strand to enhance

the signal of thrombin detection. The complementary strand was used here for investigations with gelelectrophoresis.

### 3.1.2. Sandwich assay for optical detection

The following paragraph is part of a recent publication [163]. The two available thrombin binding aptamers TBA1 and TBA2 bind to two distinct recognition sites of thrombin and can thus be used to realize a format of sandwich assay [25, 165–168] as illustrated in Figure 3.1, central scheme. The shorter aptamer TBA1 (15mer) recognizes the fibrinogen binding sites, the longer 29mer TBA2 specifically attaches to the heparin binding site [25, 64]. The first aptamer labeled by fluorescein amidite (FAM - green) proves the covalent attachment of the capture aptamer (TBA1) to the substrate surface. After the injection of analyte solutions, the second aptamer (TBA2, labeled by rhodamine red) is aimed to assure the presence of the thrombin at the surface and to quantify the concentration of the molecules captured during the assay. Once the concentration of thrombin in solution changes, the resulting fluorescence signal caused by labeled TBA2 varies. Thus, the biorecognition process happens twice during the assay, which improves specificity of the method, and can lead to an increased signal and a lower detection limit. In order to further enhance the fluorescence-to-background amplification ratio (F2B) of the experiment and to simplify the interpretation of the results, the thrombin detection regions are defined by chemically patterning glass surfaces in form of microarrays (see Figure 3.1) using microcontact printing (A) and nanoplotting (B).

### 3.1.3. Aptamer attachment strategy

As described in section 1.2, the most abundant groups receptors offer are primary amines, carboxy groups, thiols or aldehydes. In this work, the main focus was on functionalization strategies for primary amine attachment. Amines can form stable bonds with carboxy or epoxy groups in contrast to interaction with aldehydes. Here, the resulting imide bond might degrade in water and requires additional stabilization by sodiumborohydrate [59, 98]. Carboxy termination was not possible as it is not carried out easily and rarely offered by DNA synthesizing companies. The aptamer design was carried out in such a way that the primary amine was linked to the 3' end with a combination of a polyT and a carbon chain spacer. By this, perturbations of the aptamer folding region due to the surface binding are reduced. Based on an organosilane layer, functionalization strategies are described in section 2.1 to covalently attach amino-terminated aptamers to silica surfaces functionalized with either APTES and succinic anhydride for amide bond formation or GOPMS for aminoalcohol bond formation (see section 2.1.2).

### Blocking strategies

The goal of any biosensor is to detect a certain species and being able to distinguish it from unspecific attachment of others molecules in the solution. The sensor signal should also derive from specific biorecognition and not unspecific attachment due to analyte adsorption. Both events (false biorecog-



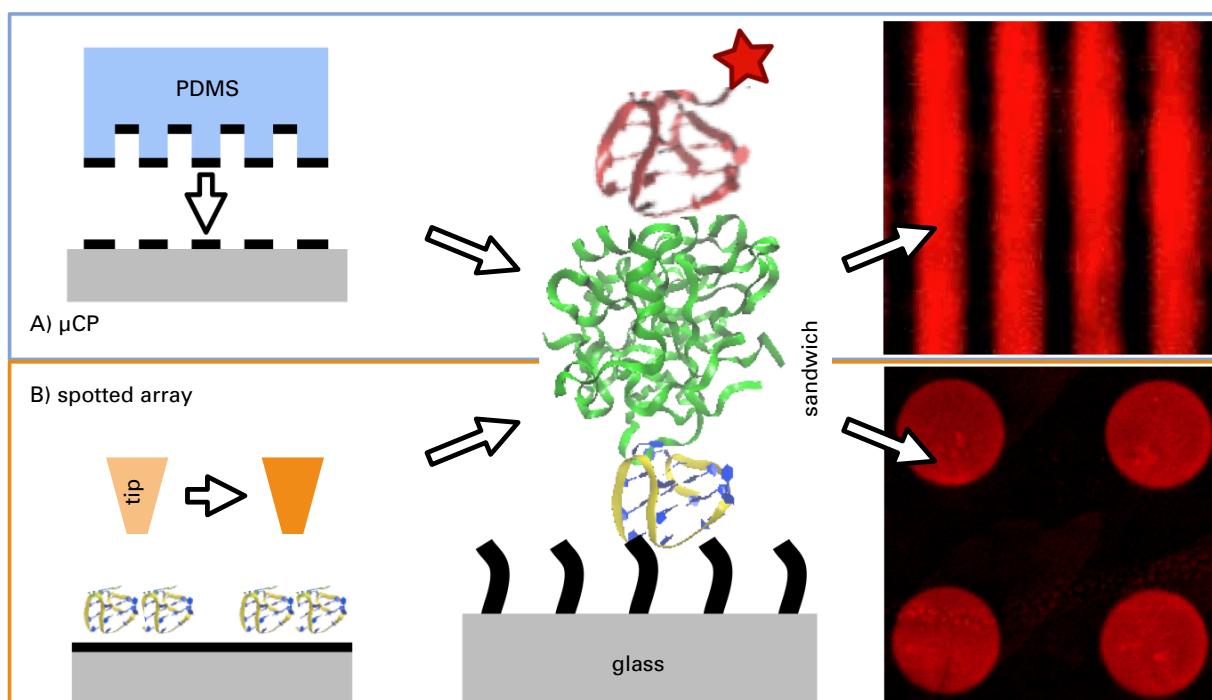


**Figure 3.1.:** Schematic drawing of sandwich assay in central scheme with surface bound TBA1 and TBA2 for dual thrombin recognition. TBA2 is labeled with a red dye to highlight the thrombin detection regions. The regions are predefined using surface patterning techniques: route A) shows the principle of microcontact printing of silane stripes and route B) illustrates nanoplotted microarrays of TBA1 onto functionalized glass slides.

nition or unspecific attachment of other molecules or the analyte itself, respectively) lead to false sensor signals or simply to a high background signal. Strategies to avoid such unspecific attachment are summarized under the term "blocking strategies". They can be subdivided into chemical and biological routes. The first one is necessary to saturate any unreacted terminal group to avoid covalent bonding or other interactions with molecules in the solution. Chemical blocking turns reactive into much less reactive and uncharged surface groups, like ethanolamine to block unreacted amine-reactive surface groups [169]. One can also attach chemical molecules that hinder protein adsorption. A common way for this are molecules with a terminal polyethylenglycol (PEG) which make the surface hydrophilic and thus less attractive for proteins. In order to avoid the unspecific adsorption of DNA it is also possible to attach succinic anhydride (SA) as DNA possesses a low affinity for SA-surfaces [138]. Referring to the previously presented strategy based on APTES and further carboxylation it is possible to show the success of EDC/NHS activation by leaving out this step for a control sample very effectively as the DNA is not very likely to adsorb onto the SA-surface. Taylor *et al.* could also show that the use of GOPMS leads to low background signals in a microarray hybridization assay as in this case no blocking showed the best signal-to-background ratio [138]. However this accounts only for undesired DNA adsorption, for proteins additional blocking is probably required.

Chemical functionalization involves the use small organic molecules which lead to rather rigid

surfaces which are not very supportive for biological species which prefer soft matter as it provides a more biocompatible environment for the receptors and approaching analytes. Proteins tend to adsorb onto many surfaces. Detection of a specific protein out of a pool of proteins *e.g.* blood is thus hindered. The situation can be improved by using biological blocking strategies after the chemical ones. By using a defined amount of protein, the surface is blocked after receptor attachment but before bringing it into contact with the analyte solution. Many publications introduce blocking with bovine serum albumine (BSA) as it was also carried out for experiments in these theses [3, 58, 59, 103, 138, 165, 170–172]. Other potential molecules are milk powder and intense washing protocols including the addition of Tween-20 or SDS [59].

## 3.2. Antibody based sensing

### 3.2.1. Inverse competition assay

To detect amoxicillin and other antibiotics, monoclonal antibodies are available for purchasing. Thus, an antibody based setup for biosensing was selected. With these antibodies, 200 pg/ml can be detected (see datasheet in appendix). In aqueous environment, amoxicillin transforms and the  $\beta$ -lactam ring opens (structure with closed ring in Figure 2.9). Lamm *et al.* proposed a mechanism of amoxicillin degradation in aqueous medium [5]. The commercially available monoclonal antibodies are especially reactive towards the open ring (see datasheet in appendix). Amoxicillin is also a small molecule and not charged strongly. Thus, FET based biosensing can be challenging. To overcome these two points, an inverse competition assay was adapted from Scott *et al.* [161]. To realize an inverse assay, amoxicillin itself will be attached to the surface covalently. Two potential groups are possible – the carboxy group COOH and the primary amine NH<sub>2</sub>. Due to the above described antibody specificity towards the open  $\beta$ -lactam ring, it was chosen to attach AMX to the surface (= **surface-AMX**) via the free primary amine as it is not in direct vicinity of the  $\beta$ -lactam ring where the antibody is supposed to bind, in contrast to the carboxy group being much closer (see Figure 2.9). A simplified setup was introduced (inverse assay, see Figure 3.2A). After attachment of surface-AMX, the chip was incubated with antibody solutions of increasing concentrations as a proof-of-concept and directly measured with the FET device (surface-AMX and black antibody in Figure 3.2A). For preliminary tests on wafers, the chip was further incubated with a specific secondary antibody (grey antibody), which is conjugated to a AuNP. The AuNPs are visualized with SEM. In order to detect different concentrations of amoxicillin in a sample solution, the inverse assay was combined with a competition assay (see Figure 3.2B). Before incubating with the chip, the sample solutions with AMX (= **sample-AMX**) were mixed with antibody solution of a constant concentration. In highly concentrated AMX solutions, many antibodies will already recognize the sample-AMX and are not free for later recognition of surface-AMX when applied onto the chip. AMX sample solutions of lower concentrations on the contrary will offer many free antibodies available for recognition of surface-AMX. As a result, high sample-AMX concentrations lead to a low, highly diluted sample-AMX solutions to a high FET signal (see also [161]).

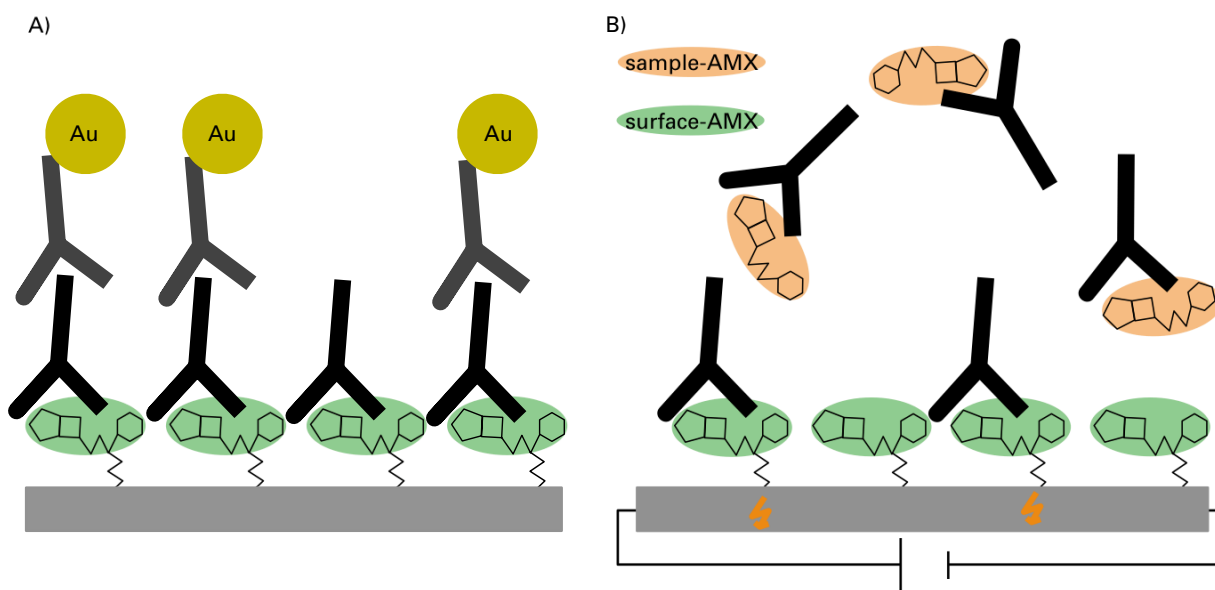


**Figure 3.2.:** AMX assays. A) Surface-AMX molecules are recognized by the anti-AMX antibody. This is visualized for analysis with SEM using secondary antibodies which are specific for the Fc end of the anti-AMX antibodies. B) Inverse competition assay with surface-AMX molecules and sample-AMX, incubated with the anti-AMX antibody prior to applying the antibody-AMX solution onto the surface with surface-AMX for recognition using FET current modulation.

### 3.2.2. Attachment strategy

As presented in section 2.1.2, GOPMS attachment to  $\text{SiO}_2$  results in an epoxy-terminated surface which forms covalent bonds with primary amines at pH values slightly higher than physiological pH. The formed aminoalcohol is relatively strong in aqueous solutions and not cleaved easily. The surfaces for AMX sensing were functionalized using the over night gas attachment from the gas phase (see appendix A.1). This was followed by incubation with AMX in PBS buffer, tuned to pH 8.5 using 1 M sodium hydroxide for 30 min, and rinsing in buffer and water. After this, the increasing concentrations of the antibody solution (simplified, inverse setup) and the samples with decreasing AMX concentrations at fixed antibody dilution (competition assay) were applied in 25  $\mu\text{l}$  droplets onto the surface. After each step, the I-V curves were recorded. Applying the antibody containing solution, the FET devices were measured after 10 min of incubation. Details of the protocol can be found in appendix A.1.



## 4. Biochemical Functionalization and Biosensing

In the previous chapters, the concepts and characterization methods were described. This chapter deals with the results of biochemical functionalization and interaction of immobilized receptors with the analyte in solution. The first part includes the results for chemical functionalization and aptamer based sensing of thrombin in a sandwich assay whereas the second part adds results obtained for antibody based sensing of amoxicillin. The third part makes an excursion to the use of nanowires in solution as versatile tools of bionanotechnology for characterizing functionalization steps and as templates for one-dimensional lipid bilayers.

### 4.1. Thrombin detection

#### 4.1.1. Biochemical modifications

##### Contact angle measurements

After carrying out the previously described cleaning procedures and the activation of hydroxyl groups by air plasma or with solvent-based methods (see section 2.1.1), the surface is very hydrophilic. This is indicated by complete spreading of the applied water droplets when measuring the contact angle (CA). In case no contact angle can be determined on any substrate, this is categorized by definition as 'below 10°', as described in section 2.4.2.

Depending on the size of the sample, a certain number of droplets was measured - usually 4-5 droplets per sample, except for liquid phase adsorption of GOPMS (wafer) and APTES (wafer and glass) where 8-9 droplets were measured. All presented values in Figure 4.1 are the average of two different samples, except for all succinic anhydride (SA) modifications and the APTMS sample on a wafer (from the liquid phase), which only average from droplets on one sample. The mean values and their standard deviations were determined from these droplet measurements.

Figure 4.1 shows all contact angles with the respective incubation time of the modification step on the x-axis in log scale. Here, the region below this threshold value is marked with a grey bar. Leaving bare and hydroxylated samples in N<sub>2</sub> at 4°C for 48 h does not significantly alter the contact angle, it is still 'below 10°'. Going through the same process of heat treatment as the functionalized GOPMS samples (without any chemical agent), the contact angle increases to around 52.43° ± 1.31° for wafers (filled black square symbol in graph).

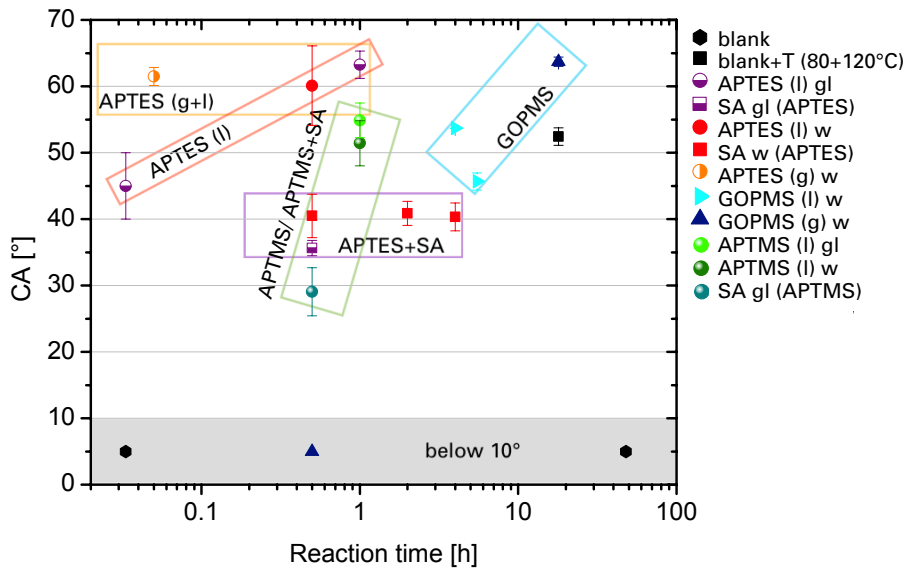


**Figure 4.1.:** Mean contact angles of 1.5  $\mu\text{l}$  dI water droplets on wafer (w) and glass (gl) substrates after functionalization with organosilane APTES, APTMS or GOPMS using liquid phase (l) and gas phase (g) attachment procedures. The change of the contact angle after attachment of succinic anhydride (SA) is included, too. The coloured frames are a guide to the eye to group the results.

The same organosilane was applied onto the activated surfaces using different methods – from a diluted silane solution in an ethanol-water mixture (ratio 95:5) as well as from the gas phase using pure silane. Silane evaporation was carried out either by vacuum treatment in a Schlenk tube system or by heating in an oven. The different results are collected and presented in Figure 4.1 for the silanes APTES, APTMS, GOPMS and the further crosslinking with SA to the amino terminated surface.

Immersion of glass slides or wafers in APTES solutions for incubation times of at least 30 min resulted in contact angles of around  $60^\circ$  (filled red and half-filled violet circle at 30 min and 1 h). This corresponds well with the previously reported value of  $58.4^\circ$  [162] and the obtained value is also within the range presented by Janssen *et al.* [140]. Short incubation of only 2 min however on glass slides leads only partially to a molecular surface coverage with a contact angle of around  $45^\circ$ . Gas phase evaporation in a small Schlenk tube only requires vacuum pumping of 2 min and further waiting of 1 min to achieve a contact angle around  $60^\circ$ , see section 2.1.2. Longer times do not increase the contact angle significantly. The difference between wafers and glass slides as well as between liquid and gas phase adsorption is negligible. It could be observed that poor silane quality (ageing) and storage in ambient conditions prior to measurement lead to reduced contact angles (the latter *e.g.* resulted in a contact angle of only around  $45^\circ$  instead of  $60^\circ$  for 1 h of incubation). More important are thus a certain minimal incubation time, the freshness of the silane solution and the way of storage until measurement. Samples should be kept in  $\text{N}_2$  and at  $4^\circ\text{C}$  until characterized.

The contact angle of water on functionalized wafer and glass samples significantly decreased after

attachment of succinic anhydride to create terminal carboxy groups. The three red filled squares represent three wafer samples functionalized with APTES after crosslinking. The contact angles deviate around  $40^\circ$  for three different incubation times, namely 30 min, 1 and 2.5 h. Thus, a reaction time of 30 min is sufficient for surface functionalization. During the attachment procedure, succinic anhydride (SA) was dissolved in the organic solvent DMSO and injected directly onto the sample which was immersed in buffer to allow the immediate reaction to happen at the surface. This indicates that the main reactions are finished after 30 min resulting in constant angles even for longer reaction times. The contact angle on a modified glass slide was similar (around  $35^\circ$ ). It could be observed that the angle after SA attachment is also dependent from the angle after APTES treatment. Higher CAs here are mostly followed by SA-CAs in the upper range as well. But the difference from APTES to SA should always be roughly around  $20^\circ$ . This is additionally confirmed by the results for APTMS and subsequent SA attachment. APTMS shows a CA of only  $51^\circ$  (filled dark green ball in graph) on wafers and  $54^\circ$  on glass slides for an adsorption time of 1 h. After SA crosslinking, the angle is reduced down to less than  $30^\circ$ , but the difference is again around  $20^\circ$ . Longer incubation times of the methoxy silane with terminal amine were not carried out as the silane was not used in ongoing experiments. They could however lead to a further increase in the CA as the methoxy groups require more time to react [101].

GOPMS attachment in ethanol-water (ratio 95:5) required longer incubation times due to the slower reaction of methoxy groups [98] (see also section 1.3.2). Samples were incubated for 4 h and 5.5 h on a heating plate set to  $50^\circ\text{C}$  which was adapted from the protocol of Hermanson [98], p. 579. With increasing incubation time, the contact angle decreases, indicating molecular stacking and thus the occurrence of different chemical groups sticking out which might reduce the contact angle. The gas phase attachment with pure silane on wafers in an oven overnight at 80 and  $120^\circ\text{C}$ , respectively, was adapted from Tarasov [105]. This method created a contact angle of  $63.70 \pm 0.69^\circ$ , with little variation within one sample. The angle is also significantly higher than the corresponding control (black filled squares: blank + heat). The procedure was chosen for attachment as it is also the least harmful way for the SiNW chips reducing any risk for contamination and damage.

Contact angle measurements are a fast indicator whether the reaction has been carried out successfully or not. Larger deviations from the expected value range mostly give hints for problems in the experimental setup like incubation time, ageing of the solution or other irregularities. If the CA differences after any modification are small compared to the previous step, it is however not the most accurate measurement. This was not the case for the applied molecular layers of silanes and succinic anhydride. It cannot be used for further attachment steps of biomolecules (DNA, proteins) as the contact angle changes were not clear enough (results are not presented here). Other techniques are necessary.

Multiple measurements, especially with different APTES methods and stock solutions were carried out throughout the years. Most importantly, the angle should be around  $60^\circ$ . A value in between  $55^\circ$ - $70^\circ$  is normal, the reduction should be at least  $15^\circ$  for SA attachment. Determination of the contact angle can also be used to show the homogeneity of surface functionalization. In liquid phase methods,

a reduced CA and layer thickness was observed in regions near the edges. This was not observed for gas phase samples. One explanation is that these samples were less in contact with tweezers which might lead to local layer removal.

### Attenuated total reflectance Fourier transform infrared spectroscopy

Attenuated total reflectance Fourier transform infrared spectroscopy (ATR-FTIR) is a spectroscopy method carried out on ATR crystals (Si wafers with defined side angles) to confirm the formation of covalent bonds on surfaces as it detects the characteristic bands. An evanescent wave is coupled into the crystal and undergoes multiple reflections. The molecular layer is in direct contact with this crystal and influences the reflectance angle. A range of frequencies is scanned and the sample is compared with the blank crystal before functionalization.

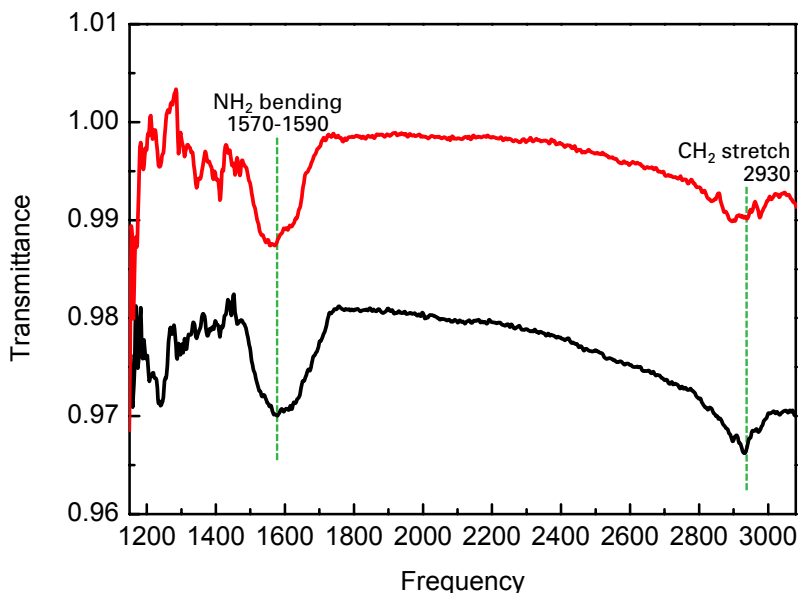


**Figure 4.2.:** Transmittance as a function of the applied frequency of two APTES functionalized ATR crystals. The peaks with a center at  $1570\text{-}1590\text{ cm}^{-1}$  and  $2930\text{ cm}^{-1}$  correspond to the  $\text{NH}_2$  bending and the  $\text{CH}_2$  stretching which confirm the presence of the aminosilane.

Figure 4.2 shows the transmittance as a function of the frequency for two different APTES functionalizations (adsorption in solution) on a crystal. The samples were characterized after surface functionalization of diluted APTES in an ethanol/water mixture for 1 h (see appendix A.1), followed by intense cleaning in ethanol and water before postbaking. Both curves exhibit distinct peaks which are centered at around  $1570\text{-}1590\text{ cm}^{-1}$  and  $2930\text{ cm}^{-1}$ . This is in excellent agreement with the peaks for  $\text{NH}_2$  bending and  $\text{CH}_2$  stretching [173, 174]. The spectroscopy measurement confirms the presence of the aminosilane on the  $\text{SiO}_2$  surface.



## Ellipsometry

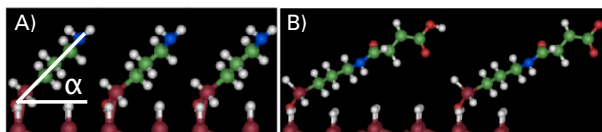


**Figure 4.3.:** Schematic model of the theoretical thickness calculated from the molecule structure using iMol, a molecular viewer for structures for Mac OS X for different angles of a perfect monolayer from 90 (straight) down to appr. 35°. A) illustrates an APTES layer at  $\alpha = 37.23^\circ$ . B) shows covalently attached APTES and SA at  $\alpha = 32.27^\circ$ .

With ellipsometry, the additional layer thickness on top of the native  $\text{SiO}_2$  was determined after each chemical functionalization step. The layer model is explained in section 2.4.3. On each wafer piece, six data points and two samples per mean value were measured. Theoretically, the expected thickness for an ideal monolayer was calculated for straight and tilted molecules, as illustrated in Figure 4.3A) for APTES (37.23°) and B) for APTES + SA (32.27°). The corresponding values are listed in Table 4.1. After measuring APTES, APTES + SA and GOPMS, layer thicknesses of 0.7-1.0 nm, 1.1-1.2 nm and  $0.63 \pm 0.05$  nm, respectively, were determined. They correspond well with the theoretically calculated values. As discussed in section 1.3.2, such perfect monolayers as in the model (see Figure 4.3) cannot be found in reality. Real layers will be irregular with molecular stacking. Interexperimental deviations of identical experiments were small which confirms the accuracy of measurement. To evaluate the ellipsometry results, the technique is a good and quick indicator whether the modification was successful or not, but it should be used in combination with other methods.

**Table 4.1.:** Ellipsometric thickness of chemical layers in comparison to calculated values for straight to tilted layers (see Figure 4.3).

Layer type	$d_{theo}$ [Å]	$d_{exp}$ [Å], $t_{0.5h}$	$d_{exp}$ [Å], $t_{1h}$	$d_{exp}$ [Å], $t_{18h}$
$\text{SiO}_2$	$\sim 2$	/	/	/
APTES	4 - 7	7 - 10	8 - 12	/
APTMS	4 - 7	/	6 - 9	/
APTES + SA	6 - 12	9 - 11	/	/
GOPMS	4 - 7	/	/	6 - 7

## Gold nanoparticle labeling

To label the attachment of functional groups on surfaces, gold nanoparticle (AuNP) labeling was applied additionally. Generally, NPs in aqueous NP solutions are covered with functional groups to avoid agglomeration via electrostatic repulsion of the individual particles. Often, this stabilization is achieved via citrates which is a residue of the fabrication procedure. This results in negatively charged nanoparticles. They can be used to label positively charged functional surface groups due to electrostatic attraction. Terminal surface amines are protonated at pH values below their isoelectric

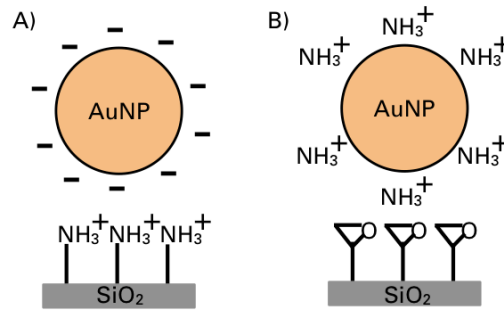


**Figure 4.4.:** AuNP labeling via A) electrostatic interactions or B) covalent bonding of amino-NPs to an epoxy-terminated surface. This sketch shows the situation prior to covalent bond formation.

point (pI), which is above pH 10 for primary amines [175]. Wu *et al.* have shown that aminosilane layers on silica particles however only show a pI of 9 and for coated SiNWs the pI was even lowered to approximately 6.5 but with a very similar  $\zeta$ -potential at pH 6 of around 20 mV [84, 176]. Thus, dI water (pH around 6) can be used for this experiment. Functionalized samples were immersed in the diluted NP solution for 3 h and then rinsed with water three times before blowing dry in  $N_2$ . The wafer samples were analyzed using SEM as the NPs give a good contrast compared to the  $SiO_2$  surface. Silicon dioxide surfaces are slightly negatively charged at the same pH which should hinder AuNP adsorption.

For epoxy-terminated surfaces covalent bonding was used instead of electrostatic interactions. For this purpose, amine functionalized NPs were diluted in PBS buffer tuned to pH 8.5 prior to immersion of the wafer samples.

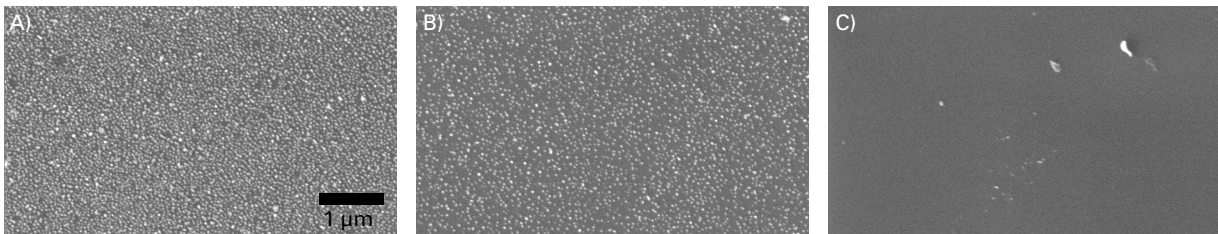


**Figure 4.5.:** AuNP labeling of terminal functional surface groups on oxidized Si wafers. Negatively charged AuNPs label protonated APTES (A) and APTMS (B) surfaces. C) The control blank shows almost no NPs on its surface. Scale bar is valid for all three images.

Aminosilane surfaces are densely covered with a layer of AuNPs, as presented in Figure 4.5 A) for APTES and B) for APTMS, the negatively charged NPs are strongly attracted by the positive surface charge due to amine protonation. The blank control sample (Figure 4.5 C) is almost AuNP-free. This clear difference can thus be well explained by the fact that the NPs are specifically labeling the functionalized surface and are repelled from the negatively charged oxide surface.

AuNP labeling allows to visualize the microcontact printed patterns as well (Figure 4.6). The PDMS stamp with a hexagonal structure creates hexagonal APTES patterns, see Figure 4.6A) and

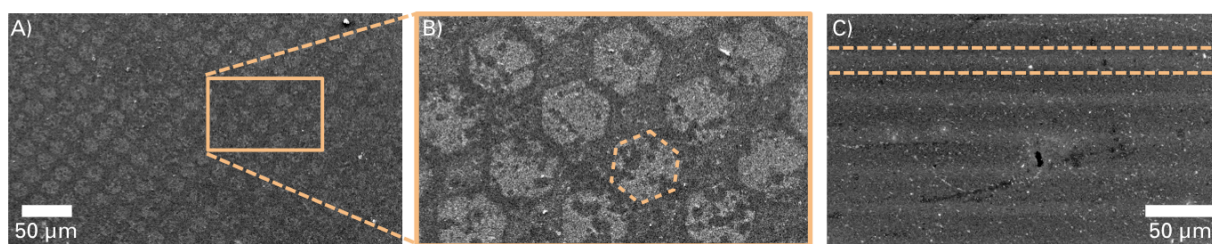


**Figure 4.6.:** AuNP labeling of terminal functional surface groups on oxidized Si wafers after micro-contact printing. Negatively charged AuNPs label protonated APTES surfaces. The dashed lines indicate the extents of the repeated stamp motive. A) Hexagon pattern. B) Magnified detail. C) Stripe pattern.

a magnified detail in B). Many AuNPs attached to the printed and thus functionalized areas as in Figure 4.5A), whereas the control regions in between show less coverage indicated by a darker colour in the SEM image. The AuNP adsorption also reflects the printed stripe pattern, see Figure 4.6C).

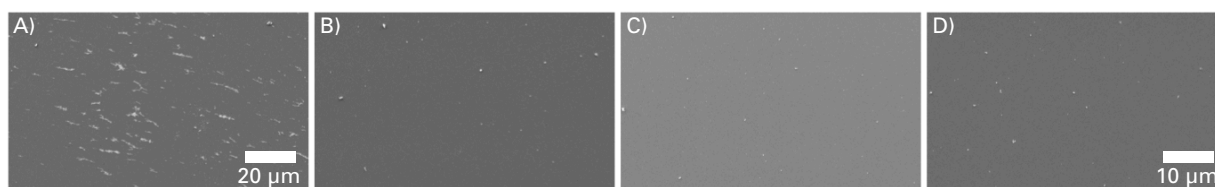


**Figure 4.7.:** SEM images of AuNP labeling of terminal functional surface groups on oxidized Si wafers. A) Amino functionalized NPs label epoxy surfaces. B) Carboxy functionalized NPs do not label the epoxy surface. Incubation with C) amino- and D) carboxy-terminated AuNP solutions on bare surfaces shows almost no NP attachment. Scale bars indicate 10  $\mu\text{m}$  for all 4 samples.

The GOPMS sample shows a certain NP coverage for the covalently attached amino-AuNPs, however it is less dense than on the APTES samples (see Figure 4.7A). This can be due to the ageing of the AuNP solution. It is observable that the AuNPs form small agglomerates which is not the case for the citrate stabilized particles. Thus, the activity is presumably reduced and less surface amines are present. In contrast to the citrate NPs which were commercially bought, the amino-NPs were produced in our lab and were not fresh. In comparison with the controls in Figures 4.7B)-D), the use of carboxy instead of amino functionalized NPs and the attachment onto bare wafers show clear differences. The AuNP coverage in case A) indicates the successful attachment of the epoxysilane and the covalent attachment of primary amines in solution onto the surface. The contrast to the controls B)-D) here is smaller compared to the significant difference for the electrostatically labeled aminosilane, as the amino-AuNPs are not repelled but might be even slightly attracted by the negatively charged bare wafer surface, see Fig. 4.7C). At pH 8.5 however, primary amines protonate less than at pH 7.4 due to their isoelectric point as discussed earlier in this section. To summarize, only the combination of amino-terminated AuNPs with an epoxy-terminated surface leads to a certain AuNP coverage.

### Atomic force microscopy

Atomic force microscopy (AFM) is a helpful tool to characterize the quality of biochemical functionalization layers. For AFM characterization, it is necessary to apply any coating on very flat surfaces as the AFM is highly sensitive to surface topography changes. Thus, wafers are better suited than glass slides. Each functionalization step can be compared to the previous one. Functionalization layers obtained by attachment in the liquid phase (APTES) and via  $\mu$ CP are presented in Figure 4.8. The blank wafer after cleaning shows a flat surface with low roughness, see linescan in Figure 4.8A). The addition of APTES molecules which are covalently attached as well as partially physisorbed leads to an increase in surface roughness, see Figure 4.8B). As the full surface is functionalized at once, direct comparison to a non-functionalized surface (blank) would be of advantage. Thus, APTES was applied onto a wafer surface using  $\mu$ CP of stripe patterns (Figure 4.8C) according to the presented procedure in section 2.1.3. These patterns can be investigated with a special AFM type – the AFAM (Atomic Force Acoustic Microscopy). This technique is well suited for thin molecular layers as it is sensitive to differences in the softness (amplitude signal) [177]. The stripes in this image show monolayer quality and thickness and appear to be relatively homogeneous except for the edges. Here, solution can concentrate during the manual printing procedure. Thus, it is necessary to dry the stamp thoroughly after incubation with the ink to assure an excellent printing of thin layers. The ability of APTES to form nicely arranged monolayers is restricted because of its short length, as discussed previously (see section 1.3.2). The blank control in between the printed stripes however appears flat and clean without much contamination. Apparently, no diffusion of the silane takes place as it was observed for octadecyltrichlorosilane which forms islands on the blank areas [147]. This clear difference will help to distinguish modified and reference surfaces more easily and will support an elevated difference between background and signal.

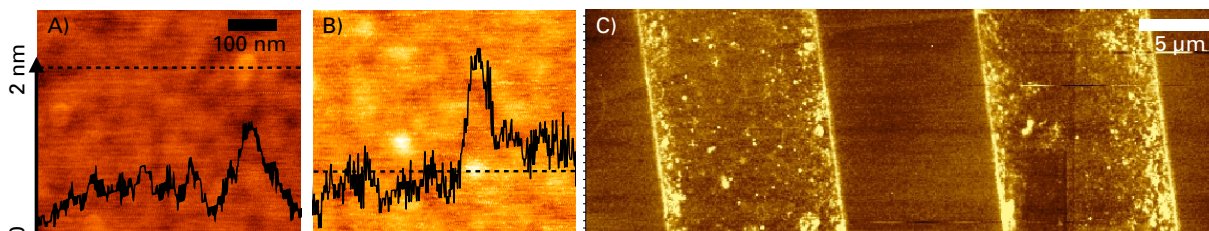


**Figure 4.8.:** AFM characterization of blank wafers (A) and with APTES functionalization from the liquid phase (B) – both topography images with  $z = 3$  nm. The dashed lines indicate the location of the linescans. The linescans themselves are an overlay on top of the AFM image (black lines). The y-axis in A) indicates the scale for the linescan in A) and B). C) AFAM topography image after  $\mu$ CP of APTES with  $z = 1.6$  nm.

A key feature which is characterized with AFM is the increase of surface roughness, represented by the root mean squared (RMS) roughness and the arithmetic average of absolute values ( $R_a$ ). When investigating sprayed or contact printed SiNWs (see section 1.4.2), the development of the NW height which corresponds to the NW diameter is also a possible parameter to evaluate an increase in the layer thickness. For evaluation of the planar surface (RMS and  $R_a$  roughnesses), the same image as

for the NW height analysis (see Figure 4.9, upper image) was used by choosing square windows outside of the NW region. The NW height was determined by a linear cross section perpendicular to the NW length. Each value is the mean of two different samples with each three different analyzed NWs, see Figure 4.9. Here, not only the chemical functionalization steps are presented, but also the receptor binding and the subsequent thrombin detection are analyzed. The bio-attachment is further discussed in section 4.1.1 and thrombin detection is characterized in section 4.1.2.

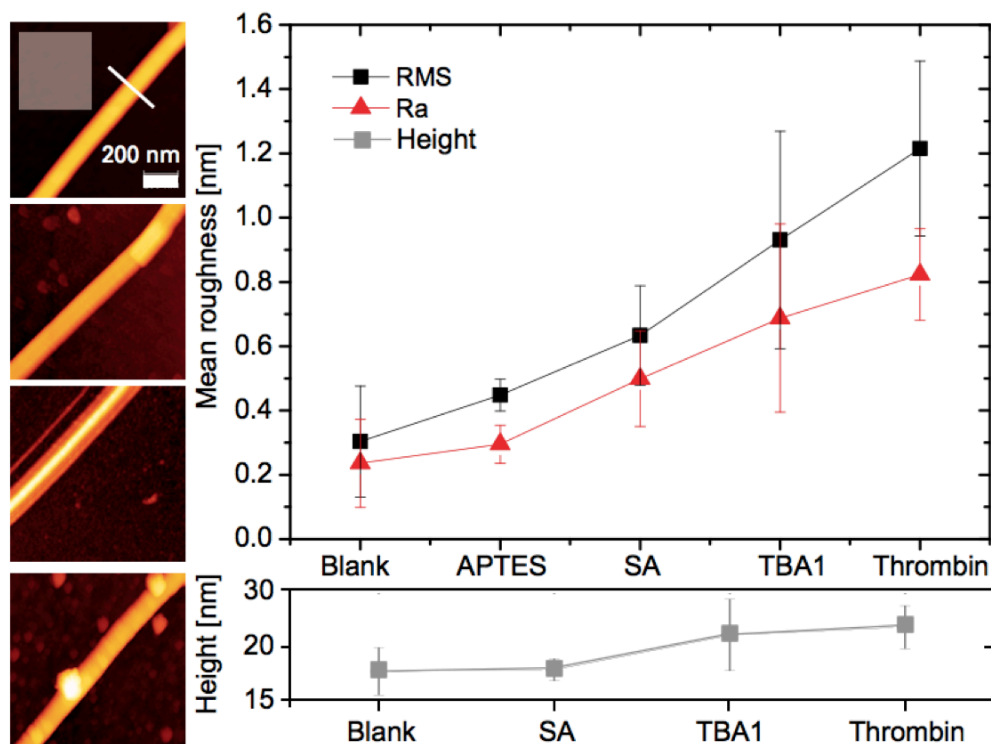


**Figure 4.9.:** The mean RMS and  $R_a$  of planar surfaces and the mean height of NWs increase because of the additional functionalization layers APTES, succinic anhydride (SA), thrombin binding aptamer (TBA1) and thrombin in comparison to the blank and clean surface. AFM topography images of each step are added on the left and correspond to the analyzed steps blank (upper image), SA, TBA1 and thrombin (lowest image). The square area in the upper image (blank) indicates the principal extents and location of the areas used for RMS/ $R_a$  analysis on planar surfaces, the white line how the NW height was determined. The z-scale is 40 nm for all images. The connecting lines in the graphs serve as guides to the eye.

The graph in Figure 4.9 displays both roughness values RMS and  $R_a$ . Both show an increase with each functionalization step which corresponds to the attaching layers. The addition of a bulky protein creates more roughness than the smoother chemical functionalization layer. Below this graph, the height development is presented. Although a tendency towards higher diameters is observable, the increase is quite low and with larger error bars. This can be mainly attributed to variances of the NW diameters themselves. Within one batch, a certain distribution is normal for vapour-liquid-solid (VLS) grown NWs, *e.g.* NWs with a mean diameter of 19.1 nm show a standard deviation of 4.6 nm (see supporting information of Pregl *et al.* [112]) which is in the range of the expected layer thickness

for the modification steps [20]. Between different batches (as it was the case for the here analyzed samples), even larger variations are possible. As roughness characterization on planar surfaces is independent from these findings, it is better suited to indicate layer attachment. However, AFM roughness does not give the degree of specificity of receptor attachment or further biorecognition. AFM is an indispensable technique for microstructure analysis as for the patterned surface and for characterization of the layer homogeneity of chemical layers.

The increase in roughness parameters is more pronounced as it is the case for the height development. This is because of the original height variations of nanowires within one sample, but even more in between different batches. The height increase is more pronounced in case only nanowires of one NW growth substrate are compared (not shown here). The results are less meaningful for an averaging over different batches, as presented in Figure 4.9. The roughness parameters are thus more reliable as they are determined on the planar SiO<sub>2</sub> surface.

### Receptor attachment

Contact angle or ellipsometry are well suited for characterization of the chemical functionalization steps, but the signal change is less pronounced for the immobilization of biomolecules like receptors and targets. Besides characterizing the surface roughness change with AFM, the attachment of DNA strands to a surface via covalent attachment is carried out by using fluorescently labeled strands, in this case with a fluorescein dye to make the DNA visible (TBA1-green see Table 2.1). The protocols for attachment steps can be found in the appendix A. Here, patterning using the nanoplotter or the functionalization of previously patterned samples (via  $\mu$ CP) helps to identify the functionalized regions and to visualize the success of attachment. Figure 4.10 shows the result after carrying out the printing regime. The fluorescence signal of TBA1-green represents well the stripe pattern and shows that DNA is not likely to attach to the blank control surface.

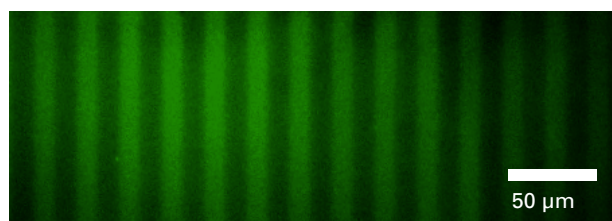


**Figure 4.10.:** Fluorescence image of a carboxylated and activated  $\mu$ CP glass slide after incubation with 20  $\mu$ M TBA1 solution to confirm selective aptamer attachment to functionalized stripe areas.

Patterning using nanoplotting is presented in Figure 4.11. The spots are characterized in 4.11A) and B) in the as-plotted state for two concentrations – 20 and 2  $\mu$ M. After rinsing, loosely absorbed DNA strands are washed from the surface and the spots appear more homogeneously (see Figure 4.11D) and E). Whereas for the higher concentration the spots appear fully functionalized with TBA1 with small density variations, the lower concentration shows a more inhomogeneous coverage, also after rinsing. Thus, 20  $\mu$ M are better suited for further interaction studies. The spot signal in the case of plotting onto clean but unfunctionalized glass slides leads to broad and blurry spots with weak intensity (see

Figure 4.11C). The spots can hardly be distinguished from the background. To conclude, only little unspecific adsorption takes place on bare glass.

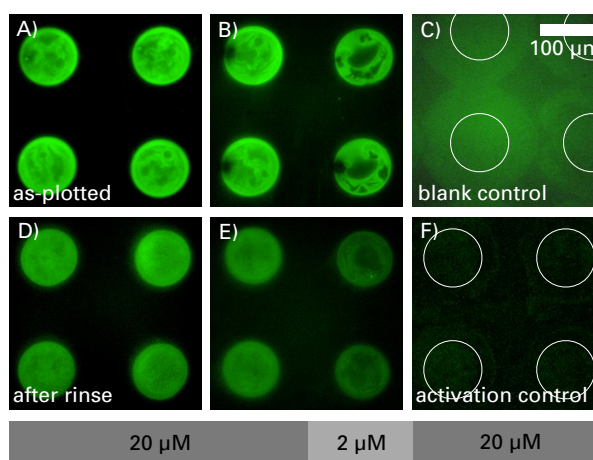


**Figure 4.11.:** Fluorescence microscopy images (20x magnification) to confirm the attachment of fluorescently labeled TBA1 onto functionalized surfaces. The grey bars below the images indicate the plotting of 20 and 2  $\mu\text{M}$  TBA1, respectively. A) and B) Nanoplotting of TBA1 onto activated carboxy functionalized glass slide and imaging in the as-plotted state. C) Nanoplotting onto unfunctionalized blank glass substrate as a control. D) and E) Nanoplotting as in case A) and B). Imaging after rinsing in buffer and water. F) Nanoplotting onto non-activated glass slide after rinsing as a control to D). The illumination time is 1 s except for F) with 3 s because of the low intensity. The scale bar in C) accounts for all images. White circles in C) and F) indicate the extents of spots in A).

In order to confirm the activation using zero-length crosslinkers EDC and NHS, nanoplotting was performed in two ways, with (D) and without (F) activation (see section 2.1.2). Without EDC/NHS, almost no spots are observable after rinsing in buffer and water, even with an illumination time of 3 instead of 1 s as for the other samples as presented in Figure 4.11. The sharp and bright spots on the activated slide (Figure 4.11D) however indicate a successful attachment in case the EDC/NHS activation was successful. From other applications like DNA combing, it is known that positively charged amino surfaces (charged because of protonation) attract DNA which is negatively charged [178]. In case the carboxylation step has not been successful, the green DNA would also attach to the functionalized stripes or would form nice spots on the fully functionalized surface only because of electrostatic interactions. Comparison of the spot size and appearance to spots directly plotted on APTES slides (not shown here) also confirmed a difference in the spot diameter. The APTES diameter is smaller because of the higher contact angle on aminosilane surface with respect to carboxy surfaces (see section 4.1.1). This finding also allows to confirm the carboxylation after nanoplotting.

### 4.1.2. Receptor-analyte interaction

#### Quartz-crystal microbalance with dissipation monitoring

The quartz-crystal microbalance with dissipation monitoring (QCM-D) was introduced to probe the interaction of immobilized TBA1 with thrombin. By using QCM-D chips coated with a thin layer of SiO<sub>2</sub>, the success of the attachment protocols for TBA1 and its specific interaction with thrombin can be studied in a flow cell setup (see section 2.5.2). In order to investigate the effect of blocking and the unspecific adsorption, not only thrombin was pumped over the sensor crystal but also bovine serum albumin (BSA) as a blocking protein.

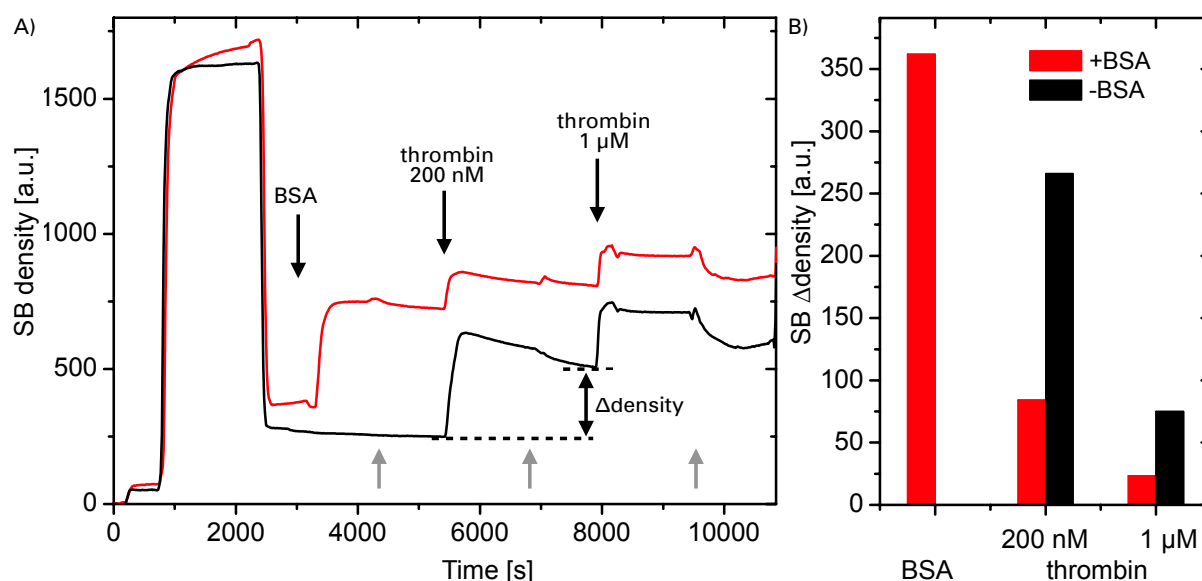


**Figure 4.12.:** Sauerbrey (SB) density analyzed for two chips run in parallel to compare the effect of BSA blocking and to find the upper limit of protein detection for fluorescence microarray thrombin detection. Red indicates with, black without BSA blocking. A) Sauerbrey density is plotted over time. Black arrows show the start of protein pumping, grey arrows where buffer is used to rinse. B) Density change comparing the value before injection and after rinsing as indicated in A) by dashed lines.

In Figure 4.12A), the density calculated after Sauerbrey using the QSense software QTools is presented in dependency of the time. Small black arrows indicate the moment a new solution is pumped over the surface. Grey arrows show when buffer was pumped for rinsing purposes. The signal of a layer is calculated from the difference before injection and after rinsing as it is assumed that by rinsing at 50  $\mu\text{l}/\text{min}$ , the loosely attached molecules are removed from the surface. Two systems were measured in parallel – thrombin detection by surface bound aptamers with and without previous BSA blocking. Prior to installing the chips in the QCM-D, they were functionalized with chemical molecules and TBA1 as described previously (see section 2.1.2). Without rinsing TBA1, the chip was mounted onto the chip holder and tightly sealed. Unbound DNA was then washed away by pumping degassed



water. This was followed by 1 M Tris buffer for blocking unreacted carboxy groups and incubation in thrombin binding buffer (see appendix A.2). Biological blocking using a 0.5 mg/ml BSA solution in the same buffer was carried out for chip 1 (red), but not for the second one (black). BSA was pumped for 6 min and then left to incubate for 10 min. Chip 2 went through the same regime but with a BSA-free buffer. After incubation, the samples were rinsed. Thrombin was firstly injected at a concentration of 200 nM. After fully covering the sensor surface with thrombin solution, the samples were left to interact for 20 min. This was also followed by a buffer rinse. To see where the upper limit of detection is, *i.e.* at which concentrations the device is fully covered with thrombin, an even higher concentration of 1  $\mu$ M was injected. The graphs in Figure 4.12A) firstly show that a distinct amount of thrombin is unspecifically attaching if no BSA is present to block. With a thrombin concentration of 200 nM, the signal increases further and decreases by half of its height after rinsing. This removes loosely attached protein molecules. The presence of the high thrombin concentration does not lead to a significant density increase indicating that the surface is almost saturated with thrombin, *i.e.* that most binding sites are occupied. Figure 4.12B) compares the density changes after each step (after rinsing) indicating on one side a need for blocking the unspecific attachment sites and secondly the saturation of the device at concentrations above 200 nM [163]. The analysis using Voigt model gives a similar trend. As with Sauerbrey averaging between three overtones (3, 5 and 7) for a mean value is easily possible using the software QTools, the Sauerbrey calculation was used instead of Voigt.

### Electromobility shift assay with native polyacrylamide gel

Gelectrophoresis allows to analyze molecular recognition in solution. In Figure 4.13 the migration of thrombin in the gel towards the plus pole was compared to the behaviour of aptamer-thrombin complexes. The same amount of molecules (*i.e.* 50 pmol) was mixed in separate vials. Interaction was allowed for 30 min which is similar to the incubation time on substrates. The samples were loaded onto the gel. This was followed by applying the voltage to induce travelling of the charged molecules. The gel was stained using protein staining agent coomassie blue. DNA strands are not affected by it. At pH 8.5, the charge of thrombin is close to neutral with an isoelectric point of 7.0-7.6 [155]. Above the isoelectric point, thrombin is supposed to get negatively charged (see also [3]) and a migration towards the plus pole is expected. Negatively charged DNA will migrate through the gel towards the positive charge end. Thrombin in lane 1 however did not migrate, but the complex with TBA1 in lane 2 reached approximately half of the depicted distance due to the negative charges. The TBA2-thrombin complex traveled slightly faster. The interaction yield seems to be lower for thrombin-TBA2 than for thrombin-TBA1 as more unbound thrombin remains at the beginning of the lane. The complex involving all three components in lane 4 migrated the longest distance.

This analysis proves the presence of three active components in solution which participated in the sandwich later investigated on the inorganic surface of glass slides in microarrays. The finding that thrombin alone did not migrate at all indicates that the negative charge is small at pH 8.5. The differences in distance between the different complexes can be attributed to the different aptamer lengths. As TBA2 is longer and thus possesses more negative charges than TBA1, the complex

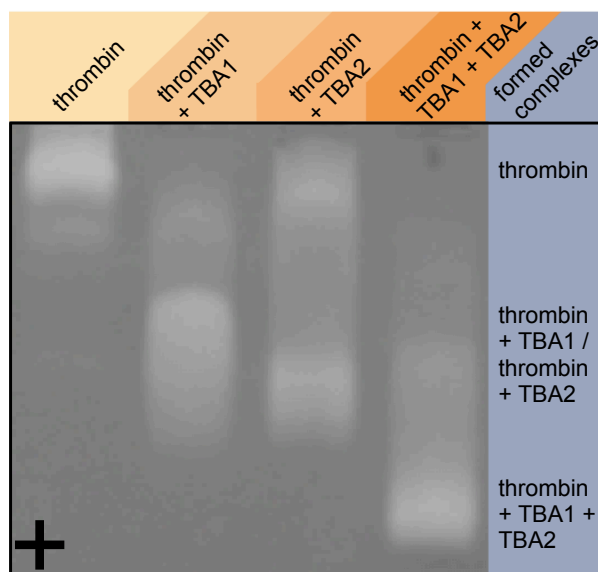


**Figure 4.13.:** Native PAGE of 8 % to investigate the interaction of protein thrombin with TBA1 and TBA2 in 25 mM Tris glycine buffer of pH 8.5. Lane 1 is thrombin alone, lane 2 and 3 show the migration of the complex formed by thrombin with one of the aptamers, lane 4 the interaction of both aptamers with the protein. Right to the gel image, probable complex formations are indicated.

migrates a wider distance. As the size of the TBAs is small compared to the size of thrombin, mainly the change in charges per complex influences the migration distance. Thus, the complex with all three components involved results in the longest distance. Obviously, this techniques helps to distinguish thrombin in complex formation with different aptamers as well as unbound thrombin.

### DNA microarray for thrombin sensing

**Optimization of sandwich assay** The concept for thrombin sensing using aptamers can be found in section 3.1.2. Parts of the following results were already published in 2013 [163]. In order to test different concentrations of thrombin in this microarray based sandwich assay, the concentrations of TBA1 (capture layer) and TBA2-red (labels thrombin regions) were optimized to obtain a wide detection range and a low limit of detection. Based on literature review [138, 167], two TBA1 concentrations were chosen – 2 and 20  $\mu\text{M}$ . For TBA2-red, 200 nM were selected according to Meneghello *et al.* [167]. A high thrombin concentration of 200 nM allows for a good signal. All sandwich layers were applied to the glass slides according to the protocols in the appendix A.4.

In Figure 4.14B) and C) both TBA1 spot densities were compared at these fixed thrombin and TBA2-red values. The fluorescence-to-background amplification ratio (F2B) of B) results in only 1.06 whereas C) gives 1.17. Using the higher concentration for the capture layer TBA1 will allow to go for lower thrombin concentrations as 200 nM already represent the region of the upper detection limit as determined with QCM-D (see section 4.1.2).

In a second study, the influence of BSA blocking on the F2B value was investigated. Samples with both arrays, 2 and 20  $\mu\text{M}$  TBA1, were incubated with thrombin and TBA2-red without (D) and with

(E) BSA blocking. The corresponding F2B values are 1.10 and 1.17 for 20  $\mu\text{M}$  TBA1 (corresponding to the right spot column in both images). In addition to QCM-D sensing, this shows the importance of blocking the microarrays prior to thrombin detection to avoid unspecific attachment. BSA blocking significantly enhances the F2B value and the F2B difference of separate concentrations. This indicates a working blocking method and allows to detect a wider range of thrombin in solution.

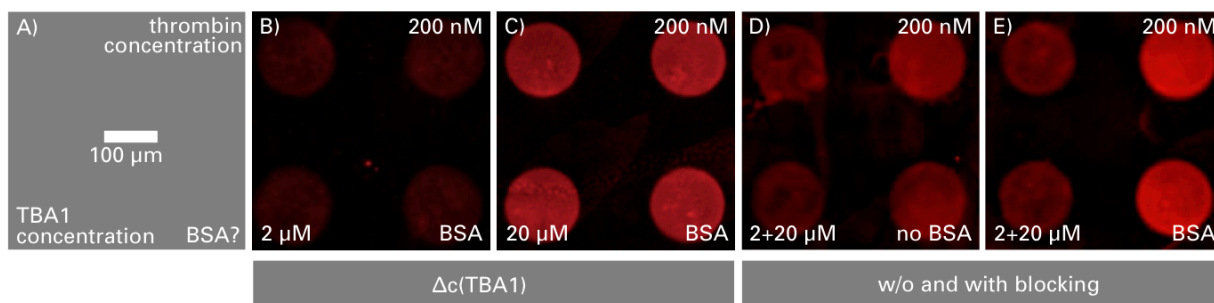


**Figure 4.14.:** Fluorescence microscopy images of sandwich assay on nanoplotted TBA1 spots for optimization of TBA1 concentration (B and C) and to show the blocking influence (D and E). A) The used thrombin concentration is indicated on the upper right, the TBA1 concentration on the lower left and whether BSA blocking was implemented or not can be found on the lower right. The scale bar is valid for all images B) to E). B) Detection of 200 nM thrombin with nanoplotted TBA1 spots of 2  $\mu\text{M}$  concentration. C) Like B) with 20  $\mu\text{M}$ . TBA1 spots of both concentrations detect 200 nM thrombin without (D) and with (E) BSA blocking.

By replacing the immobilized receptor with a scrambled DNA sequence (SCR, see table 2.1), the specificity of thrombin towards TBA1 was investigated. Figure 4.15A) shows irregularly shaped spots with blurry and weak fluorescence intensity, clearly different from the results obtained with the aptamer TBA1 for 200 nM thrombin in buffer. Besides the other characterization methods, this confirms the specific interaction of thrombin with the surface-bound receptor TBA1. As a protein control, the growth factor TGF- $\beta$ 1 was used to replace thrombin in the sandwich assay on nanoplotted TBA1 at a concentration of 39.1 nM, diluted from the 3.91  $\mu\text{M}$  stock solution. The extents of spots in Figure 4.15B) are highlighted by white circles. The spot area appears to be even darker than the surrounding BSA-blocked area. This may be attributed to the higher overall negative charge within the spots because of the attached DNA strands which probably repel the approaching TBA2-red strands more than the reference area.

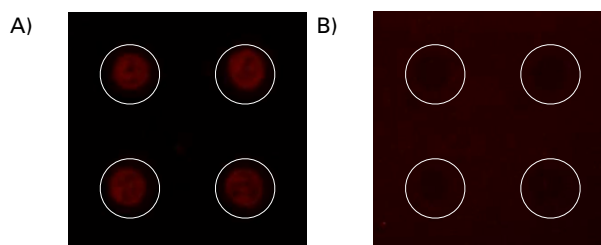


**Figure 4.15.:** Fluorescence microscopy images of sandwich assay. The white circle lines label the extents of the nanoplotted spots. A) Control DNA with scrambled sequence (SCR) as capture layer. B) Protein control TGF- $\beta$ 1.

The same setup was not only carried out on patterned slides using nanoplotting of TBA1, but also on slides functionalized via microcontact printing in the first place. This setup was also used to confirm the success of the sandwich assay, *i.e.* that the same regions that were functionalized with TBA1-green are labeled by TBA2-red after dual thrombin recognition by both aptamers subsequently. Figure 4.16A) and B) are images of the same sample spot after all steps of the sandwich assay detecting 200 nM thrombin. The small contamination (bright spot) in the upper image part confirms that the same area is investigated. Image A) was taken with the filter set 10 to visualize green fluorescence of TBA1-green and for B) filter set 15 was applied to see only red fluorescence. As TBA1-green went through all washing steps and is covered with the additional layers of thrombin and TBA2-red, an illumination time of 3 s instead of 1 s was necessary for imaging and the signal appears more blurry. However, a clear difference between functionalized stripe and blank control areas is observable and helps to identify the dual recognition of thrombin by both aptamers.

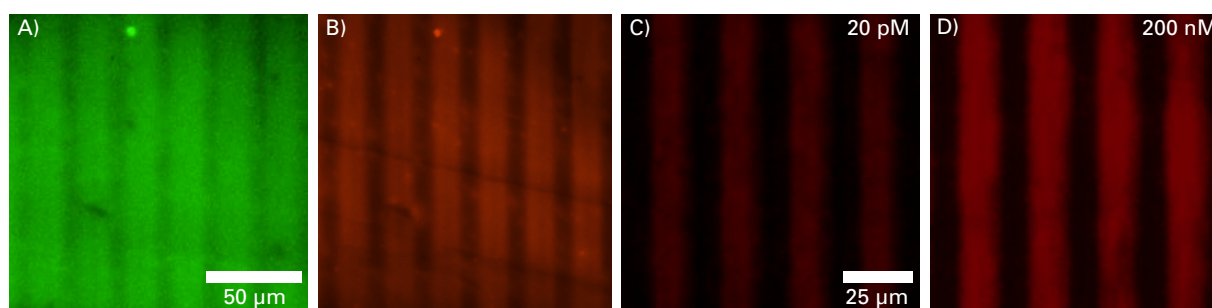


**Figure 4.16.:** Fluorescence microscopy of aptamer attachment and thrombin detection in sandwich assay onto microcontact printed glass slides. A) Green fluorescence of TBA1 with FAM label to illustrate the potential attachment sites of thrombin. The image was taken after carrying out the sandwich assay. The washing steps and additional layers on top lead to a blurry stripe signal. The scale bar is valid for A) and B). B) shows the same spot as A) but imaged with the filter set 15 for red fluorescence of TBA2 labeling the thrombin areas (200 nM thrombin). A) and B) confirm the sandwich assay. C) Detection of 20 pM thrombin in sandwich assay with unlabeled TBA1. The scale bar is valid for C) and D). D) Detection of 200 nM thrombin in sandwich assay with unlabeled TBA1.

**Detection of different thrombin concentrations** After optimizing the concentrations of the involved biorecognition layers, different thrombin concentrations from 200 nM down to 20 pM were tested on  $\mu$ CP (200 nM, 2 nM, 20 pM) and nanoplotted samples (200 nM, 150 nM, 100 nM, 60 nM, 50 nM, 2 nM, 20 pM). Figure 4.16C) and D) exemplarily display the stripes of 20 pM and 200 nM thrombin recognition. Figure 4.17A)-E) illustrates 5 of the investigated concentrations from 20 pM to 200 nM of the nanoplotted samples. All selected images were analyzed according to the described method in section 2.4.5 to obtain fluorescence-to-background amplification ratios (F2B). The corresponding calibration curve of the analyzed F2B values is presented in Figure 4.18 for both patterning routes (nanoplotting = red,  $\mu$ CP = black) with the thrombin concentration in logarithmic scale.

For both methods, a distinct signal is observable at the lowest concentration, *i.e.* 20 pM. Taking a closer look at the curve for the nanoplotted samples (red circles), the fluorescence increase for

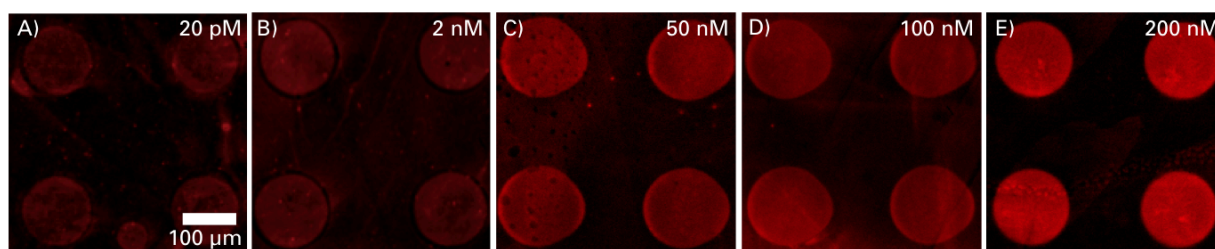


**Figure 4.17.:** Series of fluorescence microscopy images from 20 pM (A) to 200 nM (E) thrombin concentration in sandwich assay on nanoplotted TBA1 spots in a microarray.

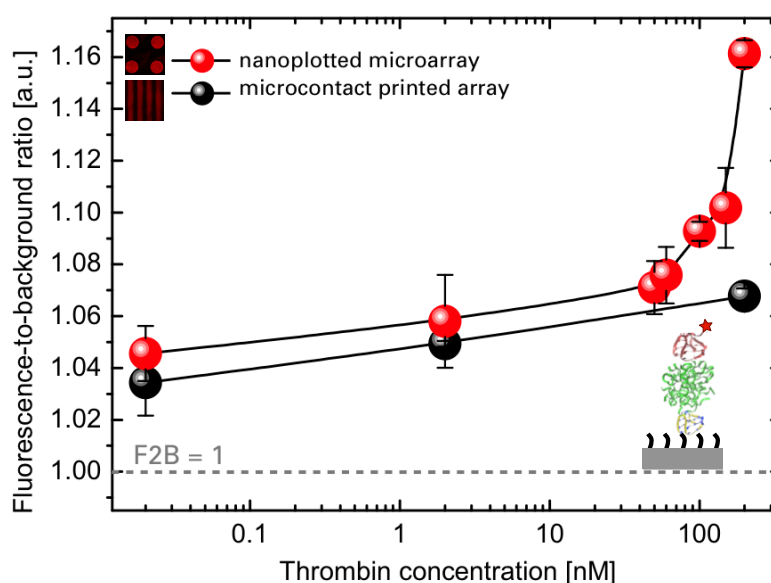


**Figure 4.18.:** Calibration curve of the F2B value versus the thrombin concentration in semi-log scale for surface-patterned samples ( $\mu$ CP in black and nanoplotted in red). The lines in between the data points serve as guides to the eye.

subnanomolar thrombin concentrations is small compared to the steeper slope towards 200 nM. The sensing setup presumably approaches a saturation level above 200 nM for a capture layer of 20  $\mu$ M TBA1 when comparing this method to other similar works employing optical detection [97] or the results obtained with QCM-D (see section 4.1.2). This means that higher concentrations might not be distinguishable by this setup. Derived from the results presented in Figure 4.14 probing the F2B of two different TBA1 densities, detection of higher thrombin levels would be possible to a certain extent by tuning the capture layer density within the spots to values different from 20  $\mu$ M. Concerning the lower limit of detection, subnanomolar levels are detectable with the here presented setup at least down to 20 pM. This is an improved detection limit compared to Menghello *et al.* who recently reported a detection limit of 250 pM in a similar optical sandwich assay [167] and the clear signals for 20 pM here may allow for detection of even lower concentrations. Comparing this assay to other optical sandwich assays, Niu *et al.* could detect thrombin at a concentration of 0.43 pM in a AuNP based fluorescence

sandwich assay [179], whereas other techniques such as fluorescence or electroluminescence involving quantum dots or beads achieved limits ranging from hundreds of pM [180] up to nM [181, 182] values. Relevant signal ranges for detection purposes are summarized in section 2.2.1. To discuss the sensor performance in more complex or real samples, Meneghello *et al.* and Zhao *et al.* probed their sandwich assays (fluorescence microarray and AuNPs, respectively) with serum samples, spiked with different thrombin concentrations. Serum is a complex matrix with different proteins and molecules and is often used to approach the characteristics of real blood samples. They could both show a decrease in the sensor performance with pure serum or little dilution. When diluting the serum by 5-10x, its influence was however small to negligible. A similar degradation can be expected for the here presented assay. But as this magnitude of dilution is handled easily, this effect can be overcome in practice.

The F2B values of the  $\mu$ CP samples were equally analyzed for three concentrations. The slope of the curve (black circles) is less steep than it is the case for NP samples. This can be attributed to the small stripe width. Although AFAM analysis shows a clean flat reference area in between the stripes (see section 4.1.1) one has to consider that the printing was carried out manually and sample-to-sample variations may occur. So it is possible that the applied pressure during printing varied locally and that silane diffused onto the bare regions and was further functionalized, as it was described by Jeon *et al.* [147]. Thus, the ratio between signal area and reference surface, *i.e.* the F2B value, is lowered. Most importantly, the detection limit of 20 pM is also achievable with the patterning technique implementing  $\mu$ CP of the first functionalization step with silanes which allows to control the functionalization from the start.

During the past section, a variety of tools was presented to verify each functionalization step for aptamer attachment and subsequent thrombin recognition. The techniques can be further used for aptasensor development on SiO<sub>2</sub> surfaces like glass slides or silicon-based electronic sensing as presented in the next chapter on SiNW FET based sensing in section 5.1. By having introduced a sandwich setup with two different aptamers, the dual recognition allows for high specificity of the optical detection assay. Such sandwich assays are usually limited by either the required presence of two recognition sites on the surface of the analyte molecule for one receptor or the existence of two receptors for two different recognition sites.

## 4.2. Amoxicillin detection

### 4.2.1. Biochemical functionalization

The attachment strategy for amoxicillin (AMX) detection was presented in section 3.2. Functionalization of silica surfaces with GOPMS has been proven and characterized previously (see section 4.1) using contact angle measurements, ellipsometry and AuNP labeling. Via the terminal epoxy groups, AMX is linked to the surfaces (see section 3.2). In addition, the change of surface potential after molecule attachment is demonstrated using FET measurements as presented in the next chapter (see section 5.2.2) which also allows for immediate control of the experimental setup on the chip.

### 4.2.2. Receptor-analyte interaction

Following the inverse competition assay presented in section 3.2.1, SiO<sub>2</sub> surfaces (wafer, chip) were functionalized with epoxy silane GOPMS via gas phase attachment in an oven overnight (protocol see A.1). Amoxicillin attachment via the surface epoxy group to its primary amine was carried out in 10 mM PBS buffer (= 1x PBS) for 30 min, tuned to a higher pH ranging from 8.5-8.9 using 1 M NaOH. Typical AMX concentrations were 100 µg/ml to assure a full coverage. This AMX is called surface-AMX in the setup (see section 3.2.1).

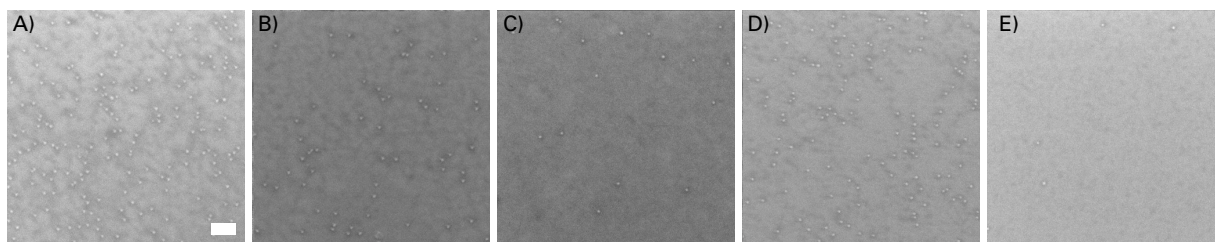


**Figure 4.19.:** Immunogold labeling with anti-mouse secondary antibody onto different anti-AMX antibody concentrations and controls. A) Antibody dilution of 1:500 in inverse assay. B) Antibody dilution of 1:2000 in inverse assay. C) Antibody dilution of 1:500 and preincubation with sample-AMX (200 µM) in competition assay. D) Like A) but without surface-AMX. E) Inverse assay without anti-AMX antibody. Scale bar in A) accounts for all images and equals 100 nm.

In order to verify the specificity of the assay, AuNP labeling with secondary antibodies was carried out (see Figure 3.2A). Two different anti-AMX antibody dilutions were tested (1:500 and 1:2000 in 0.01x PBS buffer of pH 7.4) to see whether the concentrations are reflected by a different AuNP density, see SEM images in Figure 4.19 A) and B) with 175 and 63 AuNPs on the presented images, respectively. The decreasing particle coverage reflects the different antibody concentrations which were applied onto the surfaces in A) and B). Image C) is an example of the inverse competition assay (see concept in Figure 3.2B) with a sample-AMX concentration of 72.5 µg/ml and an antibody dilution 1:500 from the stock. With only 20 AuNPs, this sample shows a significantly lower particle density than A) and B). As a high sample-AMX concentration is expected to 'catch' most of the antibodies in solution, only a little amount of antibodies remains free for interaction with the surface-AMX. D) and E) represent control samples with 140 and 4 AuNPs, respectively. To the sample in D), no surface-AMX was attached and so the anti-AMX antibody could directly adsorb onto the epoxysilane surface. As this is less hydrophilic, proteins tend to adsorb more onto it which leads to unspecific adsorption of the antibody. They are then labeled by the secondary antibody. In addition, the secondary antibody might also attach to the surface by unspecific adsorption due to the lower hydrophilicity of epoxy groups. The sample presented in E) was not incubated with the anti-AMX antibody after AMX attachment. As the surface is more hydrophilic after AMX attachment than after GOPMS attachment, the secondary antibody does not adsorb notably. The low attraction of the secondary antibody by a hydrophilic surface was also confirmed by Rim *et al.* on bare surfaces [4].

To summarize, the immunogold particle densities in Figure 4.19A) and B) reflect the different anti-AMX antibody concentrations. The antibodies attach in a relatively high number to the GOPMS functionalized surface which acts as a control, possibly due to hydrophobic-hydrophobic interactions, *i.e.* unspecific interactions. The SEM study also shows that the secondary antibodies are only weakly attracted by the AMX surface indicating a distinct change in the surface chemistry. From this, it is possible to conclude that little unspecific adsorption of protein-like molecules is happening on AMX-functionalized surfaces. Secondary antibodies are thus only attaching in case anti-AMX antibodies are present. Unspecific adsorption could be reduced by adding rinsing steps or additional blocking as described previously. In the case of sample C), less antibodies are available to recognize the surface-AMX as they already detected the sample-AMX in solution. This is then reflected by the lower AuNP density compared to A) and B). The secondary antibody only labels anti-AMX antibodies that are attached to the surface. These results allow to proceed with FET sensing of anti-AMX antibodies for an indirect AMX sensing, see section 5.2.

### 4.3. Nanowires as tools

#### 4.3.1. Zeta potential

Zeta potential ( $\zeta$ -potential) technique enables to measure the changes in the surface charge of micro- and nanoparticles due to functionalization, ideally carried out with particles of circular shape. Although nanowires exhibit a high aspect ratio, it was possible to obtain the  $\zeta$ -potential. The particle size, determined via dynamic light scattering (DLS) is averaging between the long length ( $\mu\text{m}$ ) and the tiny diameter (nm) which results in a mean particle size of roughly 500 nm which does not reflect the real dimensions of the nanowires. However, this value may be used to indicate agglomeration of the particles in solution. To exclude agglomeration and to increase comparability, the solutions were only sonicated right before measurement with a time difference of around 1 h until measured.

Nanowire growth substrates, obtained from bottom-up nanowire growth, were cleaned in organic solvents, hydroxylated, silanized and carboxylated according to the previously described methods, see section 4.1.1. Usually, the substrates are sonicated in organic solvents where the SiNWs do not agglomerate with time. The integration of NWs from these solutions is discussed in section 1.4.2. In order to verify the modification procedures or to use it for combinations of biological self-assembly with one-dimensional nanomaterials, see next paragraph (section 4.3.2), the dispersion of nanowires in aqueous solution is a prerequisite. The goal here is also to obtain stable solution in water or buffer by using the repulsive forces caused by electrostatic interactions. As the functionalization steps create surface charges like protonated amines in dependency of the solution pH, the solutions are expected to remain stable at least initially after sonication.

During modification of the nanowires which are still immobilized on the substrate, it is important to replace any cleaning step which involves ultrasound by a different method. By this it is possible to keep the wires fixed until final sonication. After functionalization, each growth substrate piece (size appr.  $0.8 \times 1.5 \text{ cm}^2$ ) is sonicated in 1 ml of deionized water for 2-3 min. The measured pH of the



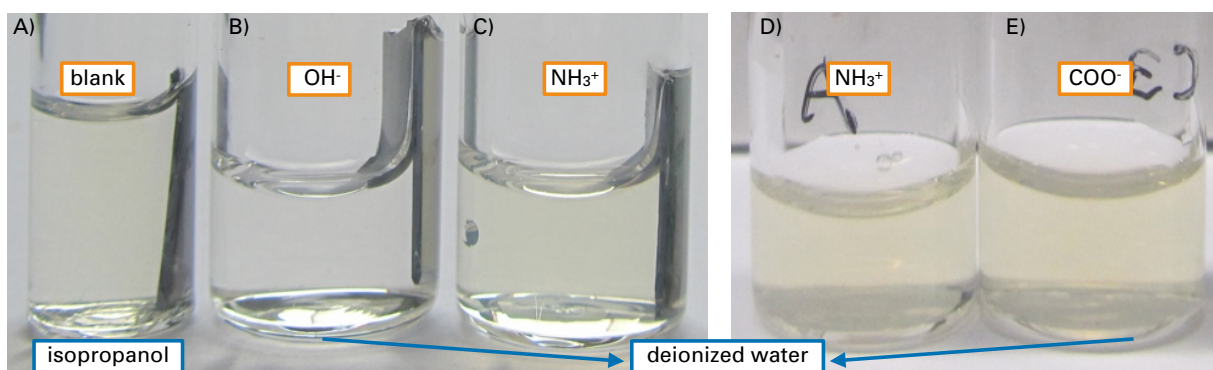


**Figure 4.20.:** Nanowire solutions in A) isopropanol and B)-E) deionized water with different terminal surface groups due to surface functionalization which alters the colour change from transparent to yellowish due to the NW dispersion yield. The growth substrates are visible in the small glass tubes in samples A)-C) on the right side. The colour difference between C) and D) is only due to external illumination conditions.

used dI water was around 5.8 to 6. Well dispersed solutions show a colour change to yellow like it is the case for organic solvents. Figure 4.20 compares the different solutions after sonication of blank substrates in A) isopropanol and B) dI water. C) and D) show the APTES-coated wires and E) with terminal carboxy group, all in dI water. For all different five solutions a colour change to yellow is observable. The best dispersion is achieved in organic solvents, but APTES and carboxy solutions show also a distinct colour similar to A). The hydroxylated wires however are not well dispersed with a slighter colour change. For blank wires, surface  $\text{OH}^-$  are responsible for electrostatic interactions between the wires. At the pH of dI water, APTES is protonated and exhibits positive surface groups ( $\text{NH}_3^+$ ). The terminal carboxy groups are partially dissociated to  $\text{COO}^-$  and thus expected to be negatively charged.

The  $\zeta$ -potential of the individual solution was determined. Each modification step is the mean value from three separate samples. The results are presented in Figure 4.21. The black squares represent the experimental results whereas the other data points originate from references. The blank and carboxy surface possess negative values of  $-32.99$  mV and  $-30.07$  mV, respectively. APTES attachment however leads to a positive surface zeta potential of  $23.2$  mV. The signs of the individual zeta potentials confirm the success of binding organic molecules to the surface. Feifel and Lisdat carried out  $\zeta$ -potential measurements on ideally shaped silica particles with a similar result but higher absolute values ( $-41.44$  mV for bare,  $-54.71$  mV for carboxy and  $39.63$  mV for APTES coated NWS in dI water), see orange circles in Figure 4.21 [183]. Graf *et al.* characterized aminosilanized silica particles in dI water with a pH of 6.5 and in ethanol (both triangles) [184]. They measured 16 and 64 mV, respectively. The lower values compared to Feifel and Lisdat can be attributed firstly to the high aspect ratio of nanowires, which is not optimal for this zeta potential technique. Secondly, the nanowires are lying on the substrate during functionalization. It is possible that the surface is not fully functionalized but shows inhomogeneous areas with lower molecule density. Additionally, it is not specified which solvent the particles are dispersed in for zeta potential measurements. Graf *et al.*

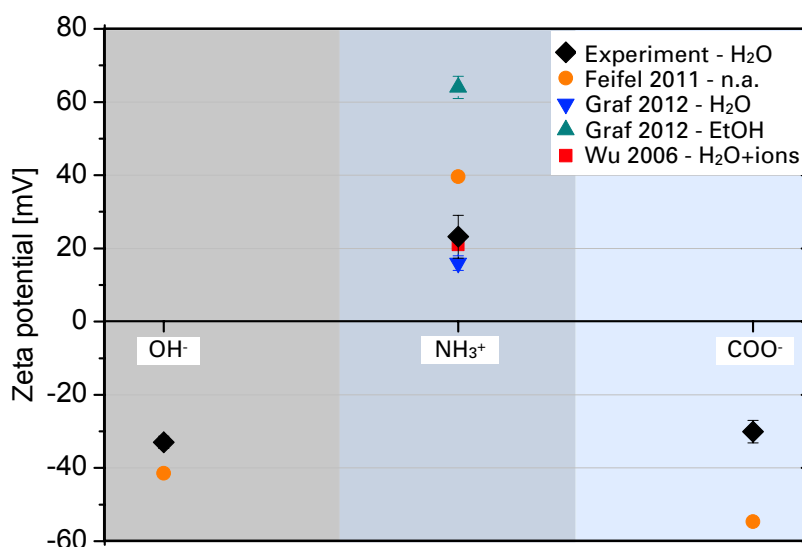


**Figure 4.21.:** Zeta potential values of the functionalized nanowires in dI water (black squares) in comparison to literature values of functionalized silica particles from Feifel and Lisdat (orange circle), Graf *et al.* (both triangles) and Wu *et al.* (red square) in both dI water and ethanol as indicated [176, 183, 184].

possibly measured a lower  $\zeta$ -potential as the pH of our water was lower than in their case [184]. The effect of pH on aminosilanized silica particles was studied by Wu *et al.* [176] and they measured a  $\zeta$ -potential of around 12 mV at pH 6.5 and around 21 mV at pH 5.5-6 which corresponds well with the value presented from Graf *et al.* and the results with nanowires.

To conclude, the zeta potential of functionalized NWs reflects the different functionalization steps and agrees well with literature values. Differences can be attributed to a different molecule density and possibly the non-ideal shape of NWs with high aspect ratios compared to circular silica particles. This technique is a rapid method to verify applied functionalization steps in a reproducible manner and supplements the methods presented in section 4.1.1.

#### 4.3.2. Nanowires with lipid bilayer shells

The results in the following section were published together with A. Gang in 2013 [84] with the aim to show the coating of SiNWs in aqueous solution with a lipid bilayer shell. The implementation of lipid bilayers is an option to functionalize surfaces for biological applications in a non-covalent way, see section 1.3.1. Lipid bilayers have been widely demonstrated on planar surfaces, but are also well-suited to coat nanomaterials like nanowires or CNTs with their small curvature. By this, one-dimensional (1D) structures are formed.

One-dimensional structures of lipid bilayers have been reported by Kulkarni *et al.* [185] using specially designed combinations of lipids that form cylindrical tube-like structures without the support of a template. The group of Noy *et al.* [94] presented a protocol to completely wrap polymer coated CNTs dispersed on a TEM grid with a functional lipid bilayer. A similar protocol was ap-

plied to polysilicon nanowires which were also dispersed on a TEM grid before lipid bilayer coating [95]. However, bottom-up ways of integration of nanowires or nanotubes into devices are still a challenge [122, 186]. The combination of the self-assembly properties of biological material together with nanoparticles can lead to controlled deposition of these nanoparticles [187], *e.g.* on bacterial S-layer templates [188].

Despite a large number of reports on the formation of lipid bilayer coatings and even their interactions with silicon nanowires, the formation of highly concentrated aqueous solutions containing suspended nanowires wrapped by lipid films has not been demonstrated so far. At the same time it should be stressed that solutions containing such functional nanowires are of special interest for the wide range of biotechnological applications, from drug delivery purposes to multiparallel sensor arrays.

In the following, a reproducible strategy on how to obtain SiNWs dispersed in an aqueous solution as carriers of one-dimensional lipid bilayers is presented. This strategy is carried out by combining a SiNW suspension stabilized by surface functionalization of the SiNWs as suggested by Heo *et al.* [186] with a common lipid bilayer deposition approach. The parameters to form lipid bilayers on planar surfaces were tested first (see Figure 4.23A), left image). The findings were then transferred to a protocol for LB formation onto the curved surface of SiNWs (see Figure 4.23A), right image). The optimal pH range was determined via zeta potential measurements. Dynamics of the lipid films were investigated using the fluorescence recovery after photobleaching (FRAP) technique. In situ observations of lipid exchanges between a vesicle and the bilayer coating of a SiNW demonstrate that SiNWs are suitable templates. The obtained 1D lipid bilayer structures could be used as drug delivery agents or they might be integrated into devices as actuator elements in bionanosensors based on SiNWs.

Usually, the NW growth substrates are sonicated in organic solvents where the SiNWs do not agglomerate with time [95, 111]. In order to create a bilayer shell around the nanowire, however, use of an aqueous solution is necessary. Heo *et al.* [186] demonstrated that SiNWs functionalized with APTES remain stable in dI water by electrostatic repulsion due to the protonation of the primary amine surface group, see previous section 4.3.1.

As illustrated in Figure 4.22, APTES-SiNWs have  $\zeta$ -potential values of 19–22 mV at pH 5.8–6.0. According to Wu *et al.* [176], silica particles with APTES coating show an isoelectric point at approximately pH 9, whereas at pH 5 the  $\zeta$ -potential is 20–22 mV. The nanowire characteristics are thus in perfect agreement with the data from Wu *et al.* for the selected pH range (see appendix A.6) to create lipid bilayers in acetate buffer with pH 5 (see grey bar in Figure 4.22), also indicating the successful surface modification with APTES. The determined isoelectric point for APTES coated SiNWs with 6.5 is however lower. The discrepancy might be due to the high aspect ratio of nanowires not corresponding to the fully spherical model assumed in  $\zeta$ -potential calculation. In addition, the APTES density might influence the shift.

The VLS grown SiNWs were characterized by AFM and further characteristics can be found in the publication of Pregl *et al.* [112]. The length of the wires was in the range of 1–10  $\mu\text{m}$  after

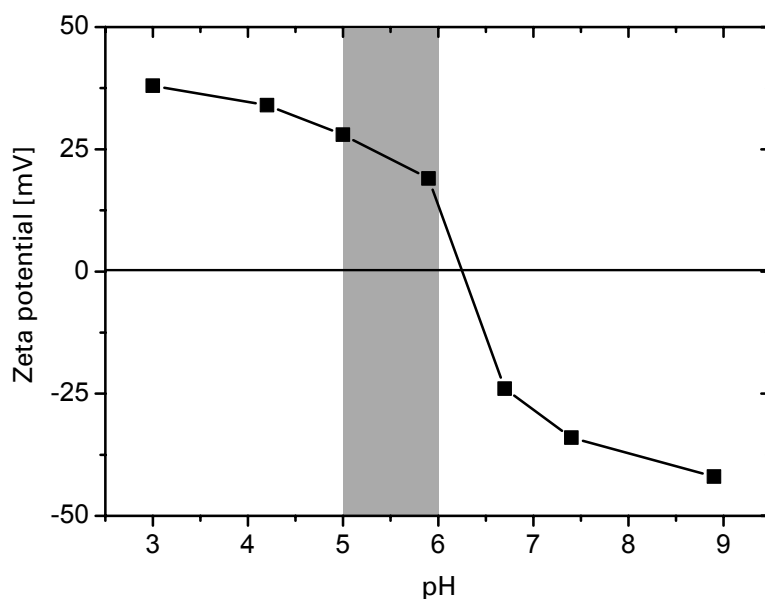


**Figure 4.22.:** Zeta potential for APTES coated SiNWs in dI water, tuned to different pH values by adding KOH and KCl, respectively.

sonication, the average diameter 19 nm. For the purposes of various experiments, bottom-up grown SiNWs have to be detached from the growth substrate and redispersed in an aqueous liquid according to the findings presented in the previous section 4.3.1. Once the NW suspension is mixed with the vesicle solution (see Figure 4.23), vesicles adsorb onto the surface. Lipid bilayers are formed around the nanowires by fusion and rupture of unilamellar vesicles (ULV) following the different mechanisms proposed by Richter *et al.* [82], see Figure 1.5. The nanowire represents the substrate for supported lipid bilayer (SLB) formation.

Measuring the  $\zeta$ -potential (see 4.3.1) and characterizing the bilayer quality at different pH values on planar substrates resulted in optimized conditions to carry out SLB formation around NWs (see grey area in Figure 4.22). Crossing the isoelectric points towards higher pH value leads to deprotonation of the amines whereas lower pH results in less homogeneous bilayer shells.

### Characterization on planar substrates

Firstly, the focus was on investigating bilayer formation parameters and improving bilayer qualities on planar and functionalized glass substrates. After cleaning, the slides were functionalized with APTES for 20 s (liquid phase attachment, see appendix A.1). For supported lipid bilayer (SLB) formation, droplets of the vesicle solutions were suspended on APTES-functionalized glass cover slides. After addition of calcium chloride with  $\text{Ca}^{2+}$  concentrations up to 50 mM, the allowed SLB formation time was at least 1 h, followed by buffer rinsing to remove loose vesicles and bilayer patches from the surface. The bilayer thickness in the buffer was measured with an ellipsometer in a liquid cell setup (see chapter 2) and could be determined to be in the range of 4–5 nm with a refractive index of 1.45

[189]. This is in good agreement with previously reported values for DOPC lipids [190]. The same protocol was later applied to the nanowire solutions.

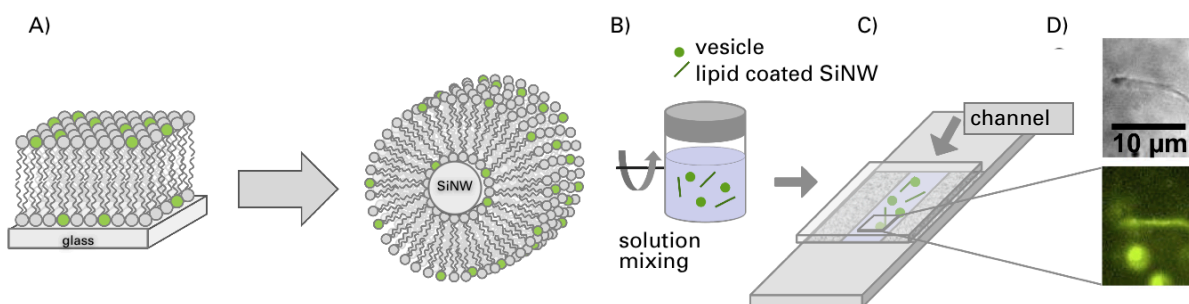


**Figure 4.23.:** Strategy for lipid bilayer wrapping of SiNWs in solution. A) From planar to curved substrates for supported lipid bilayer formation (SLBs). B) Mixing of unilamellar vesicles and APTES-functionalized dispersed SiNWs. C) Injection into fluid channel for fluorescence microscopy. D) fluorescence image and optical image of the same coated nanowire. The nanowire is visible with normal microscopy due to light scattering. See also Röhmlidt *et al.* [84].

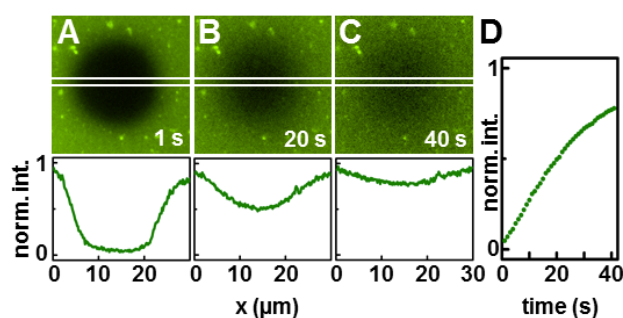


**Figure 4.24.:** Fluorescence recovery after photobleaching of a lipid bilayer on a planar, APTES-functionalized substrate. Three stages after bleaching are presented: A) 1 s, B) 20 s and C) 40 s. The development of the intensity for a time frame of 40 s is presented in D) with a recovery of appr. 75 %.

Formation of SLBs was investigated using a fluorescence recovery after photobleaching (FRAP) technique with the Zeiss microscope see chapter 2. The NBD-labeled films were locally photobleached at minimally opened aperture resulting in dark spots of diameters of approximately 18 μm (NBD see table 2.2). After bleaching, the aperture was opened manually and an image recording series of this area was started (first image 1 sec after bleaching; MetaVue imaging software, maximum two images per second). The recovery of the fluorescence in the bilayer was evaluated by analysing the grey values of the recorded images. A high grey value is assumed to be equivalent to a high degree of fluorescence.

Fluorescence microscopy images of a bilayer formed on an APTES-functionalized glass cover slide within an acetate buffer solution of pH 5 are presented in Figure 4.24. The dark spot in the middle of the images results from a photobleaching procedure as described above. The fluorescence recovery after bleaching of the circular area at 1, 20 and 40 s (see corresponding images in Figures 4.24A)–C)

is depicted. Below the fluorescence images, the respective normalized fluorescence intensities along the stripes between the two white lines are plotted. In figure 4.24D), the time dependence of the fluorescence recovery at  $x = 15.5 \mu\text{m} \pm 1.5 \mu\text{m}$  (minimum position) is shown. At 40 s approximately 75% of the initial fluorescence is recovered. After fast recovery in the first seconds, the intensity approaches a saturation level below the original intensity level. This saturation level depends on the bilayer quality. These results indicate that under the chosen conditions intact SLBs, with a few vesicles attached on top, are formed. Further improvement might be necessary to fulfil the need for defect-free bilayers in electronic applications [191]. In good approximation, the intensity profile directly after bleaching ( $t = 0$ ) is of rectangular shape with a width of  $d=2 \cdot w=18 \mu\text{m}$  which allows estimation of a diffusion coefficient  $D$  after Soumpasis [192]. At  $t_{1/2} = 20 \text{ s}$ , 50% of the original intensity level is reached and  $D$  can be calculated as follows:

$$D = 0.224 * w^2 / t_{1/2} = 0.9 \mu\text{m}^2 \text{s}^{-1} . \quad (4.1)$$

The determined diffusion coefficient is slightly lower than the previously reported values of 2–10  $\mu\text{m}^2 \text{s}^{-1}$  for lipid diffusion on more hydrophilic substrates [193]. This discrepancy can be explained by the lower hydrophilicity of the samples. The contact angle of water on APTES-functionalized  $\text{SiO}_2$  surfaces was measured to be between  $45^\circ \pm 5.0^\circ$  for short attachment on glass and  $60.1^\circ \pm 6.0^\circ$  for Si wafers with native oxide (see Figure 4.1), compared to values below  $10^\circ$  for blank glass and wafer samples. Hydrophobic substrates with contact angles above  $90^\circ$  may hinder bilayer formation on nano-objects [194] which might lead to a further decrease of the diffusion coefficient of the molecules and prevent bilayer formation. In contrast, the charge of protonated amines present in APTES may promote DOPC lipid bilayer formation, as Leonenko *et al.* investigated for APTES-modified mica [195] and lipid bilayers successfully formed on top of amine terminated CNTs integrated in FETs [196]. Thus, it is probable to have stable and homogeneous bilayers with lowered lipid mobility because of electrostatic interactions due to the surface modification.

### Characterization of NWs

In order to coat the nanowires dispersed in water with a lipid bilayer shell, vesicle solutions consisting of ULVs were mixed with the APTES coated SiNW solution at a 1:1 ratio (v/v). The SiNW–vesicle solution was constantly mixed together with  $\text{Ca}_{2+}$  ions for 1 h (see Figure 4.23B).

The vesicle–nanowire solutions were monitored in a fluid channel setup as presented in Figure 4.23C). Two stripes of double-sided adhesive tape on a microscope glass slide leave a thin channel. A glass cover slide is glued on top to close the channel. Due to capillary forces, sample solutions positioned at the channel openings using a pipette are sucked in and can be monitored readily. As a consequence of the confined space focusing of moving objects such as vesicles or nanowires is facilitated.

The NW-lipid solution was observed in the as-mixed state using a setup as shown in Figure 4.23C). Figure 4.23D) shows two images taken successively at one position of a SiNW–vesicle solution mixture. In brightfield settings (upper image) a SiNW can be observed. Although having a diameter of only

around 20 nm the NW is discernable as it diffracts the light. This is also well above the critical diameter for lipid membrane curvature of 5 nm, as reported elsewhere [197]. Thus, no further thickness increase of the 1D template is required, compared to *e.g.* thinner single-walled CNTs [94, 198]. Due to Brownian motion the NW moves inside its fluid environment variably leaving and entering the focus plane. The same SiNW can be observed in the fluorescent light image (see Figure 4.23D), lower image) next to vesicles floating in the solution. As the focus plane is in the middle of the channel and not on the glass cover slide, possible vesicles and bilayers which are out of focus result only in a low background fluorescence. This makes the NW clearly distinguishable from its surroundings. The fluorescence is homogeneous along the whole NW and thus it is fully coated by a lipid shell. Statistical evaluation of 82 nanowires was carried out. 26 % of the NWs could not be evaluated, as the fluorescence of a possible coating was overshadowed by attached vesicles. 54 % of the NWs were covered in a bilayer shell and the remaining 20 % did not show a fluorescence signal. Longer incubation times will probably increase the chances for SLB formation on uncoated NWs. According to Dayani *et al.* [198], 1D templates of comparable diameter with a lipid bilayer shell are stable in buffer solution for 60 days. Moura *et al.* reported single stabilization of a colloidal solution of lipid coated silica particles when intact single bilayers cover the surface with a saturated phosphocholine density [199]. We conclude that SiNWs coated with functional lipid bilayers are also stable in the buffer solution due to steric stabilization by the thin lipid shell.

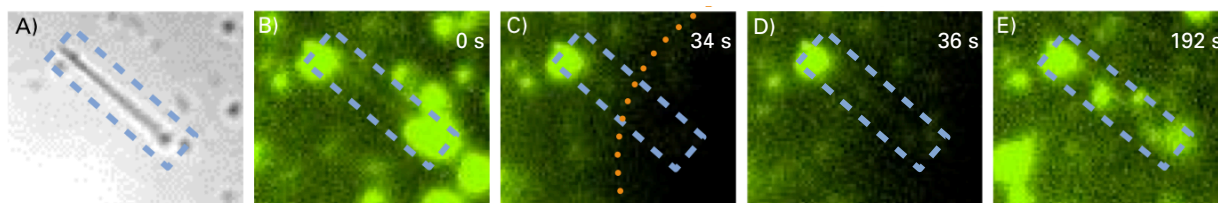


**Figure 4.25.:** FRAP on a SiNW. A) Light microscopy image of the nanowire. B)-E) Series of fluorescence microscopy images from  $t = 0$  to 192 s. The position of the nanowire is indicated by the dashed frame. C) An area partially including the nanowire is photobleached. Already after 2 s (from C) to D), bilayer recovery is observable. E) 158 s after bleaching, the wire appears fully recovered.

Functional lipid bilayers are defined by the ability of the lipid molecules to diffuse within the layer and heal defects. In Figure 4.25, a FRAP experiment involving parts of a nanowire is shown (nanowire indicated within the dashed line frame). Along the wire an increased fluorescence brightness is observable (Figure 4.25B). After photobleaching of part of the area, indicated by the dotted line in Figure 4.25C), the fluorescence along the wire has disappeared. We conclude that this confirms that the glow along the wires is not a consequence of *e.g.* scattering the fluorescent light of surrounding sources but results from the bilayer itself.

Two seconds after photobleaching (see Figure 4.25D), the majority of fluorescence on the nanowire has already recovered, indicated by a reincrease in intensity, whereas the remaining area of the bleaching spot still appears dark. This could mean that the diffusion coefficient on the wire is higher than on the flat substrate underneath. This is consistent with bilayers on 55 nm diameter nanowires inves-

tigated by Huang *et al.* who studied the influence of the substrate curvature on the bilayer dynamics and found higher recovery velocities than on planar substrates [95]. After 3 min, the fluorescence along the wire as well as within the rest of the bleached spot has reached its original fluorescence intensity (see Figure 4.25E).

Figure 4.26 displays a time series of optical and fluorescent images observing the interaction of a vesicle with an APTES-NW *in situ*. The vesicle is moving due to Brownian motion and approaches the wire at  $t = 62$  s (indicated by an arrow in Figure 4.26B). Within the following 22 s the vesicle attaches to the wire via physisorption and detaches again (indicated by an arrow in 4.26C). As a consequence of the contact, a fluorescence intensity increase at the tip of the nanowire is observable compared to  $t = 0$  s. This might be due to a transfer of lipid molecules from the attached vesicle into the already existing bilayer at the SiNW tip during the contact time. Most probably, the fluorescence intensity increase around the nanowire occurred due to these additional NBD-PE lipids (abbreviation see Table 2.2). Furthermore, it is possible that the sharp tip of the nanowire mechanically pulls out parts of the vesicle membrane, also resulting in a transfer of lipids from the vesicle to the nanowire that acts as a template for SLB formation.

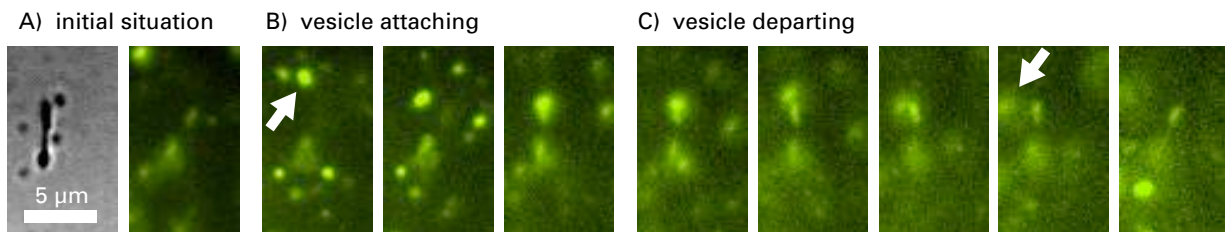


**Figure 4.26.:** *In situ* observation of a ULV which is approaching an APTES coated SiNW and leaving it. This is indicated by white arrows in B) and C). A) Initial situation in optical and fluorescence microscopy. B) The vesicle attaches to the nanowire. C) During contact, lipid molecules diffuse from the vesicle to the nanowire surface indicated by a brighter illumination of the nanowire after vesicle departure.

To summarize wrapping of NWs with lipid bilayers, the conditions for lipid bilayer formation were optimized by characterizing the surface charge of these functionalized NWs using  $\zeta$ -potential measurements. The rapid fluorescence recovery on the nanowires indicated functional lipid bilayers with high lipid mobility, which is crucial for stable solutions. With the presented channel setup, dynamic processes can also be studied *in situ* as exemplarily shown in Figure 4.26.

The semiconducting and highly sensitive characteristics of SiNWs make them an interesting nanomaterial for various applications. Device integration for nanoelectronics is important for technological purposes such as biosensors. For the development of bottom-up processes in contrast to conventional top-down technologies, biological self-assembly can be used as a positioning tool. In this case, the developed method of highly concentrated lipid coated SiNWs in aqueous solution can be used together with the incorporation of functional lipid molecules such as biotinylated lipids. In combination with the strong biorecognition between biotin and streptavidin, this can be one option for creating SiNW arrays. In addition, knowledge regarding functional lipid bilayers on small curved objects helps to



---

integrate lipid films as non-covalent functionalization layers in e.g. NW based FETs preventing the issue of unspecific protein adsorption. The advantage of bilayer coating in solution over techniques on substrates like TEM grids is that NW–lipid structures within the solution can be easily studied with a variety of techniques such as UV/Vis spectroscopy or, suspended onto different substrates, with TEM or AFM.



## 5. Towards SiNW FET Biosensing

After presenting the extensive analysis of the functionalization of SiO<sub>2</sub> surfaces with chemical and biological molecules and the subsequent characterization of the interaction of surface-bound receptors with the analyte in solution, this chapter deals with the application of these findings for FET based sensing on SiNW FET devices with both bottom-up and top-down fabricated NWs. First, the focus is made on probing the FET device characteristics and detection of protein thrombin; secondly, we demonstrate the analysis of the small antibiotic molecule amoxicillin.

### 5.1. Thrombin detection

#### 5.1.1. Bottom-up SiNW FET setup

##### Experimental setup of FET biosensor

The chip fabrication is presented in the fundamentals in section 1.4.2. On two sides of the chip, nanowires can be connected to source and drain (see Figure 5.1A) and B). The nanowires themselves are positioned within the middle of the chip along a horizontal line (*i.e.* the channel position), as presented in Figure 5.1B). They are aligned in between the interdigitated finger structure of the nickel contacts (see Figure 5.1C).

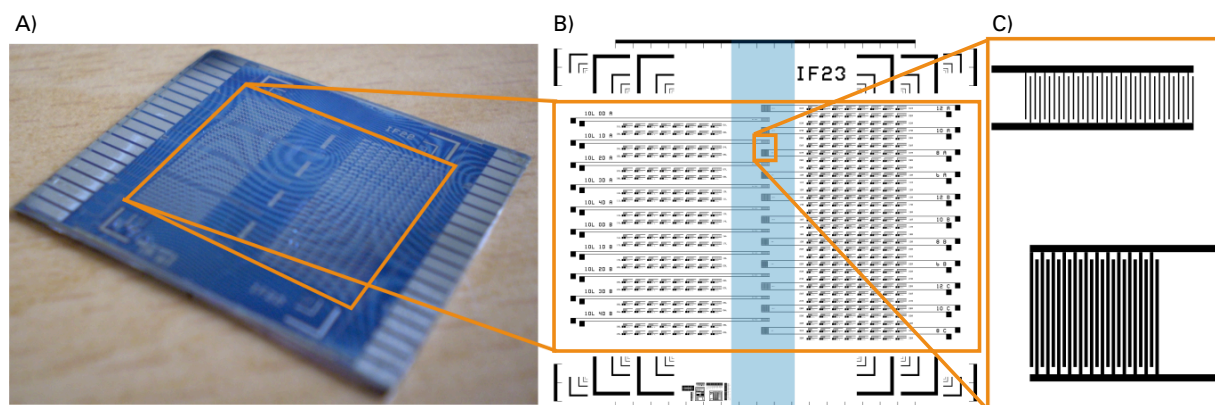


**Figure 5.1.:** A) Picture of a chip. Courtesy of F. Zörgiebel. B) Latest chip design of the labeled region in A). The blue area marks the location of the fluidic channel. Courtesy of S. Pregl. C) Magnified detail showing different interelectrode spacings of the interdigitated finger electrodes.

The tip-probing station comprises of a microscope, a metal chuck connected to a vacuum pump and two needle holders with micropositioners (Karl Suss Microtec) to contact the sample to source and

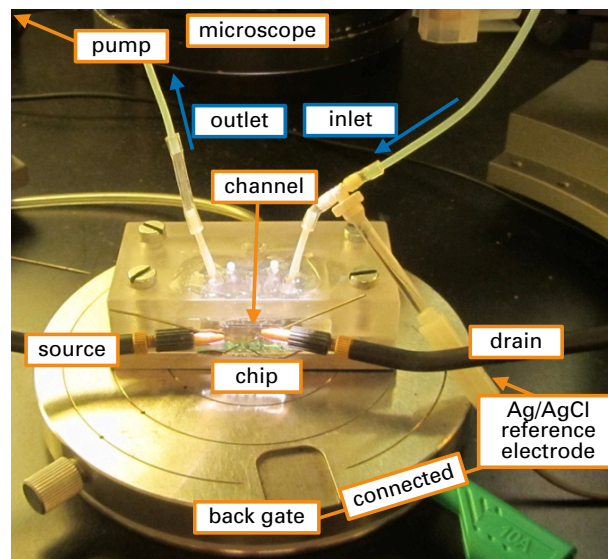


**Figure 5.2.:** Experimental setup of bottom-up FET with external reference electrode (Ag/AgCl).

drain (see Figure 5.2). Both are connected to the Keithley 2602 SourceMeter. The chuck (back gate) is connected with the reference electrode (liquid gate) when measured in solution. The measurements were controlled with matlab scripts instantaneously record I-V curves or to monitor continuously the device behaviour. The sensor itself, the SiNW FET chip, is placed below a polymer cover with a molded PDMS channel in such a way that the sensitive NW regions are within the channel area (blue stripe in Figure 5.1B). By screwing a metal plate from below, the channel is sealed as the chip is fixed between the metal base and a polymer cover. Tubings are connected to the cover to assure in- and outlet of solutions. At the inlet side, a flow-through reference electrode is connected via a T-junction (Ag/AgCl in KCl, Microelectrodes Inc.). This reference electrode acts as a liquid gate to measure in the transistor configuration. As the metal contact pads of the chip are outside the clamped chip region, they can be connected to the needles of the probe station. Pumping of liquids is carried out via a syringe pump (Harvard Apparatus PHD 2000) and in refill mode (*i.e.* it is pulling the liquid through the tubes). The inlet end of the tube is immersed in 2 ml standard tubes with the measured solution inside.

### 5.1.2. Device characterization

#### Data analysis

Matlab was not only used to control the applied voltages but also to analyze the obtained data. The x and y values of transfer curves (static measurement of one up and down sweep of transfer curve) can be extracted from matlab and further treated with Origin software for graphs. Threshold voltage steps were obtained by comparing the voltages at a fixed source drain current  $I_{sd}$ . Definition of the threshold voltage is presented in section 1.4.

In detail, the threshold voltage was analyzed for the mean I-V curve, *i.e.* the mean values of the up

and down sweep of the gate voltage as the devices exhibit a certain hysteresis. In addition, a running mean value was determined averaging 15 neighbouring data points for each value to flatten artefacts in the measurement. The initial level  $V_{t,0}$  can be extracted from the curve shortly before injection of the first analyte concentration when only measurement buffer without any thrombin is present on the chip surface. In case this region shows a drift, a baseline can be subtracted from the whole curve.  $\Delta V_t$  is obtained by subtracting  $V_{t,0}$  from  $V_{t,i}$ . This mean  $\Delta V_t$  is presented in Figure B.3 versus the corresponding thrombin concentrations for different measurements. Averaging over different devices and measurements is possible but one needs to keep in mind the device-to-device variations of NW based FETs [200]. Single transfer curves were extracted from the continuous sweep in case it was required for analysis.

### Device characteristics in dry and liquid conditions

As a first device characterization, all single devices on one chip are tested in dry conditions to determine the working devices. Moreover, it allows to choose the device with the best on/off current ratio and transfer curve for measurements in liquids. In dry conditions with back gate configuration, gate voltages of 10 V are possible. After mounting the chip into its holder, water and buffer are flushed subsequently. The transfer curve is then measured again in liquid gate configuration. Now, lower voltages with a maximum of 2 V are applied to avoid damage to the device.

Both transfer curves of the same device are presented in Figure 5.3 with two different y-axes (black

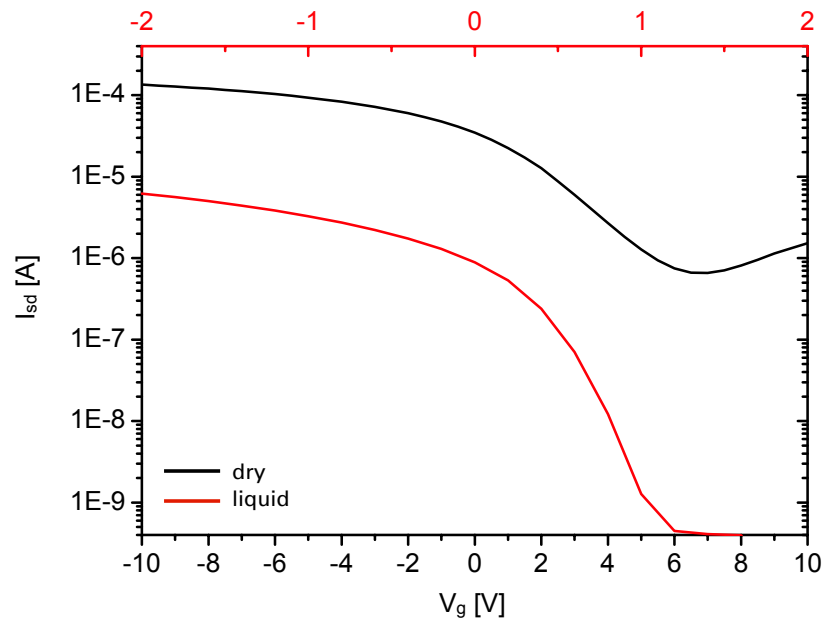


**Figure 5.3.:** Transfer curves of same bare device in dry conditions (back gate) and in 100 mM sodium phosphate buffer of pH 6 with the reference electrode as in setup see Figure 5.2 (liquid gate).  $V_{sd}$  values are 1 V in dry and 0.1 V in liquid conditions.

graph for dry environment:  $\pm 10$  V and red graph for liquid environment:  $\pm 2$  V). The curve slope and shape are similar but the on/off current ratio is different which is also because of the different gate voltage range.

### Influence of flow rates and ionic strength on the device characteristics

In order to determine the influence of flow velocities on the measured FET signal, different flow rates were tested. In parallel, three ionic concentrations were compared to find optimal flow rates for different buffer strengths. Sodium phosphate buffer (SPB) with a pH of 6 was prepared in three different concentrations, namely 0.03, 0.8 and 4 mM. In Figure 5.4, the threshold voltage is plotted against the running time of the experiment. The device is a bare device with  $\text{Al}_2\text{O}_3$  passivation. The orange bars show which ionic concentration was used. The thin blue bars indicate the flow rate during pumping as specified on the left. In between pumping steps, the liquid is not moving.

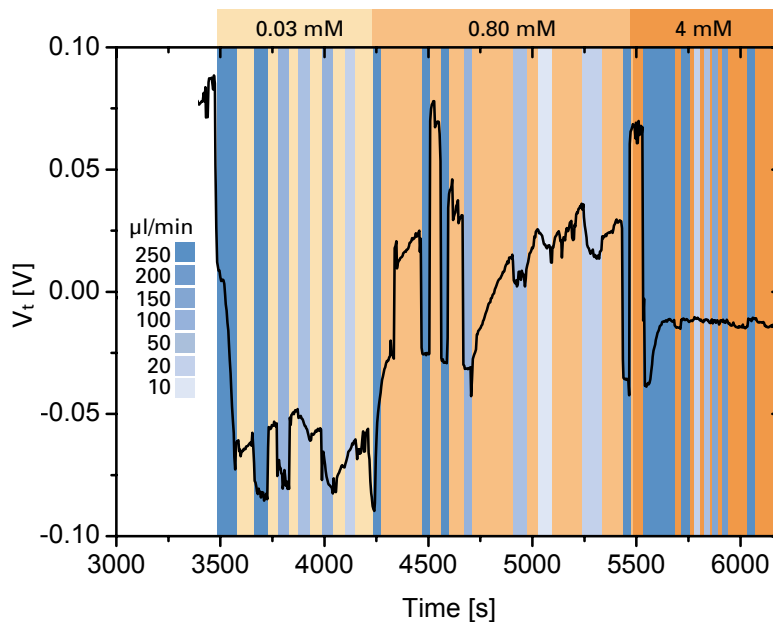


**Figure 5.4.:** Threshold voltage at  $I_{sd} = 1 \cdot 10^{-8}$  A versus time. Starting with sodium phosphate buffer at the lowest concentration (0.03 mM), different flow rates from 250 to 10  $\mu\text{l}/\text{min}$  were applied (blue bars). The area left orange shows the device response in the pump-off mode.

Firstly, the buffer with the lowest concentration was pumped over the sensor surface with decreasing flow rates from 250 down to 20  $\mu\text{l}/\text{min}$ . At high velocities there is an immediate voltage jump after starting the pumping with a sharp voltage decrease, but stabilizes after some time. After turning off the pump, the signal increases to a higher value and stabilizes. The jumps are smaller and less steep for lower flow rates as it can be seen for 50  $\mu\text{l}/\text{min}$  (fourth blue stripe from the left). At 0.80 mM, the situation is similar. The signal is affected at all flow rates, but above 50  $\mu\text{l}/\text{min}$ , the jumps are more pronounced and sharp. At 4 mM buffer concentration, the device is much more stable. After

the initial complete exchange of the buffer solution because of the first pumping, the signal is little affected even at the highest velocity. As discussed in section 1.4.3, the Debye layer thickness increases with reduced ionic concentration but is less firmly attached. By inducing a shear force because of the flow, the outer layer may be washed away. This effect can be reduced significantly by optimizing the buffer concentration. Figure 1.14 illustrates that the optimal concentration for a sensitive FET device using aptamers as recognition receptors can be found in between 1 and 10 mM. The measurements were started at 1 mM. To achieve a signal without effects of the pumping itself it might be better to go to slightly higher ionic strength like 4 mM which showed a much better performance even at high pumping velocity than 0.8 mM.

To summarize, both parameters flow rate and ionic strength influence the device signal. The goal is to achieve a stable signal which is not reacting to pumping but only to changes of the analyte solution. For this, a certain ionic strength is required as the pumping cannot be carried out at an indefinitely small flow rate.

### Real-time pH sensing

ISFETs are sensitive to pH changes as the surface hydroxyl groups can take or give away protons. As a first test of any device, pH measurements are often carried out to characterize the functionality of the device. Here, a sensor chip mounted into the chip holder was flushed with several pH solutions of identical ionic concentrations at a flow rate of 250  $\mu\text{l}/\text{min}$ .

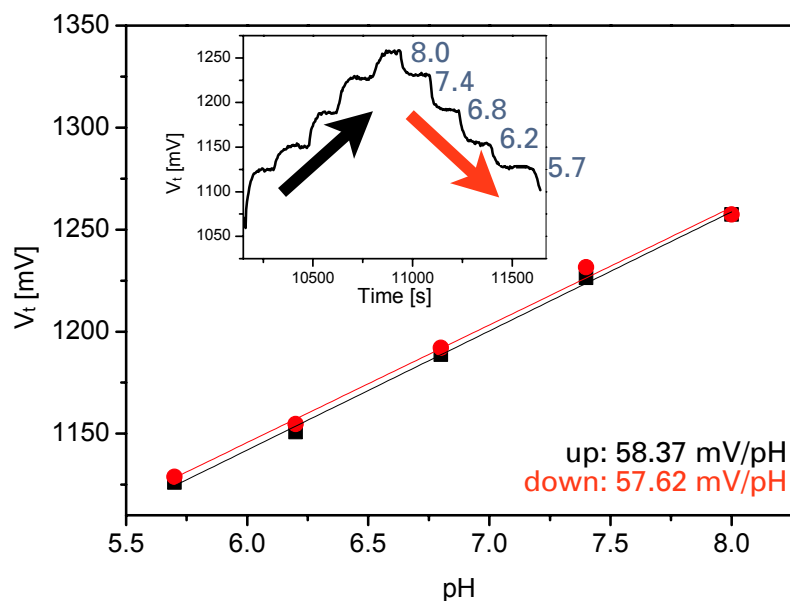


**Figure 5.5.:** pH sensitivity of  $\text{Al}_2\text{O}_3$  passivated SB SiNW FET sensor measured from pH 5.7 to and 8 and reverse. The inset shows the voltage steps induced by the buffer change because of their different pH values. The slope of the linear fit confirms the near ideal Nernstian behaviour of  $\text{Al}_2\text{O}_3$  devices [107].  $I_{sd} = 1 \cdot 10^{-8}$  A.

The continuous measurement was started with the lowest pH, *i.e.* 5.7 up to 8.0 and reverse, see Figure 5.5. The defined threshold voltage steps for a sodium phosphate buffer of 10 mM concentration are visible in Figure 5.5 (inset). The device sensitivity was derived from the voltage changes per pH. Both directions, *i.e.* increasing and decreasing pH steps, exhibit a sensitivity of around 58 mV/pH which is close to Nernst limit. In comparison, the same device type without passivation layer only results in a sensitivity of around 20 mV/pH above pH 6 as SiO<sub>2</sub> is exposed to the electrolyte solution [201]. The obtained pH sensing behaviour is in good agreement with previous works on Al<sub>2</sub>O<sub>3</sub> coated FETs [107, 202] and demonstrates the capability of real-time pH sensing with this ALD passivated SiNW FET sensor.

### Influence of surface modification

FETs are surface sensitive devices. The high surface-to-volume ratio of nanowires leads to a strong influence of the surface modification on the electrical characteristics of the nanowires based FETs (see section 1.4). Once the surface potential is changed, the transfer characteristics will be influenced. This can be used to verify the attachment of molecules to the surface. The surface modification steps have been characterized extensively in chapter 4. The effect of modification on the FET devices is thus only presented exemplarily.

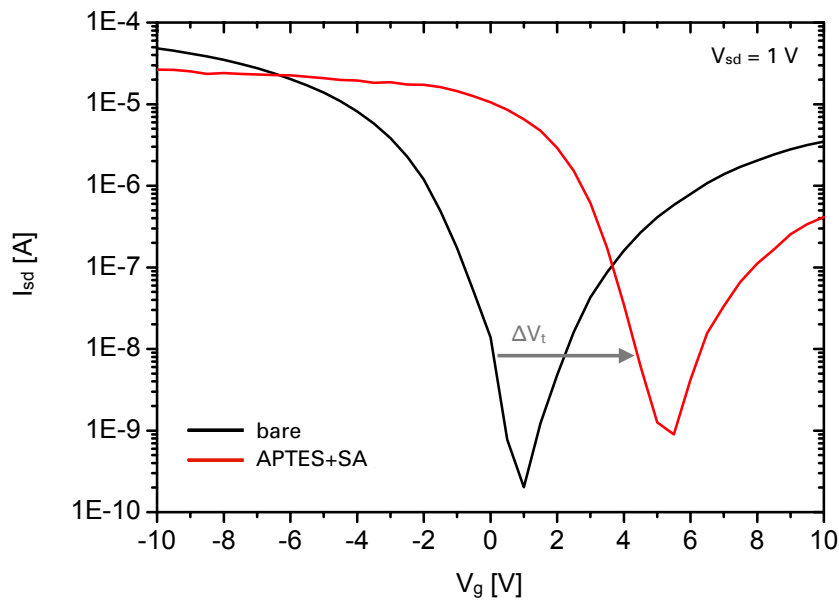


**Figure 5.6.:** Transfer curves before and after functionalization with APTES and succinic anhydride (SA) in dry conditions (back gate configuration). The functionalization was carried out directly via the channel. The voltage at  $I_{sd} = 7 \cdot 10^{-9}$  shifts 4.2 V to the right for the functionalized device.

The bottom-up SiNW FET was characterized in the clean and bare state as well as after attachment of APTES and succinic anhydride (SA) in the flow cell. The I-V curves however were taken without any buffer, *i.e.* in the dry state, see Figure 5.6. The voltage shifts for about 4.2 V to the right at a fixed  $I_{sd}$ . On the contrary, only APTES modification leads to a significant shift in the opposite



direction (not shown here). This reflects the different signs of the surface charges being negative for carboxy and positive for amino groups. These measurements indicate the strong influence of surface modification on the device behaviour. Tarasov also confirms the influence of surface modification with a different silane leading to a complete loss of the pH sensing ability for thick layers as no surface groups that can take or give away protons are present anymore [105]. Thus, on-chip checking of the functionalization is possible as an additional confirmation technique complementing others.

### 5.1.3. Biosensing

#### Thrombin shift

It is important to know in which direction a thrombin induced shift occurs. Earlier works recommend to use a buffer with a pH considerably below the pI of 7.0-7.6 to obtain charged thrombin [3, 20]. At 7.4, thrombin is neutral according to the supplier information (see section 2.2) whereas at lower pH values the overall charge will be positive. A relatively high thrombin concentration was prepared in order to achieve a distinct signal. 200 nM thrombin was flushed over the FET sensor surface, diluted in the same buffer type but two different pH values, *i.e.* a 5 mM sodium phosphate buffer of pH 6.0 and 7.4, respectively. Sodium phosphate buffer (SPB) is a suitable buffer for the selected pH range (buffering from pH 5.7 - 8.0, see appendix A.2). Thrombin is a protein and is expected to physisorb onto the surface. For positive charges, the transfer curve shifts to the left. Figure 5.7 displays two graphs measured on two different devices of one chip with A) pH 6.0 and B) pH 7.4, comparing the initial transfer curve with the curve after thrombin adsorption. The curves for neutral pH are almost identical whereas for pH 6.0 a distinct but small shift of the complete curve to the left with 16 mV is observable and confirms the expected direction. The reason for the rather small shift compared to Hammock *et al.* could be the slightly higher pH here (6 instead of 5.5), a buffer with higher ionic strength (approximately factor 100) and a possible lower thrombin concentration [3].

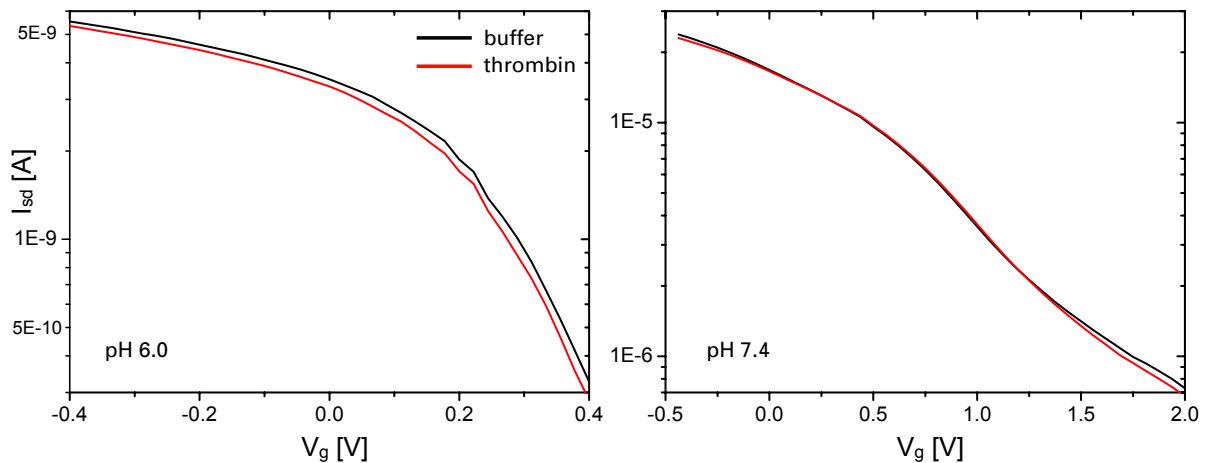


**Figure 5.7.:** Transfer curves before (black) and after thrombin physisorption (red) in steady conditions (*i.e.* no flow). A) Shift at pH 6.0. B) Shift at pH 7.4.

## Thrombin sensing

First steps towards FET sensing were carried out using the protocols tested previously with other biosensing techniques (see chapter 4). The transfer curve of a carboxy-terminated surface is presented in paragraph 5.1.2 and is shifted compared to a bare transistor because of the applied modification. The reacting molecules were delivered via the channel of the flow cell. As the reaction of succinic anhydride and EDC with the present surface groups have to happen immediately after injection, the channel delivery is not practical as it is too slow, *i.e.* the molecules already reacted in solution and not on the surface. In addition, this scheme requires incubation in different aqueous and organic liquids which may lead to partial degradation of metallic contacts which are not ALD-passivated. Therefore, TBA1 for FET sensing was attached to the sensor surface via the epoxysilane method (see section 2.1.2). The prefunctionalized sensor chip was mounted into the holder and flushed with TBA1. After incubation for covalent aptamer attachment the sensor was ready for thrombin detection in the flow cell in continuous measurement mode.

The DNA strands were attached in the flow cell. The DNA stock solution was diluted in a 10 mM PBS buffer of pH 8.5-8.9 (tuned to this pH by 1 M NaOH addition). This pH is required for covalent bonding of primary amines with epoxy surfaces to form stable aminoalcohols (see section 2.1.2). After incubation, loosely adsorbed strands were washed away by buffer rinse. This was followed by a Tris buffer rinse and incubation to support the aptamer folding (buffer protocol see appendix A.2). For thrombin detection, the device was brought into contact with the measurement buffer, a sodium phosphate buffer (SPB). A 100 mM SPB solution of pH 5.7 (prepared according to the appendix A.2) was diluted to 1 mM and injected at a flow rate of 250  $\mu\text{l}/\text{min}$ . After obtaining a stable baseline with SPB, the solution was exchanged with the same buffer (from the same stock vial), but spiked with the lowest thrombin concentration. After assuring that the whole device surface is covered with the new solution, the sensor was left to stabilize for around 100-200 s before the next thrombin concentration was added. By pumping each new solution, rinsing with the old and lower concentrated solution is provided which should remove loose protein molecules. The mean voltage at a constant  $I_{sd}$  versus running time of one experiment is displayed in Figure B.1 in the appendix. At an ionic concentration of 1 mM to assure sensitivity of the device, voltage steps are visible once the pump is turned on which might be because the Debye layer is rinsed away (see discussion of pumping influence in section 5.1.2). To distinguish this from the thrombin related signals, only voltage levels in the steady state were taken for analysis where the pump is turned off and the signal has had time to stabilize. For details, see also the corresponding figure caption in appendix B.

To probe the sensor, different setups are compared in the following. Thrombin concentrations ranging from 400 nM down to 2 pM were tested (400 nM, 200 nM, 63.3 nM, 20 nM, 6.33 nM, 2 nM, 633 pM, 200 pM, 63.3 pM, 20 pM, 6.3 pM, 2 pM) on a TBA1 surface without and with BSA blocking and on a scrambled DNA sequence of similar length (SCR). The devices were measured from -0.5 to maximally 1.5 V (gate voltage  $V_g$ ) at a source drain voltage  $V_{sd}$  of 0.1 V. Around 400 ml of thrombin were pumped using a flow rate of 250  $\mu\text{l}/\text{min}$  and with an ionic SPB concentration of 1 mM to certainly keep the biorecognition events within the Debye layer.

Exemplarily, Figures 5.8 and 5.9 display the measured I-V curves of one TBA1 coated sample (sweep direction from 1.3 to -0.5 V) for the individual thrombin concentration steps from 0 M (black) to 200 nM (red) showing a continuous shift to the left, except for 200 nM shifting back to the right. The complete range displayed in Figure 5.8 visualizes where the curve slope is maximal and parallel at the same time. The grey arrow in Figure 5.9 which magnifies the area of steepest slope of the curves from Figure 5.8 indicates the  $I_{sd}$  level at which  $V_t$  has been determined. The automated analysis of the whole continuous measurement (see Figure 5.10) however included the mean I-V curve between up and down sweep, as discussed earlier in this section in the paragraph on data analysis. With  $I_{sd}$  at the steepest slope of the parallel I-V curves for highest device sensitivity, the voltage steps can be extracted. Via software-aided complete automation of these steps, a more general sensing concept for this FET sensor will be applicable and is one option for analysis. By this, voltage shifts can be analyzed where the device exhibits the highest signal change, but this voltage is not necessarily identical with the real threshold voltage according to the definition. In Figure B.2A) and B) in the appendix, concentrations down to 2 pM were screened and these curve shifts show a similar trend as this device.

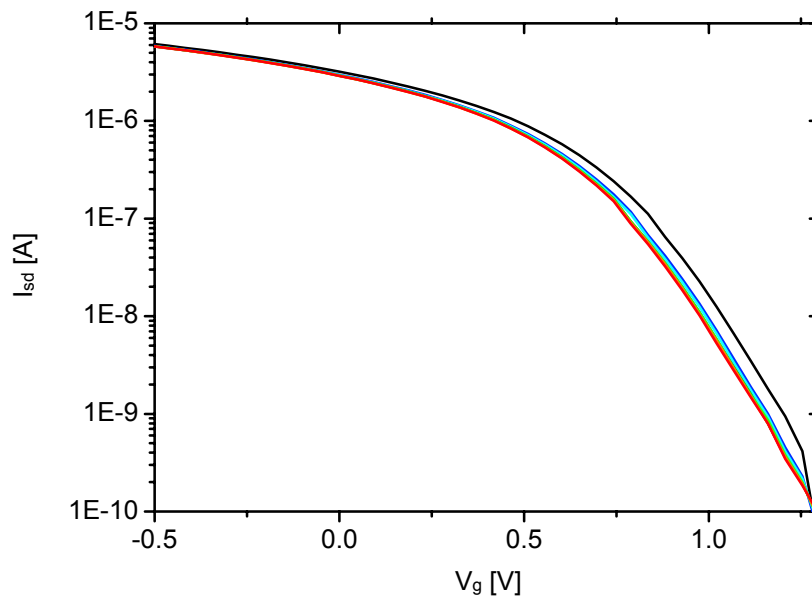


**Figure 5.8.:** I-V curves of TBA1\_B for 7 concentrations and the starting point  $V_{t,0}$  on the black line. Only I-V curves of measuring from 1.3 down to -0.5 V (gate voltage) are presented. The colour legend is displayed in the next Figure.

The results of the voltage steps versus the thrombin concentration for the individual measurements are presented in the appendix in Figure B.3 with the full range of probed thrombin concentrations. Each data point in Figure 5.10 represents the mean value of two measurements for TBA1 and SCR as a capture layer, respectively, without any blocking. The graphs only show the mean signal of two

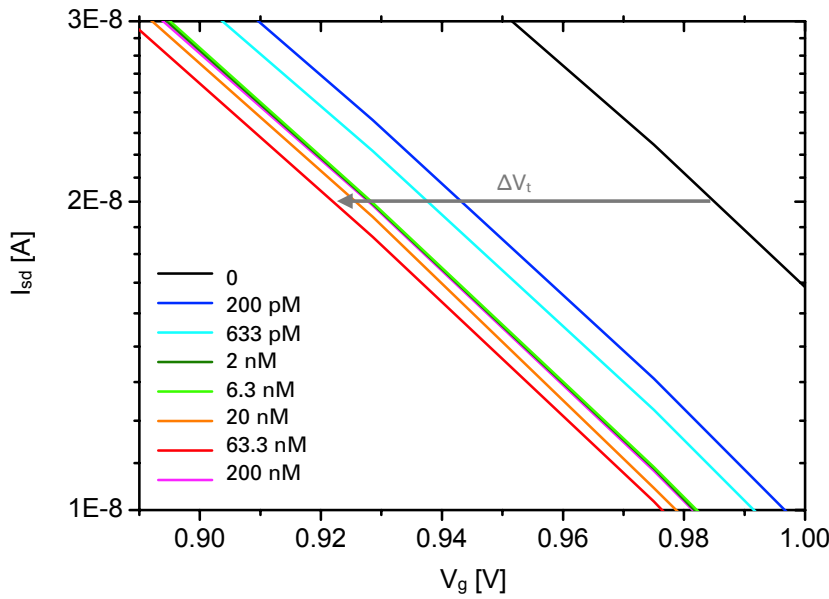


**Figure 5.9.:** Magnified detail of the I-V curves of TBA1\_B for 7 concentrations and the starting point  $V_{t,0}$  on the black line. The grey arrow indicates the shift direction at  $I_{sd}$ .

sitinct devices where two values were available, *i.e.* from 200 pM up to 200 nM. Starting with 200 pM thrombin in solution, a  $\Delta V_t$  of around 50 mV is detectable. The step size compared to the initial level (*i.e.* 0 mV) increases to almost 73 mV for 63 nM. For the highest concentration of 200 nM, no further signal increase could be detected. In comparison, the  $\Delta V_t$  for thrombin on control samples with scrambled DNA sequence shows a slight signal increase starting from 16 mV for 200 pM up to 25 mV for 63 pM. Similar to the TBA1 samples, no further increase is observable for 200 nM. The addition of BSA to block the surface before thrombin injection seems to lead to decreased signals at a level in between controls and TBA1 coated FETs, as shown in Figure B.3 for one example (pink curve).

The sensor obviously responds to the increasing thrombin concentrations. The comparison of TBA1 as capture layer with the SCR samples shows that the signal for TBA1 functionalized FET chips is significantly higher than for the controls with SCR. The individual device curves are displayed in Figure B.3. The devices with SCR exhibit a signal increase which can be attributed to unspecific adsorption of thrombin. Blocking is necessary to reduce this effect. Without blocking, many thrombin molecules will adsorb unspecifically initially which might also explain the relatively high signal in the beginning of both experimental setups – TBA1 and SCR. The additional signal can be attributed to the specific thrombin recognition of the aptamer. Figure B.3 (pink curve) shows that the signal for thrombin after BSA blocking is reduced but still higher than for the controls. As only one measurement is displayed, further tests will be necessary to optimize the blocking. Because of the pumping influence on the signal and other difficulties, a detection limit could not be determined yet although a threshold

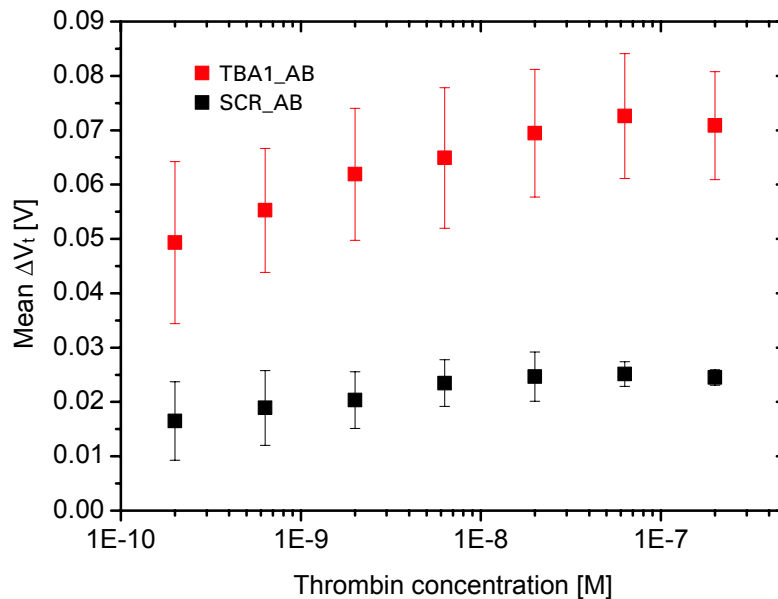


**Figure 5.10.:** FET concentration curves of thrombin detection taken in steady state with TBA1 as a capture layer (red) and SCR as a control aptamer (black).

voltage shift could be observed in the picomolar range of thrombin concentrations. For aptamer based SiNW FET biosensors, a detection limit of 330 pM thrombin has been published so far (see also Table 1.1). A two-dimensional organic FETs, functionalized with aptamers, allowed to detect thrombin down to 100 pM as published recently [3]. So we expect to be able to finally achieve lower values, also because of the proposed higher sensitivity of NW based devices compared to two-dimensional FET sensors.

For direct comparison, parallel measurement of sample and control as a reference would be advantageous for the specificity of the measurement. For this multiplexed sensing, site-specific functionalization with different capture layers and their controls as well as wire bonding are required and currently in development. Techniques like nanoplotting of the aptamer as presented in chapter 4 could be integrated in the future. As there are device-to-device variations, the absolute values of  $V_t$  might differ for samples that have been prepared identically. This influence however should be smaller for our parallel arrays of SiNWs compared to single wire FETs. The visualization of the individual measurements in Figure B.3 with the same capture layer illustrates the importance of applying identical parameters to the devices in terms of  $V_{sd}$  and  $V_g$  in order to make the step height more comparable.

For the ongoing sensor development, it is important to initially obtain a stable buffer line and to exclude device drifts from the signal after measurement, work at a lower velocity and a slightly higher ionic concentration so that pumping does not affect the signal. By this, the risk of detecting false signals will be reduced.

## 5.2. Amoxicillin detection

### 5.2.1. Top-down SiNW FET setup

The fabrication of top-down SiNW FET chips and the chip design are described in section 1.4.2 and are also explained in detail in the publications from Rim *et al.* [4, 116]. The chip itself was measured on the same probe station as the bottom-up SiNW FET, but without a channel setup. Solution droplets of  $25\ \mu\text{l}$  were deposited onto one of the four sensitive regions with each 8 devices, see descriptions in Figure 5.11. The tip surface of a silver wire of 1 mm in diameter was converted to AgCl due to electrolysis against a platinum wire. The tip was then immersed into the solution droplet, whereas the other end was connected to the chuck (back gate) and acted as a liquid gate. After each functionalization step, I-V curves of all devices were measured subsequently.

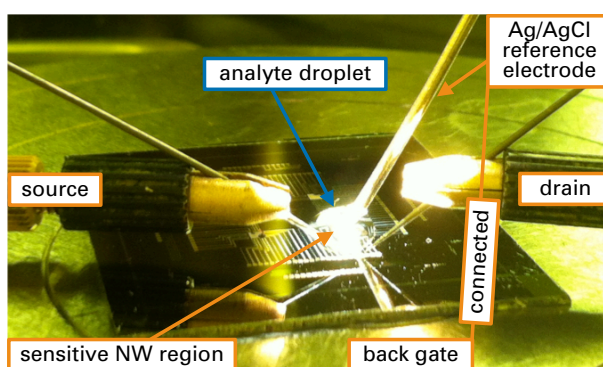


Figure 5.11.: Experimental setup of top-down FET with external reference electrode (Ag/AgCl).

### 5.2.2. Device characterization

#### Data analysis

The obtained I-V curves, measured from  $0 \rightarrow 1 \rightarrow -0.7 \rightarrow 0\ \text{V}$ , were directly treated with Origin.  $V_t$  was determined at the steepest slope at a fixed current for all modification steps on one device.

#### Characterizing the individual modification steps

The different functionalization steps were probed in 0.1 mM PBS buffer ( $= 0.01\ \text{x}$ ) with physiological pH directly on the FET chip by analyzing the threshold voltage shifts. Comparing bare to GOPMS-functionalized devices, the I-V curves of 7 measured devices on one chip shifted to the right with a mean value of  $185 \pm 16\ \text{mV}$ . In Figure 5.12 one device is exemplarily displayed (shift from black to red curve). Adding AMX results in a clear shift further to the right by  $35 \pm 10\ \text{mV}$  which was tested also on 7 different devices of one chip (see the blue curve in Figure 5.12). As FETs are sensitive to surface charges, the added functionalization layers clearly change the transfer characteristics in a consistent manner in one direction. Both molecules, GOPMS and AMX obviously attract negative

surface charges to the NW surface. Although it is hard to estimate the layer quality from here, the measurements prior to biosensing help to verify each modification step on-chip and rapidly.

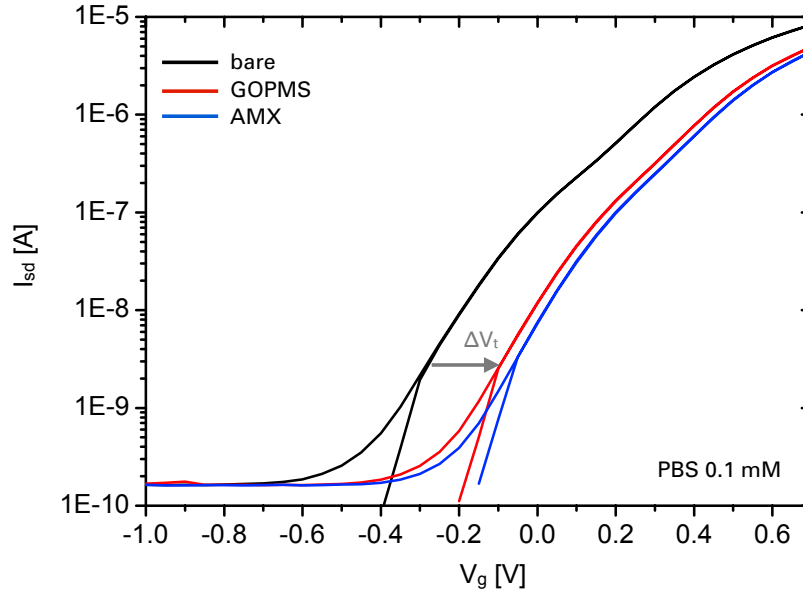


**Figure 5.12.:** Transfer curves before and after functionalization with GOPMS (via gas phase attachment) on TD SiNW FET device. The curves were measured in 0.1 mM pBS buffer at pH 7.4 (liquid gate). For  $I_{sd} = 2.8 \cdot 10^{-9}$  the voltage shifts 185 mV to the right.

### 5.2.3. Biosensing

#### Antibody shift

IgG antibodies show a pI in the range of 6.4-9.0 [203]. Thus, the shift direction depends on the pI of the used monoclonal antibody as well as the buffer. A positively charged antibody would force the transfer characteristics to shift to the left. To probe the expected shift direction, a high concentration of the antibody was allowed to physisorb on the bare surface indicating an overall positive charge not only at pH 7.4 but even at pH 8.8 (0.1 mM PBS buffer, see Figure 5.13) with a shift of almost 30 mV. Within the group of IgG antibodies, the anti-amoxicillin antibody appears to exhibit a pI at the upper limit of the range. Thus, further experiments were carried out at the lower pH 7.4 as it probably provides a more stable environment for the biorecognition and could allow to measure higher voltage shifts at a fixed  $I_{sd}$ .

#### Amoxicillin sensing

After confirming the assay specificity for anti-AMX antibodies on planar surfaces with AuNP labeling by secondary antibodies and visualization in SEM (see section 4.2.2), increasing antibody concentra-

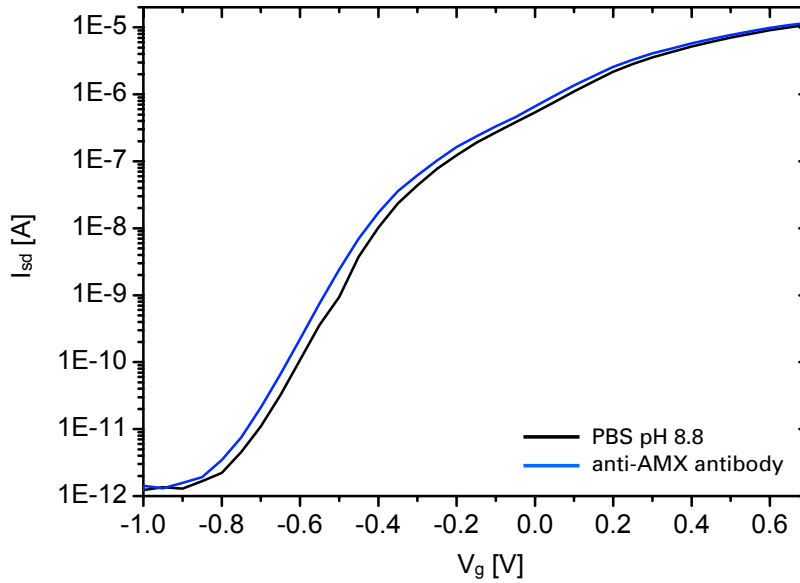


**Figure 5.13.:** Transfer curves before and after physisorption of anti-AMX antibody on bare device at pH 8.8 show a shift to the left.

tions were tested on AMX-functionalized surfaces (see experimental setup in Figure 4.19A) to probe the device sensitivity. Droplets of three concentrations (antibody dilutions from stock: 1:4000, 1:2000 and 1:500) were deposited on one of the four NW regions. The antibody concentration can only be estimated according to the supplier and is around 1-10 mg/ml for a dilution of 1:500 (supplier see Table 2.2). After a waiting time of 10 min, the first antibody detection step was measured on the individual devices. The liquid was removed via a pipette and a droplet containing the higher antibody concentration was deposited on the same spot. By this, the transfer characteristics for each step were acquired compared to the initial curve after AMX attachment, see blue curve in Figure 5.14A). For comparison, the GOPMS curve (red) is also displayed. Each data point in the concentration curve in Figure 5.14B) is the mean of two devices on one chip. At zero antibody concentration the curve shift is zero. All four points were fitted using an exponential decaying function (see equation in Figure 5.14). The threshold voltage shift compared to the initial situation (= blue curve) increases with each step and seems to approach a saturation limit. Many biosensors show a certain saturation at elevated analyte concentrations. The error bars are relatively high indicating device-to-device variations. The NW thicknesses and lengths vary for each device which might be one explanation for the different step sizes. From these results however, it can be derived that the devices are sensitive for increasing antibody concentrations and thus the inverse competition assay can be introduced (see experimental setup in Figure 4.19B).

For the inverse competition assay, the devices were equally functionalized with GOPMS and surface-AMX. Sample-AMX of various concentrations ranging from 40  $\mu\text{M}$  down to 40 nM was then incubated



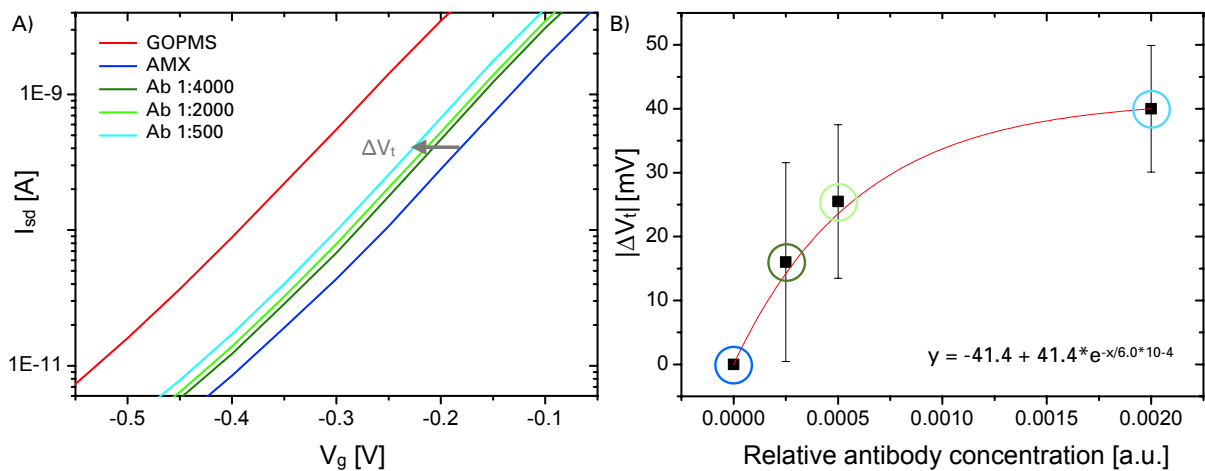


**Figure 5.14.:** A)  $I_{sd}$  as a function of the applied gate voltage for GOPMS and AMX functionalization and antibody detection of three dilutions. B) Threshold voltage shift at  $I_{sd} = 4 \cdot 10^{10}$  A as a function of the relative antibody concentration. The red curve is a fitting curve (exponential decaying function).

with a fixed antibody concentration (1:500 dilution from antibody stock) for 30 min in measurement buffer of pH 7.4. To firstly probe the influence of AMX in solution on the device characteristics, droplets with the highest AMX concentration, *i.e.* 40  $\mu\text{M}$ , but without antibodies were deposited onto the sensitive NW regions. Averaged on 5 devices, the AMX solution shows a shift of the I-V curve of  $9.7 \pm 2.7$  mV to the left, *i.e.* in the same direction as the antibodies (see grey square in Figure 5.15). After this, 25  $\mu\text{l}$  droplets of the prepared antibody-AMX mixtures were deposited onto the NW regions, starting with the highest AMX concentration as this was supposed to already react with many antibodies in solution leaving little amount of free antibodies for biorecognition with the surface-AMX (competition assay). This was confirmed prior to FET sensing by AuNP labeling, see Figure 4.19C). The transfer curves were measured after 10 min of incubation. In between the steps, the sensitive NW regions were incubated with the buffer solution for rinsing. Figure 5.15 displays the absolute values of  $\Delta V_t$  versus the AMX concentration. For high AMX levels, a low signal is expected but the signal should increase for lower AMX levels. The mean threshold voltage shifts (average of 5 devices for all concentrations except for the lowest concentration 40 nM which is only the average of 4 devices) however deviates around 25 mV. More detailed, all single devices do show a small but distinct shift increase from 40 to 4  $\mu\text{M}$ , but for 400 and 40 nM the signal is again slightly reduced. This means that the sensor initially response to the increasing antibody concentrations from only AMX (grey square) to 40 and 4  $\mu\text{M}$  AMX mixed with antibodies, but then saturates at around 25 mV. Possibly, all surfaces had been covered with antibodies so that newly arriving antibodies were not sensed anymore by the device as it happened outside of the Debye layer. Unfortunately it is hard to estimate the antibody concentration as the supplier only gives the dilution ratio for experiments. It can be assumed that the antibody concentration was too high and higher dilutions from stock are

necessary to allow for detection of lower sample-AMX concentrations. In addition, the influence of AMX is overlaying with the antibody as they seem both to exhibit a net positive charge.

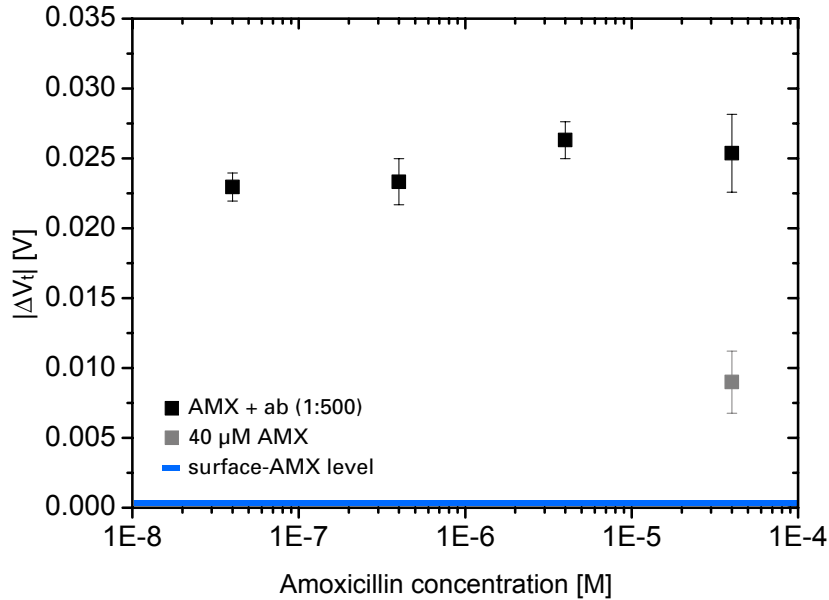


**Figure 5.15.:** Concentration curve of inverse competition assay for AMX detection using antibodies. The grey value shows the  $V_t$  change of AMX in solution without any antibody compared to the initial curve of AMX-functionalized devices (blue = level 0).

To summarize, the FET device exhibits a sensitivity for increasing antibody concentrations. Mixed with AMX however, the effects are overlaying and the initial antibody concentration might have been so high that most of the surface area was already covered and thus lost its sensitivity for further molecules in solution. Thus it will be necessary to probe whether optimization of the fixed antibody concentration in the inverse competition assay improves the concentration curve and allows for AMX sensing in solution. The setup will then be suitable especially for low AMX concentrations, as the influence of AMX in solution on the transfer curves will be negligible in contrast to the distinct shift effected by 40  $\mu$ M AMX and compared to the shift caused by the antibodies. Further measurements were not possible within this thesis due to the little availability of chips as they are still produced on the lab scale. The results however can be taken as a first framing of the experimental conditions.

## Summary and Outlook

The preparation of surfaces and the choice of linker molecules are crucial for a successful receptor attachment. A robust biochemical functionalization while maintaining the receptor activity towards the target molecule is demonstrated in this thesis for silicon dioxide surfaces. The subsequent biorecognition was detected using optical and electrochemical methods.

Covalent functionalization strategies to link amino-terminated receptors were investigated in detail. This functional group of the selected receptors formed stable bonds with both carboxy- and epoxy-terminated surfaces, respectively.

Additionally, non-covalent functionalization of silicon nanowires was probed to produce highly concentrated aqueous solutions of silicon nanowires (SiNW) wrapped in lipid bilayer shells as tools for bionanotechnology. The lipid bilayers show an excellent mobility on the curved substrates of the freely dispersed SiNWs which was indicated by successful recovery tests [84]. Prior to this, only recovery tests on nanotubes and -wires on solid supports were carried out.

Two receptor-analyte combinations were chosen – namely an aptamer against the protein human  $\alpha$ -thrombin as well as an antibody against the small drug molecule amoxicillin (AMX). To characterize the individual modification steps from the start, a tool set of methods was demonstrated ranging from contact angle measurements to fluorescence microscopy. Most methods were carried out on planar glass or silicon wafer substrates. This allowed for investigation of functionalization strategies independently from the sensor platform development. Imaging of the functionalized areas was simplified by introducing micropatterning techniques – microcontact printing and nanoplotting. From modified to reference surfaces a clear difference was obviously present. This allowed to confirm the selective covalent attachment of the receptors. To prove their functionality after immobilization, the interaction with the analyte was probed.

For thrombin, a sandwich assay with two different aptamers was applied onto the patterned surfaces. The second aptamer was labeled with a red dye for visualization with fluorescence microscopy. After optimization of the participating layers and the blocking procedure, the fluorescence-to-background ratio was analyzed. By this, a concentration curve detecting thrombin down to 20 pM was achieved for both surface patterning techniques. This pushes the limit of detection of recent publications on similar assays further down [167]. The combination of layer optimization, parallel presence of modified and control areas as well as the dual thrombin recognition leads to a highly specific assay with low detection limit. In addition, no protein labeling is required. As disease thrombin levels are in the pM range in contrast to healthy levels in the nM to  $\mu$ M range, this setup might allow to distinguish between them [163].

The detection strategy for amoxicillin was an inverse competition assay. For this, AMX was attached on the surface and the antibodies were deposited onto the immobilized drug molecules. SEM investigation using gold nanoparticle labeling of a secondary antibody confirmed a concentration dependent coverage with particles.

The protocols were transferred and adapted to achieve the final goal, the realization of biosensing experiments on silicon nanowire field-effect transistors (FET). Due to the high surface-to-volume ratio, these devices are sensitive down to the molecular level. The integration of nanomaterial would also allow for miniaturization for the goal of portable and CMOS compatible sensors. Two types of FETs were tested with bottom-up grown and top-down fabricated NWs for thrombin and AMX detection, respectively. First device characterizations demonstrated the high sensitivity towards changes in the surface chemistry in a constant manner for one type of modification. Altering the flow rate and ionic strength of pumped solutions showed that these parameters have to be balanced to avoid signals which could interfere with the actual measurement. To prevent leakage, surface passivation was necessary when working in liquid environments. Due to the  $\text{Al}_2\text{O}_3$  passivation, the bottom-up SiNW FET exhibits an excellent pH sensitivity close to the Nernst limit [201].

Aptamers might be well suited for implementation in these transistors because of their small size as the sensitivity is highest close to the surface. Thus, sensors can be run in more stable environments while maintaining sensitivity for biorecognition events. Thrombin detection was tested on both the aptamer and a scrambled DNA sequence acting as a control. A clearly higher signal of the voltage shifts per injected concentrations at a fixed current is present for the aptamer proving the specificity on the bottom-up SiNW FET. To avoid higher fractions of unspecific adsorption, the investigation of blocking was started but needs to be studied further.

The top-down SiNW FET is sensitive for increasing antibody concentrations which proved the success of the simplified inverse assay. The inverse competition assay however requires further testing of the antibody concentration. Antibody and AMX solutions seem to influence each other leading to a constant signal instead of an AMX-concentration dependent voltage shift.

Within this thesis it could be demonstrated that the bottom-up SiNW FET chips show a sensitivity for thrombin in the pM range which is comparable to the values of recent aptamer-FET publications [3, 20]. More generally speaking, the technique demonstrates the ability to detect biorecognition events in real-time and without labeling. To realize a biosensor, further development will be necessary in the future. The aspects explained in the next paragraphs will be important for follow-up research.

Combining the here presented patterning techniques with the FETs, the chips can be functionalized in manifold ways for the goal of multiplexed detection of various analytes at the same time. Integration of microfluidics for parallel delivery and mixing of different solutions is required. Bottom-up grown SiNWs are feasible for integration on flexible substrates which reduces costs and opens up more potential application fields of the sensor, *e.g.* on the human skin. Such flexible devices are currently under investigation in our group. To realize an instant readout as well as portability and easy handling are essential for a future goal like point-of-care diagnostics. Thus, wire-bonding and packaging technology for the bottom-up SiNW FET are currently developed by IAVT, TU Dresden.

---

To achieve more stable conditions during measurement, *i.e.* to reduce pumping influences, the ionic strength and flow rate require optimization. Automated determination of the most sensitive region of the device characteristics (I-V curve) will be a possibility to measure voltage shifts as a readout signal.

Aptasensor development is interesting because of the listed advantages over antibodies. In terms of FETs, their small size is however a key features when aiming at low detection limits. Thus, the combination of aptamers with the detection of charged target molecules on SiNW FET sensors is promising.



# Bibliography

- [1] F. Patolsky, G. Zheng, and C. Lieber: *Nanowire sensors for medicine and the life sciences*, *Nanomedicine* **1** (2006), 51–65.
- [2] K. Odenthal and J. Gooding: *An introduction to electrochemical DNA biosensors*, *Analyst* **132** (2007), 603–610.
- [3] M. L. Hammock, O. Knopfmacher, B. D. Naab, J. B.-H. Tok, and Z. Bao: *Investigation of protein detection parameters using nanofunctionalized organic field-effect transistors.*, *ACS Nano* **7** (2013), 3970–3980.
- [4] T. Rim, K. Kim, N. Hong, W. Ko, C.-K. Baek, S. Jeon, M. J. Deen, M. Meyyappan, Y.-H. Jeong, and J.-S. Lee: *Investigation of the electrical stability of Si-nanowire biologically sensitive field-effect transistors with embedded Ag/AgCl pseudo reference electrode*, *RSC Advances* **3** (2013), 7963–7969.
- [5] A. Lamm, I. Gozlan, A. Rotstein, and D. Avisar: *Detection of amoxicillin-diketopiperazine-2', 5' in wastewater samples*, *Journal of Environmental Science and Health, Part A* **44** (2009), 1512–1517.
- [6] R. Babington, S. Matas, M.-P. Marco, and R. Galve: *Current bioanalytical methods for detection of penicillins.*, *Analytical and Bioanalytical Chemistry* **403** (2012), 1549–1566.
- [7] Y. Cui, Q. Wei, H. Park, and C. M. Lieber: *Nanowire nanosensors for highly sensitive and selective detection of biological and chemical species*, *Science* **293** (2001), 1289–1292.
- [8] J. Hahm and C. M. Lieber: *Direct ultrasensitive electrical detection of DNA and DNA sequence variations using nanowire nanosensors*, *Nano Letters* **4** (2004), 51–54.
- [9] F. Patolsky, G. Zheng, O. Hayden, M. Lakadamyali, X. Zhuang, and C. Lieber: *Electrical detection of single viruses*, *Proceedings of the National Academy of Sciences of the United States of America* **101** (2004), 14017.
- [10] F. Patolsky, G. Zheng, and C. M. Lieber: *Nanowire-based biosensors.*, *Analytical Chemistry* **78** (2006), 4260–4269.
- [11] Z. Jiang, Q. Qing, P. Xie, R. Gao, and C. M. Lieber: *Kinked pn junction nanowire probes for high spatial resolution sensing and intracellular recording*, *Nano Letters* **12** (2012), 1711–1716.

- [12] R. Elnathan, M. Kwiat, A. Pevzner, Y. Engel, L. Burstein, A. Khatchourints, A. Lichtenstein, R. Kantaev, and F. Patolsky: *Biorecognition layer engineering: overcoming screening limitations of nanowire-based FET devices*, Nano Letters **12** (2012), 5245–5254.
- [13] G. Zhang, J. Chua, R. Chee, A. Agarwal, S. Wong, K. Buddhharaju, and N. Balasubramanian: *Highly sensitive measurements of PNA-DNA hybridization using oxide-etched silicon nanowire biosensors*, Biosensors and Bioelectronics **23** (2008), 1701–1707.
- [14] E. Stern, R. Wagner, F. J. Sigworth, R. Breaker, T. M. Fahmy, and M. A. Reed: *Importance of the Debye Screening Length on Nanowire Field Effect Transistor Sensors*, Nano Letters **7** (2007), 3405–3409.
- [15] C. Hsiao, C. Lin, C. Hung, C. Su, and Y. Lo: *Novel poly-silicon nanowire field effect transistor for biosensing application*, Biosensors and Bioelectronics **24** (2009), 1223–1229.
- [16] A. D. Ellington and J. W. Szostak: *In vitro selection of RNA molecules that bind specific ligands.*, Nature **346** (1990), 818–822.
- [17] M. Menger, J. Glökler, and M. Rimmel: *Application of aptamers in therapeutics and for small-molecule detection.*, Handbook of experimental pharmacology (2006), 359–373.
- [18] A. Wochner, M. Menger, D. Orgel, B. Cech, M. Rimmel, V. A. Erdmann, and J. Glökler: *A DNA aptamer with high affinity and specificity for therapeutic anthracyclines.*, Analytical Biochemistry **373** (2008), 34–42.
- [19] M. Khati: *The future of aptamers in medicine*, Journal of Clinical Pathology **63** (2010), 480–487.
- [20] K. Kim, H. Lee, J. Yang, M. Jo, and S. Hahn: *The fabrication, characterization and application of aptamer-functionalized Si-nanowire FET biosensors*, Nanotechnology **20** (2009), 235501.
- [21] H. Lee, K. Kim, C. Kim, S. Hahn, and M. Jo: *Electrical detection of VEGFs for cancer diagnoses using anti-vascular endothelial growth factor aptamer-modified Si nanowire FETs*, Biosensors and Bioelectronics **24** (2009), 1801–1805.
- [22] C. K. O’Sullivan: *Aptasensors—the future of biosensing?*, Analytical and Bioanalytical Chemistry **372** (2002), 44–48.
- [23] L. C. Bock, L. C. Griffin, J. A. Latham, E. H. Vermaas, and J. J. Toole: *Selection of single-stranded DNA molecules that bind and inhibit human thrombin.*, Nature **355** (1992), 564–566.
- [24] M. Tsiang, C. S. Gibbs, L. C. Griffin, K. E. Dunn, and L. L. Leung: *Selection of a suppressor mutation that restores affinity of an oligonucleotide inhibitor for thrombin using in vitro genetics.*, Journal of Biological Chemistry **270** (1995), 19370–19376.



- [25] D. M. Tasset, M. F. Kubik, and W. Steiner: *Oligonucleotide inhibitors of human thrombin that bind distinct epitopes1*, *Journal of Molecular Biology* **272** (1997), 688–698.
- [26] J. P. Chambers, B. P. Arulanandam, L. L. Matta, A. Weis, and J. J. Valdes: *Biosensor Recognition Elements*, *Current Issues in Molecular Biology* **10** (2008), 1–12.
- [27] M. Zourob: *Recognition Receptors in Biosensors*, (Springer, New York Dordrecht Heidelberg London), 1st edn., (2010).
- [28] J. Wang: *Electrochemical biosensors: towards point-of-care cancer diagnostics*, *Biosensors and Bioelectronics* **21** (2006), 1887–1892.
- [29] M. Velasco-Garcia and S. Missailidis: *New trends in aptamer-based electrochemical biosensors*, *Gene Therapy and Molecular Biology* **13** (2009), 1–10.
- [30] E. Baldrich: *Aptamers: Versatile Tools for Reagentless Aptasensing*, in: *Recognition Receptors in Biosensors* (Ed. M. Zourob), 675–722, (Springer, New York Dordrecht Heidelberg London), (2010).
- [31] I. Willner and B. Willner: *Biomolecule-Based Nanomaterials and Nanostructures*, *Nano Letters* **10** (2010), 3805–3815.
- [32] R. Caygill and G. Blair: *A review on viral biosensors to detect human pathogens*, *Analytica Chimica Acta* **681** (2010), 8–15.
- [33] B. Chang: *Electrochemical Impedance Spectroscopy*, *Annual Review of Analytical Chemistry* **3** (2010), 207–229.
- [34] R. L. Rich and D. G. Myszka: *Survey of the 2009 commercial optical biosensor literature*, *Journal of Molecular Recognition* **24** (2011), 892–914.
- [35] J. Wang: *Electrochemical Glucose Biosensors*, *Chemical Reviews* **108** (2008), 814–825.
- [36] G. Lehoucq: *Transistors à nanofils de silicium top-down. Application à la détection biologique.*, Ph.D. thesis, École Polytechnique ParisTech, Paris, (2010).
- [37] M. Curreli, R. Zhang, F. N. Ishikawa, H.-K. Chang, R. J. Cote, C. Zhou, and M. E. Thompson: *Real-Time, Label-Free Detection of Biological Entities Using Nanowire-Based FETs*, *IEEE Transactions on Nanotechnology* **7** (2008), 651–667.
- [38] Z. Gao, A. Agarwal, A. Trigg, N. Singh, C. Fang, C. Tung, Y. Fan, K. Buddharaju, and J. Kong: *Silicon nanowire arrays for label-free detection of DNA*, *Analytical Chemistry* **79** (2007), 3291–3297.
- [39] A. Gao, N. Lu, P. Dai, T. Li, H. Pei, X. Gao, Y. Gong, Y. Wang, and C. Fan: *Silicon nanowire-based CMOS-compatible field-effect transistor nanosensors for ultrasensitive electrical detection of nucleic acids-Supproting info*, *Nano Letters* **11** (2011), 3974–3978.

- [40] G. Zhang, Z. Luo, M. Huang, G. K. I. Tay, and E. A. Lim: *Morpholino-functionalized silicon nanowire biosensor for sequence-specific label-free detection of DNA*, *Biosensors and Bioelectronics* **25** (2010), 2447–2453.
- [41] K. Kahn and K. W. Plaxco: *Principles of Biomolecular Recognition*, in: *Recognition Receptors in Biosensors* (Ed. M. Zourob), 3–46, (Springer, New York Dordrecht Heidelberg London), (2010).
- [42] N. M. Green: *Avidin.*, *Advances in Protein Chemistry* **29** (1975), 85–133.
- [43] A. C. Donahue and M. Albitar: *Antibodies in Biosensing*, in: *Recognition Receptors in Biosensors* (Ed. M. Zourob), 221–248, (Springer Science +Business Media, New York Dordrecht Heidelberg London), (2009).
- [44] A. Casadevall, E. Dadachova, and L.-a. Pirofski: *Passive antibody therapy for infectious diseases*, *Nature Reviews Microbiology* **2** (2004), 695–703.
- [45] R. L. Wimalasena and G. S. Wilson: *Factors affecting the specific activity of immobilized antibodies and their biologically active fragments.*, *Journal of Chromatography* **572** (1991), 85–102.
- [46] B. Lu, M. R. Smyth, and R. O’Kennedy: *Tutorial review. Oriented immobilization of antibodies and its applications in immunoassays and immunosensors*, *Analyst* **121** (1996), 29R–32R.
- [47] E. Baldrich, A. Restrepo, and C. O’Sullivan: *Aptasensor development: elucidation of critical parameters for optimal aptamer performance*, *Analytical Chemistry* **76** (2004), 7053–7063.
- [48] S. C. B. Gopinath: *Methods developed for SELEX.*, *Analytical and Bioanalytical Chemistry* **387** (2007), 171–182.
- [49] I. Russo Krauss, A. Merlino, A. Randazzo, E. Novellino, L. Mazzarella, and F. Sica: *High-resolution structures of two complexes between thrombin and thrombin-binding aptamer shed light on the role of cations in the aptamer inhibitory activity.*, *Nucleic Acids Research* **40** (2012), 8119–8128.
- [50] R. Stoltenburg, N. Nikolaus, and B. Strehlitz: *Capture-SELEX: Selection of DNA Aptamers for Aminoglycoside Antibiotics.*, *Journal of Analytical Methods in Chemistry* **2012** (2012), 415697.
- [51] J. J. Toulmé, J. P. Daguer, and E. Dauss: *Aptamers: Ligands for all reasons*, in: *Aptamers in Bioanalysis* (Ed. M. Mascini), 3–30, (John Wiley & Sons, Hoboken, New Jersey), (2009).
- [52] University of Southern Denmark: [www.sdu.dk/en/Om\\_SDU/Institutter\\_centre/C\\_Evolna/Background](http://www.sdu.dk/en/Om_SDU/Institutter_centre/C_Evolna/Background) (last checked: 11.02.2014): *EVOLNA Background* (2012).
- [53] L. Li, B. Li, Y. Qi, and Y. Jin: *Label-free aptamer-based colorimetric detection of mercury ions in aqueous media using unmodified gold nanoparticles as colorimetric probe.*, *Analytical and Bioanalytical Chemistry* **393** (2009), 2051–2057.

- [54] M. S. L. Raddatz, A. Dolf, E. Endl, P. Knolle, M. Famulok, and G. Mayer: *Enrichment of Cell-Targeting and Population-Specific Aptamers by Fluorescence-Activated Cell Sorting*, *Angewandte Chemie* **120** (2008), 5268–5271.
- [55] S. Balamurugan, A. Obubuafo, R. L. McCarley, S. A. Soper, and D. A. Spivak: *Effect of Linker Structure on Surface Density of Aptamer Monolayers and Their Corresponding Protein Binding Efficiency*, *Analytical Chemistry* **80** (2008), 9630–9634.
- [56] Y.-H. Lao, K. Peck, and L.-C. Chen: *Enhancement of Aptamer Microarray Sensitivity through Spacer Optimization and Avidity Effect*, *Analytical Chemistry* **81** (2009), 1747–1754.
- [57] M. Lee and D. R. Walt: *A fiber-optic microarray biosensor using aptamers as receptors.*, *Analytical Biochemistry* **282** (2000), 142–146.
- [58] A. Henseleit, S. Schmieder, T. Bley, F. Sonntag, N. Schilling, P. Quenzel, N. Danz, U. Klotzbach, and E. Boschke: *A compact and rapid aptasensor platform based on surface plasmon resonance*, *Engineering In Life Sciences* **11** (2011), 573–579.
- [59] P. Jonkheijm, D. Weinrich, H. Schröder, C. Niemeyer, and H. Waldmann: *Chemical Strategies for Generating Protein Biochips*, *Angewandte Chemie International Edition* **47** (2008), 9618–9647.
- [60] M. Mascini (ed.): *Aptamers in Bioanalysis*, (John Wiley & Sons, Hoboken, New Jersey), 1st edn., (2009).
- [61] S. Klussmann, A. Nolte, R. Bald, V. A. Erdmann, and J. P. Fürste: *Mirror-image RNA that binds D-adenosine.*, *Nature Biotechnology* **14** (1996), 1112–1115.
- [62] P. Schultze, R. Macaya, and J. Feigon: *Three-dimensional solution structure of the thrombin-binding DNA aptamer d (GGTTGGTGTGGTTGG)*, *Journal of Molecular Biology* (1994).
- [63] H. Cai, T. Lee, and I. Hsing: *Label-free protein recognition using an aptamer-based impedance measurement assay*, *Sensors and Actuators B* **114** (2006), 433–437.
- [64] Y. Xu, L. Yang, X. Ye, P. He, and Y. Fang: *An aptamer-based protein biosensor by detecting the amplified impedance signal*, *Electroanalysis* **18** (2006), 1449–1456.
- [65] T. Hianik, V. Ostatna, Z. Zajacova, E. Stoikova, and G. Evtugyn: *Detection of aptamer-protein interactions using QCM and electrochemical indicator methods*, *Bioorganic & Medicinal Chemistry Letters* **15** (2005), 291–295.
- [66] L. Paborsky, S. McCurdy, L. Griffin, J. Toole, and L. Leung: *The single-stranded DNA aptamer-binding site of human thrombin.*, *Journal of Biological Chemistry* **268** (1993), 20808–20811.
- [67] W. Liao and X. T. Cui: *Reagentless aptamer based impedance biosensor for monitoring a neuro-inflammatory cytokine PDGF*, *Biosensors and Bioelectronics* **23** (2007), 218–224.

- [68] T. Chiu: *Aptamer-Functionalized Nano-Biosensors*, *Sensors* (2009).
- [69] T. An, K. Kim, S. Hahn, and G. Lim: *Real-time, step-wise, electrical detection of protein molecules using dielectrophoretically aligned SWNT-film FET aptasensors*, *Lab on a Chip* **10** (2010), 2052–2056.
- [70] X. Wang, Y. Ishii, A. R. Ruslinda, M. Hasegawa, and H. Kawarada: *Effective Surface Functionalization of Nanocrystalline Diamond Films by Direct Carboxylation for PDGF Detection via Aptasensor*, *ACS Applied Materials & Interfaces* **4** (2012), 3526–3534.
- [71] S. D. Jayasena: *Aptamers: an emerging class of molecules that rival antibodies in diagnostics*, *Clinical Chemistry* **45** (1999), 1628–1650.
- [72] K. Han, Z. Liang, and N. Zhou: *Design Strategies for Aptamer-Based Biosensors*, *Sensors* **10** (2010), 4541–4557.
- [73] Z.-S. Wu, F. Zheng, G.-L. Shen, and R.-Q. Yu: *A hairpin aptamer-based electrochemical biosensing platform for the sensitive detection of proteins*, *Biomaterials* **30** (2009), 2950–2955.
- [74] M. Crawford and R. Woodman: *Peptide aptamers: tools for biology and drug discovery*, *Briefings in Functional Genomics and Proteomics* **2** (2003), 72–79.
- [75] S. Cabilly: *The Basic Structure of Filamentous Phage and its Use in the Display of Combinatorial Peptide Libraries*, *Molecular Biotechnology* **12** (1999), 143–148.
- [76] J. Collins, N. Horn, J. Wadenbäck, and M. Szardenings: *Cosmix-plexing: a novel recombinatorial approach for evolutionary selection from combinatorial libraries.*, *Journal of Biotechnology* **74** (2001), 317–338.
- [77] M. Mejri, H. Baccar, and E. Baldrich: *Impedance biosensing using phages for bacteria detection: Generation of dual signals as the clue for in-chip assay confirmation*, *Biosensors and Bioelectronics* (2010).
- [78] K. Butz, C. Denk, B. Fitscher, and I. Crnkovic-Mertens: *Peptide aptamers targeting the hepatitis B virus core protein: a new class of molecules with antiviral activity.*, *Oncogene* (2001).
- [79] J. Morton, N. Karoonuthaisiri, R. Charlermroj, L. D. Stewart, C. T. Elliott, and I. R. Grant: *Phage Display-Derived Binders Able to Distinguish *Listeria monocytogenes* from Other *Listeria* Species.*, *PloS one* **8** (2013), e74312.
- [80] S. Kober, G. Gotesman, and R. Naaman: *Surprising Molecular Length Dependence in Conduction through a Hybrid Organic–Inorganic System*, *The Journal of Physical Chemistry Letters* **4** (2013), 2041–2045.
- [81] R. Chelmoski: *Proteinchemie an Oberflächen*, Ph.D. thesis, Universität Bochum, Bochum, (2008).

- [82] R. P. Richter, R. Bérat, and A. R. Brisson: *Formation of solid-supported lipid bilayers: an integrated view*, *Langmuir* **22** (2006), 3497–3505.
- [83] N. Misra, J. Martinez, S. Huang, Y. Wang, P. Stroeve, C. Grigoropoulos, and A. Noy: *Bioelectronic silicon nanowire devices using functional membrane proteins*, *Proceedings of the National Academy of Sciences* **106** (2009), 13780.
- [84] L. Römhildt, A. Gang, L. Baraban, J. Opitz, and G. Cuniberti: *High yield formation of lipid bilayer shells around silicon nanowires in aqueous solution*, *Nanotechnology* **24** (2013), 355601.
- [85] F. Höök, A. Ray, B. Norden, and B. Kasemo: *Characterization of PNA and DNA immobilization and subsequent hybridization with DNA using acoustic-shear-wave attenuation measurements*, *Langmuir* **17** (2001), 8305–8312.
- [86] D. Bavli, M. Tkachev, H. Piwonski, E. Capua, I. d. Albuquerque, D. Bensimon, G. Haran, and R. Naaman: *Detection and Quantification through a Lipid Membrane Using the Molecularly Controlled Semiconductor Resistor*, *Langmuir* **28** (2012), 1020–1028.
- [87] B. Tian, T. Cohen-Karni, Q. Qing, X. Duan, P. Xie, and C. M. Lieber: *Three-dimensional, flexible nanoscale field-effect transistors as localized bioprobes.*, *Science* **329** (2010), 830–834.
- [88] X. Duan, R. Gao, P. Xie, T. Cohen-Karni, Q. Qing, H. S. Choe, B. Tian, X. Jiang, and C. M. Lieber: *Intracellular recordings of action potentials by an extracellular nanoscale field-effect transistor.*, *Nature Nanotechnology* **7** (2012), 174–179.
- [89] V. Petrák, L. Grieten, A. Taylor, F. Fendrych, M. Ledvina, S. D. Janssens, M. Nešládek, K. Haenen, and P. Wagner: *Monitoring of peptide induced disruption of artificial lipid membrane constructed on boron-doped nanocrystalline diamond by electrochemical impedance spectroscopy*, *Physica Status Solidi A* **208** (2011), 2099–2103.
- [90] J. Liu, X. Jiang, C. Ashley, and C. J. Brinker: *Electrostatically mediated liposome fusion and lipid exchange with a nanoparticle-supported bilayer for control of surface charge, drug containment, and delivery*, *Journal of the American Chemical Society* **131** (2009), 7567–7569.
- [91] C. E. Ashley, E. C. Carnes, G. K. Phillips, D. Padilla, P. N. Durfee, P. A. Brown, T. N. Hanna, J. Liu, B. Phillips, M. B. Carter, N. J. Carroll, X. Jiang, D. R. Dunphy, C. L. Willman, D. N. Petsev, D. G. Evans, A. N. Parikh, B. Chackerian, W. Wharton, D. S. Peabody, and C. J. Brinker: *The targeted delivery of multicomponent cargos to cancer cells by nanoporous particle-supported lipid bilayers*, *Nature Materials* **10** (2011), 389–397.
- [92] M. Goutayer, S. Dufort, V. Jossierand, A. Royère, E. Heinrich, F. Vinet, J. Bibette, J.-L. Coll, and I. Texier: *Tumor targeting of functionalized lipid nanoparticles: Assessment by in vivo fluorescence imaging*, *European Journal of Pharmaceutics and Biopharmaceutics* **75** (2010), 11–11.

- [93] X. Zhou, J. Moran-Mirabel, H. Craighead, and P. McEuen: *Supported lipid bilayer/carbon nanotube hybrids*, Nature Nanotechnology **2** (2007), 185–190.
- [94] A. B. Artyukhin, A. Shestakov, J. Harper, O. Bakajin, P. Stroeve, and A. Noy: *Functional one-dimensional lipid bilayers on carbon nanotube templates*, Journal of the American Chemical Society **127** (2005), 7538–7542.
- [95] S. Huang, A. Artyukhin, J. Martinez, and D. Sirbully: *Formation, stability, and mobility of one-dimensional lipid bilayers on polysilicon nanowires*, Nano Letters **7** (2007), 3355–3359.
- [96] H. T. McMahon and J. L. Gallop: *Membrane curvature and mechanisms of dynamic cell membrane remodelling*, Nature **438** (2005), 590–596.
- [97] E. J. Cho, J. R. Collett, A. E. Szafranska, and A. D. Ellington: *Optimization of aptamer microarray technology for multiple protein targets.*, Analytica Chimica Acta **564** (2006), 82–90.
- [98] G. T. Hermanson: *Bioconjugated Techniques*, (Bioconjugate Techniques, Pierce Biotechnology, Thermo Fisher Scientific, Rockford, Illinois, USA), (2008).
- [99] C. D. Bain, E. B. Troughton, Y.-T. Tao, J. Evall, G. M. Whitesides, and R. G. Nuzzo: *Formation of monolayer films by the spontaneous assembly of organic thiols from solution onto gold*, Journal of the American Chemical Society **111** (1989), 321–335.
- [100] S. Onclin and B. Ravoo: *Engineering Silicon Oxide Surfaces Using Self-Assembled Monolayers*, Angewandte Chemie International edition **44** (2005), 6282–6304.
- [101] Gelest Inc.: [www.gelest.de/goods/pdf/couplingagents.pdf](http://www.gelest.de/goods/pdf/couplingagents.pdf) (last checked: 11.02.2014): *Silane coupling agents: connecting across boundaries* (2006), 1–60.
- [102] V. Dugas, A. Elaissari, and Y. Chevalier: *Surface Sensitization Techniques and Recognition Receptors Immobilization on Biosensors and Microarrays*, in: *Recognition Receptors in Biosensors* (Ed. M. Zourob), 47–134, (Springer, New York Dordrecht Heidelberg London), (2010).
- [103] R. Janissen, L. Oberbarnscheidt, and F. Oesterhelt: *Optimized straight forward procedure for covalent surface immobilization of different biomolecules for single molecule applications.*, Colloids and Surfaces B: Biointerfaces **71** (2009), 200–207.
- [104] F. Luderer and U. Walschus: *Immobilization of oligonucleotides for biochemical sensing by self-assembled monolayers: Thiol-organic bonding on gold and silanization on silica surfaces*, Immobilisation of DNA on Chips I **260** (2005), 37–56.
- [105] A. Tarasov: *Silicon Nanowire Field-effect Transistors for Sensing Applications*, Ph.D. thesis, Universität Basel, Basel, (2012).
- [106] P. Bergveld: *Development of an Ion-Sensitive Solid-State Device for Neurophysiological Measurements*, IEEE Transactions on Biomedical Engineering **BME-17** (1970), 70–71.

- [107] S. Chen, J. G. Bomer, E. T. Carlen, and A. van den Berg: *Al<sub>2</sub>O<sub>3</sub>/Silicon NanoISFET with Near Ideal Nernstian Response*, Nano Letters **11** (2011), 2334–2341.
- [108] D. Nozaki, J. Kunstmann, F. Zörgiebel, W. M. Weber, T. Mikolajick, and G. Cuniberti: *Multi-scale modeling of nanowire-based Schottky-barrier field-effect transistors for sensor applications*, Nanotechnology **22** (2011), 325703.
- [109] M. Meyyappan and M. K. Sunkara: *Inorganic Nanowires, Applications, Properties, and Characterization*, (CRC PressI Llc), (2010).
- [110] R. GhoshMoulick, X. T. Vu, S. Gilles, D. Mayer, A. Offenhaeusser, and S. Ingebrandt: *Impedimetric detection of covalently attached biomolecules on field-effect transistors*, Physica Status Solidi A **206** (2009), 417–425.
- [111] W. Weber, L. Geelhaar, A. Graham, E. Unger, G. Duesberg, M. Liebau, W. Pamler, C. Cheze, H. Riechert, and P. Lugli: *Silicon-nanowire transistors with intruded nickel-silicide contacts*, Nano Letters **6** (2006), 2660–2666.
- [112] S. Pregl, W. M. Weber, D. Nozaki, J. Kunstmann, L. Baraban, T. Mikolajick, and G. Cuniberti: *Parallel arrays of Schottky barrier nanowire field effect transistors: Nanoscopic effects for macroscopic current output*, Nano Research **6** (2013), 381–388.
- [113] W. Weber, L. Geelhaar, E. Unger, C. Cheze, F. Kreupl, H. Riechert, and P. Lugli: *Silicon to nickel-silicide axial nanowire heterostructures for high performance electronics*, physica status solidi (b) (2007).
- [114] K.-S. Shin, A. Pan, and C. On Chui: *Channel length dependent sensitivity of Schottky contacted silicon nanowire field-effect transistor sensors*, Applied Physics Letters **100** (2012), 123504.
- [115] D. Martin, A. Heinzig, M. Grube, L. Geelhaar, T. Mikolajick, H. Riechert, and W. M. Weber: *Direct probing of Schottky barriers in Si nanowire Schottky barrier field effect transistors.*, Physical Review Letters **107** (2011), 216807.
- [116] S. Kim, T. Rim, K. Kim, U. Lee, E. Baek, H. Lee, C.-K. Baek, M. Meyyappan, M. J. Deen, and J.-S. Lee: *Silicon nanowire ion sensitive field effect transistor with integrated Ag/AgCl electrode: pH sensing and noise characteristics.*, Analyst **136** (2011), 5012–5016.
- [117] A. Nerowski, M. Poetschke, M. Bobeth, J. Opitz, and G. Cuniberti: *Dielectrophoretic growth of platinum nanowires: concentration and temperature dependence of the growth velocity.*, Langmuir **28** (2012), 7498–7504.
- [118] A. Nerowski, J. Opitz, L. Baraban, and G. Cuniberti: *Bottom-up synthesis of ultrathin straight platinum nanowires: Electric field impact*, Nano Research (2013), 1–9.
- [119] A. Nerowski: *Electrochemical metal nanowire growth from solution*, Ph.D. thesis, TU Dresden, Dresden, (2013).

- [120] R. S. Wagner and W. C. Ellis: *Vapor-liquid-solid mechanism of single crystal growth*, Applied Physical Letters **4** (1964), 89–90.
- [121] Y. Cui, L. J. Lauhon, M. S. Gudixsen, J. Wang, and C. M. Lieber: *Diameter-controlled synthesis of single-crystal silicon nanowires*, Applied Physical Letters **78** (2001), 2214–2216.
- [122] S. Pregl, L. Römhildt, W. M. Weber, L. Baraban, J. Opitz, T. Mikolajik, and G. Cuniberti: *Investigations on the sensing mechanisms in silicon nanowire Schottky-barrier field effect sensors*, Proceedings of IMCS 2012 – The 14th International Meeting on Chemical Sensors (2012), 994–996.
- [123] B. Wang, T. Stelzner, R. Dirawi, O. Assad, N. Shehada, S. Christiansen, and H. Haick: *Field-effect transistors based on silicon nanowire arrays: effect of the good and the bad silicon nanowires.*, ACS Applied Materials & Interfaces **4** (2012), 4251–4258.
- [124] Z. Fan, J. C. Ho, Z. A. Jacobson, R. Yerushalmi, R. L. Alley, H. Razavi, and A. Javey: *Wafer-scale assembly of highly ordered semiconductor nanowire arrays by contact printing.*, Nano Letters **8** (2008), 20–25.
- [125] C. H. Lee, D. R. Kim, and X. Zheng: *Fabricating nanowire devices on diverse substrates by simple transfer-printing methods.*, Proceedings of the National Academy of Sciences **107** (2010), 9950–9955.
- [126] J. Yao, H. Yan, and C. M. Lieber: *A nanoscale combing technique for the large-scale assembly of highly aligned nanowires*, Nature Nanotechnology **8** (2013), 329–335.
- [127] S. Jin, D. Whang, M. C. McAlpine, R. S. Friedman, Y. Wu, and C. M. Lieber: *Scalable Interconnection and Integration of Nanowire Devices without Registration*, Nano Letters **4** (2004), 915–919.
- [128] D. Wang, Y.-L. Chang, Z. Liu, and H. Dai: *Oxidation resistant germanium nanowires: bulk synthesis, long chain alkanethiol functionalization, and Langmuir-Blodgett assembly.*, Journal of the American Chemical Society **127** (2005), 11871–11875.
- [129] B.-R. Li, C.-W. Chen, W.-L. Yang, T.-Y. Lin, C.-Y. Pan, and Y.-T. Chen: *Biomolecular recognition with a sensitivity-enhanced nanowire transistor biosensor.*, Biosensors and Bioelectronics **45C** (2013), 252–259.
- [130] S. Schumacher, D. Sartorius, and E. E. Förster: *Miniaturization for point-of-care analysis: platform technology for almost every biomedical assay*, The Journal of the International Federation of Clinical Chemistry and Laboratory Medicine **23** (2012), 1–6.
- [131] Z. Li, Y. Chen, X. Li, T. Kamins, K. Nauka, and R. Williams: *Sequence-specific label-free DNA sensors based on silicon nanowires*, Nano Letters **4** (2004), 245–247.



- [132] T. Rim, K. Kim, S. Kim, and C. K. Baek: *Improved Electrical Characteristics of Honeycomb-Nanowire ISFETs*, IEEE Electron Device Letters **34** (2013), 1059–1061.
- [133] C. W. Park, C. S. Ah, C.-G. Ahn, J.-H. Yang, A. Kim, T.-Y. Kim, and G. Y. Sung: *Analysis of configuration of surface-immobilized proteins by Si nanochannel field effect transistor biosensor*, Sensors And Actuators B-Chemical **154** (2011), 164–168.
- [134] Y. Bunimovich, Y. Shin, W. Yeo, and M. Amori: *Quantitative real-time measurements of DNA hybridization with alkylated nonoxidized silicon nanowires in electrolyte solution*, Journal of the American Chemical Society **128** (2006), 16323–16331.
- [135] M. Y. Bashouti, K. Sardashti, S. W. Schmitt, M. Pietsch, J. Ristein, H. Haick, and S. H. Christiansen: *Oxide-free hybrid silicon nanowires: From fundamentals to applied nanotechnology*, Progress in Surface Science **88** (2013), 39–60.
- [136] M. Zayats, Y. Huang, R. Gill, C.-a. Ma, and I. Willner: *Label-free and reagentless aptamer-based sensors for small molecules.*, Journal of the American Chemical Society **128** (2006), 13666–13667.
- [137] S. Ek, E. Iiskola, L. Niinistö, J. Vaittinen, and T. Pakkanen: *Atomic layer deposition of a high-density aminopropylsiloxane network on silica through sequential reactions of gamma-aminopropyltrialkoxysilanes and water*, Langmuir **19** (2003), 10601–10609.
- [138] S. Taylor, S. Smith, B. Windle, and A. Guiseppi: *Impact of surface chemistry and blocking strategies on DNA microarrays*, Nucleic Acids Research **31** (2003), 1–19.
- [139] R. Benters, C. Niemeyer, and D. Wöhrle: *Dendrimer-activated solid supports for nucleic acid and protein microarrays*, ChemBioChem **2** (2001), 686–694.
- [140] D. Janssen, R. De Palma, S. Verlaak, and P. Heremans: *Static solvent contact angle measurements, surface free energy and wettability determination of various self-assembled monolayers on silicon dioxide*, Thin Solid Films **515** (2006), 1433–1438.
- [141] S. C. Gopinath, K. Awazu, M. Fujimaki, K. Shimizu, W. Mizutani, and K. Tsukagoshi: *Surface functionalization chemistry on highly sensitive silica-based sensor chips*, Analyst **137** (2012), 3520–3527.
- [142] S. Gilles: *Chemical modification of silicon surfaces for the application in soft lithography*, Ph.D. thesis, FZ Jülich, Jülich, (2007).
- [143] K. Choi, J. Bourgoïn, S. Auvray, and D. Esteve: *Controlled deposition of carbon nanotubes on a patterned substrate*, Surface Science **462** (2000), 195–202.
- [144] A. Kumar and G. M. Whitesides: *Features of gold having micrometer to centimeter dimensions can be formed through a combination of stamping with an elastomeric stamp and an alkanethiol “ink” followed by chemical etching*, Applied Physics Letters **63** (1993), 2002–2004.

- [145] Y. Xia and G. M. Whitesides: *Soft lithography*, Annual Reviews of Materials Science **28** (1998), 153–184.
- [146] D. J. Lipomi, R. V. Martinez, L. Cademartiri, and G. M. Whitesides: *Soft Lithographic Approaches to Nanofabrication*, in: *Polymer Science: A Comprehensive Reference* (Eds. K. Matyjaszewski and M. Möller), 211–230, (Elsevier B.V., Amsterdam Oxford Waltham), (2012).
- [147] N. L. Jeon, K. Finnie, K. Branshaw, and R. G. Nuzzo: *Structure and Stability of Patterned Self-Assembled Films of Octadecyltrichlorosilane Formed by Contact Printing*, Langmuir **13** (1997), 3382–3391.
- [148] A. L. Briseno, S. C. B. Mannsfeld, M. M. Ling, S. Liu, R. J. Tseng, C. Reese, M. E. Roberts, Y. Yang, F. Wudl, and Z. Bao: *Patterning organic single-crystal transistor arrays*, Nature **444** (2006), 913–917.
- [149] G. Arslan, M. Özmen, I. Hatay, I. H. Gübbük, and M. Ersöz: *Microcontact Printing of an Alkylsilane Monolayer on the Surface of Glass*, Turkish Journal of Chemistry **32** (2008), 313–321.
- [150] M. Eisen and P. Brown: *DNA arrays for analysis of gene expression*, Methods of Enzymology **303** (1999), 179–205.
- [151] M. T. Stubbs and W. Bode: *A player of many parts: The spotlight falls on thrombin's structure*, Thrombosis Research **69** (1993), 1–58.
- [152] M. A. Shuman and P. W. Majerus: *The measurement of thrombin in clotting blood by radioimmunoassay.*, Journal of Clinical Investigation **58** (1976), 1249–1258.
- [153] S. Centi, S. Tombelli, M. Minunni, and M. Mascini: *Aptamer-Based Detection of Plasma Proteins by an Electrochemical Assay Coupled to Magnetic Beads*, Analytical Chemistry **79** (2007), 1466–1473.
- [154] K. Padmanabhan and A. Tulinsky: *An ambiguous structure of a DNA 15-mer thrombin complex.*, Acta Crystallographica. Section D, Biological Crystallography **52** (1996), 272–282.
- [155] Haematologic Technologies Inc.: [www.haemtech.com/enzymes/Factor%20Xa\\_Thrombin\\_Flyer.pdf](http://www.haemtech.com/enzymes/Factor%20Xa_Thrombin_Flyer.pdf) (last checked: 11.02.2014): *Thrombin and Factor Xa* (2008), 1–2.
- [156] Q. Tang, X. Su, and K. P. Loh: *Surface plasmon resonance spectroscopy study of interfacial binding of thrombin to antithrombin DNA aptamers.*, Journal of Colloid and Interface science **315** (2007), 99–106.
- [157] R. Kirby, E. J. Cho, B. Gehrke, T. Bayer, Y. S. Park, D. P. Neikirk, J. T. McDevitt, and A. D. Ellington: *Aptamer-based sensor arrays for the detection and quantitation of proteins*, Analytical Chemistry (2004).

- [158] U. Schlecht, A. Malave, T. Gronewold, M. Tewes, and M. Loehndorf: *Comparison of antibody and aptamer receptors for the specific detection of thrombin with a nanometer gap-sized impedance biosensor*, *Analytica Chimica Acta* **573** (2006), 65–68.
- [159] P. D. Patel: *ScienceDirect.com - TrAC Trends in Analytical Chemistry - (Bio)sensors for measurement of analytes implicated in food safety: a review*, *Trends in Analytical Chemistry* (2002).
- [160] J. R. L. Guerreiro, M. G. F. Sales, F. T. C. Moreira, and T. S. R. Rebelo: *Selective recognition in potentiometric transduction of amoxicillin by molecularly imprinted materials*, *European Food Research and Technology* **232** (2010), 39–50.
- [161] I. M. Scott, L. J. Kraft, J. D. Parker, K. Daniel, S. Kustick, D. Kennen, J. L. McMurry, and J. L. McMurry: *A real time optical biosensor assay for amoxicillin and other beta-lactams in water samples*, *Academy of Science* **68** (2010), 72.
- [162] S. Flink, F. C. J. M. van Veggel, and D. N. Reinhoudt: *Functionalization of self-assembled monolayers on glass and oxidized silicon wafers by surface reactions*, *J. Phys. Org. Chem.* **14** (2001), 407–415.
- [163] L. Römhildt, C. Pahlke, F. Zörgiebel, H.-G. Braun, J. Opitz, L. Baraban, and G. Cuniberti: *Patterned Biochemical Functionalization Improves Aptamer-Based Detection of Unlabeled Thrombin in a Sandwich Assay*, *ACS Applied Materials & Interfaces* **5** (2013), 12029–12035.
- [164] G. Sauerbrey: *Verwendung von Schwingquarzen zur Wägung dünner Schichten und zur Mikrowägung - Springer*, *Zeitschrift für Physik* (1959).
- [165] D. Huang, C. Niu, P. Qin, M. Ruan, and G. Zeng: *Time-resolved fluorescence aptamer-based sandwich assay for thrombin detection*, *Talanta* **83** (2010), 185–189.
- [166] A. Sobic, A. Meneghello, E. Cretaio, and B. Gatto: *Human Thrombin Detection Through a Sandwich Aptamer Microarray: Interaction Analysis in Solution and in Solid Phase*, *Sensors* **11** (2011), 9426–9441.
- [167] A. Meneghello, A. Sobic, A. Antognoli, E. Cretaio, and B. Gatto: *Development and Optimization of a Thrombin Sandwich Aptamer Microarray*, *Microarrays* **1** (2012), 95–106.
- [168] C. Daniel, F. Mélaïne, Y. Roupioz, T. Livache, and A. Buhot: *Real time monitoring of thrombin interactions with its aptamers: insights into the sandwich complex formation.*, *Biosensors and Bioelectronics* **40** (2013), 186–192.
- [169] F. Patolsky, G. Zheng, and C. Lieber: *Fabrication of silicon nanowire devices for ultrasensitive, label-free, real-time detection of biological and chemical species*, *Nature Protocols* **1** (2006), 1711–1724.

- [170] W. Liao, F. Wei, M. Qian, and X. Zhao: *Characterization of protein immobilization on alkyl monolayer modified silicon(111) surface*, *Sensors And Actuators B-Chemical* **101** (2004), 361–367.
- [171] J. S. Daniels and N. Pourmand: *Label-free impedance biosensors: Opportunities and challenges*, *Electroanalysis* **19** (2007), 1239–1257.
- [172] R. M. Penner: *Chemical Sensing with Nanowires*, *Annual Review of Analytical Chemistry* **5** (2012), 461–485.
- [173] N. A. Lapin and Y. J. Chabal: *Infrared Characterization of Biotinylated Silicon Oxide Surfaces, Surface Stability, and Specific Attachment of Streptavidin*, *Journal Of Physical Chemistry B* **113** (2009), 8776–8783.
- [174] Kim, J: [www.piketech.com/skin/fashion\\_mosaic\\_blue/application-pdfs/ProbingOrganicSelf-AssembledMonolayersSiliconFTIRSingleReflectanceATR.pdf](http://www.piketech.com/skin/fashion_mosaic_blue/application-pdfs/ProbingOrganicSelf-AssembledMonolayersSiliconFTIRSingleReflectanceATR.pdf) (11.02.2014): *Probing Organic Self-Assembled Monolayers (SAMS) on Silicon by FTIR with Single Reflectance ATR - PIKE Technologies* (2007), 1–2.
- [175] H. D. Kim and H. Ishida: *Hydrogen Bonding of Polybenzoxazines*, in: *Handbook of Benzoxazine Resins: Part III - Physical and Chemical Properties of Cross-Linked Polybenzoxazines* (Eds. H. Ishida and T. Agag), 712, (Elsevier, Oxford), (2011).
- [176] Z. Wu, H. Xiang, T. Kim, M.-S. Chun, and K. Lee: *Surface properties of submicrometer silica spheres modified with aminopropyltriethoxysilane and phenyltriethoxysilane*, *Journal of Colloid and Interface science* **304** (2006), 119–124.
- [177] U. Rabe: *Atomic Force Acoustic Microscopy*, in: *Applied Scanning Probe Methods II- Scanning Probe Microscopy Techniques* (Eds. B. Bushan and H. Fuchs), 37–90, (Springer-Verlag, Berlin Heidelberg New York), (2006).
- [178] J. Opitz, F. Braun, R. Seidel, W. Pompe, B. Voit, and M. Mertig: *Site-specific binding and stretching of DNA molecules at UV-light-patterned aminoterpolymer films*, *Nanotechnology* **15** (2004), 717–723.
- [179] S. S. Niu, L. L. Qu, Q. Q. Zhang, and J. J. Lin: *Fluorescence detection of thrombin using autocatalytic strand displacement cycle reaction and a dual-aptamer DNA sandwich assay*, *Analytical Biochemistry* **421** (2012), 6–6.
- [180] Y. H. Tennico, D. Hutanu, M. T. Koesdjojo, C. M. Bartel, and V. T. Remcho: *On-chip aptamer-based sandwich assay for thrombin detection employing magnetic beads and quantum dots.*, *Analytical Chemistry* **82** (2010), 5591–5597.
- [181] H. Huang and J.-J. Zhu: *DNA aptamer-based QDs electrochemiluminescence biosensor for the detection of thrombin.*, *Biosensors and Bioelectronics* **25** (2009), 927–930.

- [182] S. J. Lee, R. Tatavarty, and M. B. Gu: *Electrospun polystyrene-poly(styrene-co-maleic anhydride) nanofiber as a new aptasensor platform.*, Biosensors and Bioelectronics **38** (2012), 302–307.
- [183] S. C. Feifel and F. Lisdat: *Silica nanoparticles for the layer-by-layer assembly of fully electroactive cytochrome c multilayers*, Journal of Nanobiotechnology **9** (2011), 59.
- [184] C. Graf, Q. Gao, I. Schütz, C. N. Noufele, W. Ruan, U. Posselt, E. Korotianskiy, D. Nordmeyer, F. Rancan, S. Hadam, A. Vogt, J. Lademann, V. Haucke, and E. Rühl: *Surface functionalization of silica nanoparticles supports colloidal stability in physiological media and facilitates internalization in cells.*, Langmuir **28** (2012), 7598–7613.
- [185] V. S. Kulkarni, W. H. Anderson, and R. E. Brown: *Bilayer nanotubes and helical ribbons formed by hydrated galactosylceramides: acyl chain and headgroup effects*, Biophysical Journal **69** (1995), 1976–1986.
- [186] K. Heo, E. Cho, J. Yang, M. Kim, M. Lee, B. Lee, S. Kwon, M. Lee, M. Jo, and H. Choi: *Large-Scale Assembly of Silicon Nanowire Network-Based Devices Using Conventional Microfabrication Facilities*, Nano Letters **8** (2008), 4523–4527.
- [187] S. Kinge, M. Crego-Calama, and D. N. Reinhoudt: *Self-assembling nanoparticles at surfaces and interfaces.*, Chemphyschem : a European journal of chemical physics and physical chemistry **9** (2008), 20–42.
- [188] U. Queitsch, C. Hamann, F. Schäffel, B. Rellinghaus, L. Schultz, A. Blüher, and M. Mertig: *Toward Dense Biotemplated Magnetic Nanoparticle Arrays: Probing the Particle-Template Interaction*, Journal of Physical Chemistry C **113** (2009), 10471–10476.
- [189] M. Howland, A. Szmodis, B. Sanii, and A. Parikh: *Characterization of physical properties of supported phospholipid membranes using imaging ellipsometry at optical wavelengths*, Biophysical Journal (2007).
- [190] A. Erbe and R. Sigel: *Tilt angle of lipid acyl chains in unilamellar vesicles determined by ellipsometric light scattering.*, The European physical journal. E, Soft matter **22** (2007), 303–309.
- [191] G. Wiegand, N. Arribas-Layton, H. Hillebrandt, E. Sackmann, and P. Wagner: *Electrical properties of supported lipid bilayer membranes*, Journal Of Physical Chemistry B **106** (2002), 4245–4254.
- [192] D. M. Soumpasis: *Theoretical analysis of fluorescence photobleaching recovery experiments*, Biophysical Journal **41** (1983), 95–97.
- [193] A. Noy, A. B. Artyukhin, and N. Misra: *Bionanoelectronics with 1D materials*, Materials Today **12** (2009), 22–31.

- [194] E. Tang and S. Dong: *Preparation of styrene polymer/ZnO nanocomposite latex via miniemulsion polymerization and its antibacterial property*, Colloid & Polymer Science **287** (2009), 1025–1032.
- [195] Z. Leonenko, A. Carnini, and D. Cramb: *Supported planar bilayer formation by vesicle fusion: the interaction of phospholipid vesicles with surfaces and the effect of gramicidin on bilayer properties using atomic force microscopy*, Biochimica et Biophysica Acta **1509** (2000), 131–147.
- [196] Y. Huang, P. V. Palkar, L.-J. Li, H. Zhang, and P. Chen: *Integrating carbon nanotubes and lipid bilayer for biosensing*, Biosensors and Bioelectronics **25** (2010), 1834–1837.
- [197] C. Huang and J. Mason: *Geometric packing constraints in egg phosphatidylcholine vesicles*, Proceedings of the National Academy of Science USA **75** (1978), 308–310.
- [198] Y. Dayani and N. Malmstadt: *Lipid Bilayers Covalently Anchored to Carbon Nanotubes*, Langmuir **28** (2012), 8174–8182.
- [199] S. P. Moura and A. M. Carmona-Ribeiro: *Biomimetic particles: optimization of phospholipid bilayer coverage on silica and colloid stabilization*, Langmuir **21** (2005), 10160–10164.
- [200] M. E. Roberts, M. C. LeMieux, and Z. Bao: *Sorted and Aligned Single-Walled Carbon Nanotube Networks for Transistor-Based Aqueous Chemical Sensors*, ACS Nano **3** (2009), 3287–3293.
- [201] F. Zörgiebel, S. Pregl, L. Römhildt, J. Opitz, W. Weber, T. Mikolajick, L. Baraban, and G. Cuniberti: *Schottky barrier based silicon nanowire pH sensor with live sensitivity control*, Nano Research **7** (2014), 263–271.
- [202] O. Knopfmacher: *Sensing with Silicon Nanowire Field-Effect Transistors*, Ph.D. thesis, Uni Basel, (2011).
- [203] G. Li, R. Stewart, B. Conlan, A. Gilbert, P. Roeth, and H. Nair: *Purification of human immunoglobulin G: a new approach to plasma fractionation.*, Vox sanguinis **83** (2002), 332–338.
- [204] O. H. Lin, H. Md Akil, and Z. A. M. Ishak: *Characterization and properties of activated nanosilica/polypropylene composites with coupling agents*, Polymer Composites **30** (2009), 1693–1700.
- [205] N. R. Glass, R. Tjeung, P. Chan, L. Y. Yeo, and J. R. Friend: *Organosilane deposition for microfluidic applications*, Biomicrofluidics **5** (2011), 036501.

# Appendix

## A. Protocols

### A.1. Functionalization

- cleaning of wafers
  1. wafer pieces in holder
  2. boiling in acetone and absolute ethanol for each 5-8 min
  3. absolute ethanol rinse
  4. N<sub>2</sub> dry
- cleaning of glass slides
  1. glass slides in holder for vertical position
  2. ultrasonic treatment in acetone and H<sub>2</sub>O for each 5-8 min
  3. H<sub>2</sub>O rinse
  4. incubation at 80°C for 15 min in acid (H<sub>2</sub>O:H<sub>2</sub>O<sub>2</sub>:HCl = 5:1:1)
  5. water rinse
  6. incubation at 80°C for 15 min in base (H<sub>2</sub>O:H<sub>2</sub>O<sub>2</sub>:NH<sub>4</sub>OH = 5:1:1)
  7. water rinse
  8. N<sub>2</sub> dry
- cleaning of FET chips
  1. immersion in absolute ethanol for 3 min and rinse (FET chips come from the clean room)
  2. N<sub>2</sub> dry
- two options for hydroxylation
  1. surface activation with oxygen from air in the plasma cleaner Plasma Prep II from SPI Supplies, Structure Probe Inc. ntensity was set to highest level and left for 0.25-2 min depending on the type of substrate (chips shorter than glass or wafer substrates). This method was mostly used.
  2. surface activation in 1M NaOH [103, 204, 205]

- APTES (l)
  1. 2 % silane solution in 95:5 (vol/vol) absolute ethanol/water mixture
  2. hydrolysis for 10 min
  3. sample immersion for 0.5-2 h
  4. rinse in absolute ethanol (3 x)
  5. N<sub>2</sub> dry
  6. incubation in oven at 120°C for 20 min
- APTES (g) – see section 2.1.2
- GOPMS (g)
  1. 200-300  $\mu$ l silane in small open beaker, upright position
  2. sample positioned next to it, but shielded to avoid droplet contamination
  3. both placed in bigger glass beaker with aluminium foil cover
  4. over night incubation in oven for around 16 h at 80°C, 2 h at 120°C
  5. rinse in absolute ethanol
  6. N<sub>2</sub> dry
  7. incubation in oven at 80°C for 2 h
- Succinic anhydride (SA)
  1. weigh 140 mg SA
  2. dissolve in 2 ml DMSO and mix
  3. place samples in petri dish
  4. add 9 ml of borate buffer
  5. inject 1.5 ml of SA-DMSO solution (quick mixing)
  6. incubation for 30 min
  7. rinse in dI water for 3 min (wafers, glass slides: with ultrasound, chips: w/o ultrasound)
  8. N<sub>2</sub> dry
- EDC/NHS for 1 ml total volume
  1. weigh powder for 100 mM EDC HCl
  2. weigh powder for 50 mM NHS
  3. dissolve each in 1ml dI water
  4. place samples in petri dish



5. fill with 7 ml dI water, 1ml 10x PBS buffer (final ionic concentration: 10 mM)
  6. inject EDC, then NHS with quick mixing
  7. incubation for 10 min
  8. rinse in dI water (incubation and squeeze bottle)
  9. N<sub>2</sub> dry
- Aptamer attachment
    1. dilute from stock (100  $\mu$ M in dI water)
    2. 2-20  $\mu$ M for microarray in PBS pH 7.4 at 10 mM final concentration
    3. 10  $\mu$ M for FET in PBS pH 8.5-8.9 at 10 mM final concentration

## A.2. Buffers

- All buffers were filtered with 0.2  $\mu$ m syringe filter and stored in the fridge.
- Buffer for succinic anhydride attachment
  1. 200 mM boric acid
  2. calibrated to pH 8.0 with 1 M NaOH
- **Binding buffer** for biorecognition and aptamer folding
  1. 10 mM Tris HCl
  2. 20 mM MgCl<sub>2</sub>
  3. calibrated to pH 7.4 with 1 M NaOH
- **Blocking buffer**
  1. 1 M Trizma<sup>®</sup> Base
  2. calibrated to pH 7.4 with 1 M HCl
- Sodium phosphate buffer (**SPB**) for thrombin detection with FET
  1. 100 mM stock solutions of Na<sub>2</sub>HPO<sub>4</sub> (solution A) and NaH<sub>2</sub>PO<sub>4</sub> (solution B)
  2. mix A and B for desired pH according to buffer table (see Merck Lab Tools - Tabellen für das Labor, [www.versuchschemie.de/upload/files3/74751201\\_2244.pdf](http://www.versuchschemie.de/upload/files3/74751201_2244.pdf)) – here: pH 5.7
  3. dilute to 1 mM for FET sensing (attention: change of pH value due to dilution)
- 10x Tris glycine buffer with pH 8.5
  1. 250 mM Trizma<sup>®</sup> Base
  2. 1.92 M glycine
  3. 20 mM KCl

### A.3. PDMS

- PDMS mold
  1. mix A and B in a ratio of 10:1
  2. degassing in vacuum chamber
  3. vapour deposition of octadecyltrifluorosilane onto master in desiccator for 2h to make later PDMS mold release easier
  4. pour liquid into aluminium bowl until the height is 2 mm
  5. immerse master structure and press it to bottom
  6. short degassing to remove bubbles under master
  7. crosslinking at 100°C on a hot plate (5 min) or in an oven (at least 2 h)
- stamp fabrication
  1. cut appropriate piece with scalpel
  2. glue on SEM holder (Plano GmbH) using conductive sticky pads  $\Rightarrow$  acts a manual stamp
- printing of silane solution
  1. 1 % silane in absolute ethanol
  2. apply 25-50  $\mu$ l droplets to fully cover the stamp for 5 min
  3. blow dry for 15 sec ( $N_2$ )
  4. printing for 1 min with some pressure
  5. thermal curing at 120°C for 20 min

### A.4. Steps of the sandwich assay

- capture layer  $\mu$ CP
  1. transfer of slides into sterile well-plates (6er) with wet tissue for humid chamber setup
  2. 25  $\mu$ l TBA1 in 10 mM PBS (1x) onto EDC/NHS activated  $\mu$ CP glass slide for 1h
- capture layer nanoplotting
  1. nanoplotting of TBA1 in 10 mM PBS onto EDC/NHS activated glass slide
  2. transfer into sterile well-plates (6er)
- preparation steps
  1. 10 min blocking with blocking buffer
  2. 20 min blocking with 0.5 mg/ml BSA in 10 mM binding buffer
  3.  $MgCl_2$  in binding buffer allows aptamer to fold prior to detection

4. repeated rinsing with 10 mM Tris buffer in between steps
- biorecognition
    1. incubate slide with thrombin solution in binding buffer for 30 min
    2. allow 200 nM TBA2-red to incubate in binding buffer for at least 10 min
    3. incubate slide with the TBA2-red solution for 30 min
    4. repeated rinsing with 10 mM Tris buffer in between steps
    5. final rinsing with dI water
    6. N<sub>2</sub>
  - direct imaging

### A.5. Gelelectrophoresis

- mix 2 ml of 40 % acrylamide-bis solution with 1ml of 10x Tris glycine buffer and 6.9 ml dI water
- add 10  $\mu$ l TEMED and 100  $\mu$ l 10 % APS (v/v in dI water) and stirr quickly
- quick gel casting before it solidifies and addition of plastic comb (gel solidification for 30 min)
- sample preparation as desired and addition of loading dye
- short centrifuging (table centrifuge)
- parameters: 50 V, 100 W, 80 mA, 1.5 h
- careful release from glass frames into staining chamber
- staining in coomassie solution
- destaining
- optional drying
- imaging
- data evaluation

### A.6. Lipids

In order to form vesicles, DOPC lipids (glycophospholipid 1,2-dioleoyl-sn-glycero-3-phosphocholine) were employed. 2 mol-% of headgroup-labelled NBD-PE lipids (1,2-dioleoyl-sn-glycero-3-phosphoethanolamine-N-7-nitro-2-1,3-benzo-xadiazol-4-yl, both lipids from Avanti Polar Lipids, Inc.) were added to stain vesicles with fluorophores for optical detection. Unilamellar vesicle (ULV) solutions were prepared from stock solutions of 1 mg/ml (DOPC) and 0.1 mg/ml (NBD-PE) lipids in chloroform.

Required amounts were transferred into a flask and dried via nitrogen flow and subsequent vacuum pumping. The resulting thin film of dried lipids was dispersed in the chosen buffer. The blurry solution was left for strong sonication until the solution clarified, indicating the formation of unilamellar vesicles. ULVs can be further used to create lipid bilayers on a solid support. Different buffers (sodium acetate, MES and TRIS) with pH values ranging from 5.0 to 8.1 were tested for the bilayer formation and 12 mM sodium acetate buffer at pH 5.0 led to the desired functional lipid bilayers on APTES-functionalized surfaces. Other systems resulted in bilayer formation as well, but they were less homogeneous, with patches and a slower recovery in FRAP (data not shown here).

## B. Additional results

### B.1. FET sensing

- Thrombin detection with BU SB SiNW FET device: voltage versus running time of the experiment.

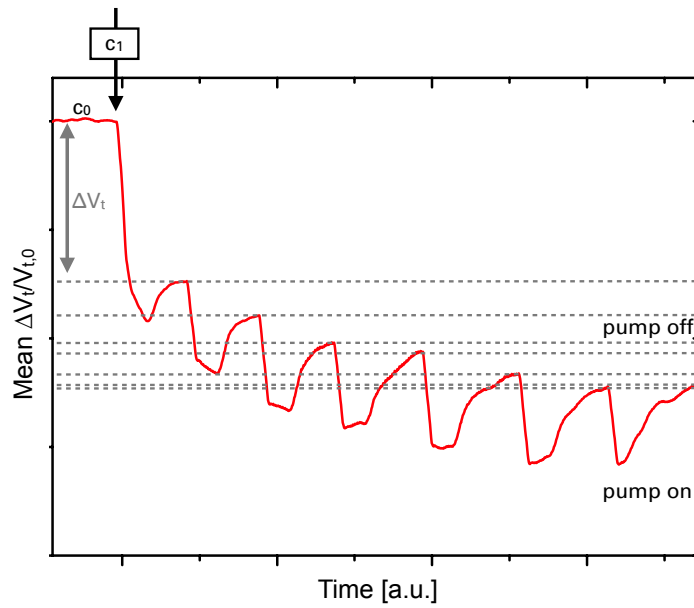


**Figure B.1.:** Mean normalized threshold voltage ( $\Delta V_t/V_{t,0}$ ) versus running time of the experiment of the sample TBA1\_B at  $I_{sd} = 2 \cdot 10^{-8}$  for the time range of thrombin injection from 200 pM to 200 nM.  $C_0$  labels the region where  $V_{t,0}$  is extracted. The first thrombin injection with the lowest concentration  $c_1$  is indicated with a black arrow. The grey dashed lines are there to illustrate where the values for the concentration curve are extracted from. Here, the pump is turned off, see label in graph.

- I-V curves and magnified detail vor increasing thrombin concentrations.

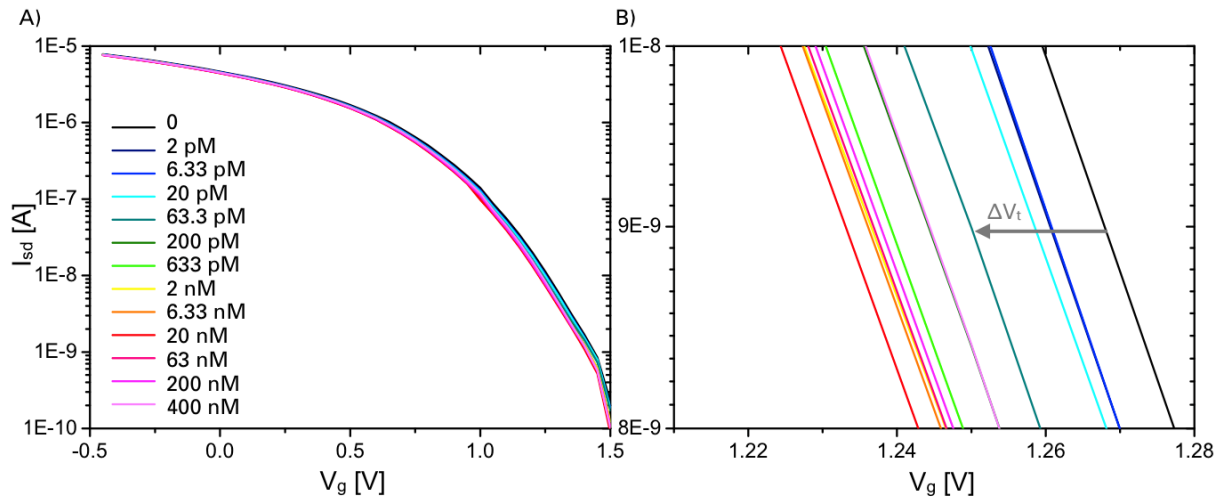


**Figure B.2.:** Transfer curves of thrombin detection with TBA1 as a capture layer from 2 pM up to 400 nM thrombin concentrations. A) Complete measurement range. B) Magnified detail at steepest slope.

- Comparison of concentration curves for individual measurements.

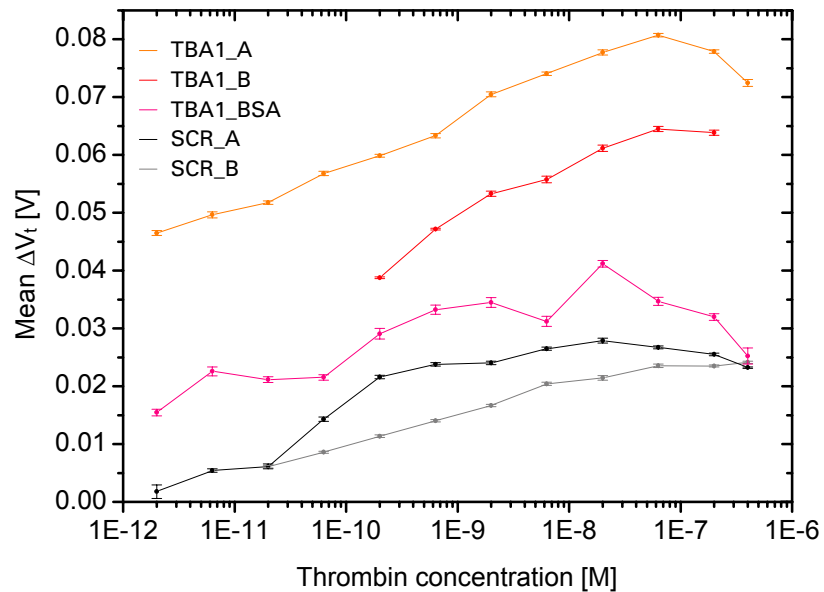


**Figure B.3.:** FET concentration curves of the mean  $\Delta V_t$  taken in steady state of five thrombin detection experiments with TBA1 as a capture layer (orange and red) and SCR as a control aptamer (black and grey). The pink curve represents a device with a TBA1 coating and BSA blocking before biorecognition was allowed. The lines serve as guides to the eye. The error bars originate from the running mean of  $V_t$  averaging over 15 neighboring data points.



# List of publications

## Peer-reviewed publications

- Zörgiebel, F., Pregl, S., **Römhildt, L.**, Opitz, J., Weber, W. M., Mikolajick, T., Baraban, L., and Cuniberti, G., Schottky Barrier based Silicon Nanowire pH Sensor with Live Sensitivity Control, *Nano Research* 7, 2014, 263-271
- **Römhildt, L.**, Pahlke, C., Zörgiebel, F., Braun, H.-G., Opitz, J., Baraban, L., and Cuniberti, G., Patterned biochemical functionalization improves aptamer based detection of unlabeled thrombin in a sandwich assay, *ACS Applied Materials and Interfaces* 5, 2013, 12029-12035
- Baraban, L., Zörgiebel, F., Pahlke, C., Baek, E., **Römhildt, L.**, and Cuniberti, G., Lab on a Wire: Application of Silicon Nanowires for Nanoscience and Biotechnology, Chapter in: *Nanowire Field Effect Transistors: Principles and Applications*, Springer Science+Business Media New York, 2014, DOI: 10.1007/978-1-4614-8124-9\_10
- **Römhildt, L.**, Gang, A., Baraban, L., Opitz, J., and Cuniberti, C., High yield formation of lipid bilayer shells around silicon nanowires in aqueous solution, *Nanotechnology* 24, 2013, 355601
- Pregl, S., **Römhildt, L.**, Weber, W. M., Baraban, L., Opitz, J., Mikolajick, T., and Cuniberti, G., Investigations on the sensing mechanisms in silicon nanowire Schottky-barrier field effect sensors, *Proceedings of IMCS 2012 - The 14th International Meeting on Chemical Sensors*, 2012, 994-996

## Publications in preparation

- **Co-author** in Baek, E. et al., Optoelectronic switching of nanowire-based hybrid organic/oxide/semiconductor field-effect transistors, *submitted to Advanced Functional Materials*
- **Co-author** in Baraban, L. et al., Nanotechnology review article: Silicon nanowire based sensors

**Selected international conferences**

- Römhildt, L. et al., Strukturierte biochemische Funktionalisierung von SiO<sub>2</sub> Sensoroberflächen zur optischen Detektion verschiedener Analytkonzentrationen, Talk at the Deutsches Biosensor Symposium DBS 2013, Wildau, Germany, 12.03.2013
- Römhildt, L. et al., Biochemical surface modification of SiO<sub>2</sub> for aptasensors, Talk at Heraeus Seminar on Functional Magnetic Nanomembranes, Bad Honnef, Germany, 06.03.2013
- Römhildt, L. et al., Silicon Nanowire Based Aptasensor, Poster at 2nd NanoSensEU Symposium on Biosensors Development “Trends and Technology“, Hasselt, Belgium, 25.04.2012
- Römhildt, L. et al., Functionalisation of Silicon Surfaces for Electrochemical Biosensing - a Nanowire Based Aptasensor, Talk at Smart Surfaces Conference, Dublin, Ireland, 08.03.2012
- Römhildt, L. et al., Surface Functionalization and Receptor Development for Biosensors, Poster at Biosensing Technology 2 Conference, Amsterdam, Netherlands, 10.-12.10.2011



## Versicherung

Diese Arbeit wurde am Institut für Werkstoffwissenschaft der Technischen Universität Dresden unter der wissenschaftlichen Betreuung Prof. Dr. Gianaurelio Cunibertis durchgeführt.

Hiermit versichere ich, dass ich die vorliegende Arbeit ohne unzulässige Hilfe Dritter und ohne Benutzung anderer als der angegebenen Hilfsmittel angefertigt habe; die aus fremden Quellen direkt oder indirekt übernommenen Gedanken sind als solche kenntlich gemacht. Bei der Auswahl und Auswertung des Materials sowie bei der Herstellung des Manuskripts habe ich Unterstützung von folgenden Personen erhalten:

- Larysa Baraban (Korrekturlesen der gesamten Arbeit)
- Jörg Opitz (Korrekturlesen der gesamten Arbeit)
- Claudia Pahlke (Korrekturlesen Kapitel 4)
- Sebastian Pregl (Matlabprogrammierung)
- Felix Zörgiebel (Matlabprogrammierung)
- Andreas Gang (Unterkapitel 4.3.2).

Weitere Personen waren an der geistigen Herstellung der vorliegenden Arbeit nicht beteiligt. Insbesondere habe ich nicht die Hilfe eines kommerziellen Promotionsberaters in Anspruch genommen. Dritte haben von mir keine geldwerten Leistungen für Arbeiten erhalten, die in Zusammenhang mit dem Inhalt der vorgelegten Dissertation stehen. Die Arbeit wurde bisher weder im Inland noch im Ausland in gleicher oder ähnlicher Form einer anderen Prüfungsbehörde vorgelegt.

Darüber hinaus erkenne ich die Promotionsordnung der Fakultät Maschinenwesen der Technischen Universität Dresden vom 01.07.2001 an.

Lotta Römhildt

Dresden, 14.02.2014